UNIVERSITÀ DEGLI STUDI DI TRIESTE

UNIVERSITÀ DEGLI STUDI DI TRIESTE

XXXV CICLO DEL DOTTORATO DI RICERCA IN

NANOTECHNOLOGIE

Development of semiconductor-superconductor nanosystems for applications in quantum computation.

Settore scientifico-disciplinare: **FIS/03**

DOTTORANDA
MAGDHI KIRTI

COORDINATORE
PROF. ALBERTO MORGANTE

SUPERVISORE DI TESI
Dr. GIORGIO BIASIOL

ANNO ACCADEMICO 2020/2021

‘‘When you change the way you loook at things,
the things you look at change.’’

- Max Plank

Acknowledgements

I would like to express my deepest gratitude to every exceptional individual who supported and guided me throughout this PhD journey, enabling me to successfully complete the PhD despite many unforeseen obstacles that arose. First and foremost, I would like to express that I owe an immense debt of gratitude to my PhD supervisor Dr. Giorgio Biasiol, Technology Director, CNR IOM whose guidance played a pivotal role in refining my academic understanding and scientific wisdom. His constant support, never ending guidance, and encouragement have been invaluable throughout the entire process. His remarkable academic competence, along with his unwavering commitment for helping early career researchers, makes him a true role model in the this competitive world of academia.

Furthermore, the endeavor to achieve this PhD degree would not have been possible without the prodigious help of the Post docs in our group. I would like to thank Dr. Abdennacer Benali for the help in the the initial stage of PhD. He was the one who followed my first steps in the laboratory and trained me on the functioning showing unlimited patience and efforts. Also, I would like to thank Dr. Tereza Steinhartovà for teaching me different equipment's in the clean room. She was a strong mentor, always persuading me to work hard with utmost diligence. Finally, I would like to thank Dr. Shravan Appani who helped me in the last year of my PhD work by teaching me different simulation software's and also, helped me in gaining insight in XRD measurements. He generously contributed his time and insights to my research.

I would be remiss in not mentioning Dr. Simone Dal Zilio who gave me training on various equipment's in the clean room and later made me autonomous in using those machines. I am also thankful to the Microscopy group headed by Dr. Regina Ciancio for the TEM measurements especially, Dr. Piu Rajak for helping me whenever needed and teaching me a bit of in-operando measurements. I am immensely thankful to Dr. Jasper Plaisier, head of MCX beamline, Elettra for the XRD measurements and sharing his expertise in this field. Finally, Dr. Pietro Parisse working in the Microfabrication, Micro-sensing and Mechanobiology (3M) laboratory for the AFM training and measurements.

Among the most memorable highlights of my PhD journey was the opportunity to work with our collaborators Mate Suto, Dr. Tovari Endre, Dr. Makk Peter and Dr. Szabolcs Csonka from Quantum Electronics group at BME, Budapest. I extend my heartfelt thanks to them for welcoming me in their group twice and helping me in device fabrication and measurements. This collaboration not only gave us fruitful results but also taught me different skills.

I have received tremendous help and support from the administrative staffs from the University of Trieste and CNR-IOM throughout my Ph.D. I would like to thank them a lot. It would have been impossible to manage my way through the subtleties of the Italian bureaucracy and tedious administrative issues without their help.

My deepest gratitude goes to my family for their constant inspiration, support, encouragements and for being a constant source of motivation. I am blessed to have parents, who despite coming from a small town always ranked education in their highest priority and had immense faith in me, and a brother who always stood by my side. Your love and support provided the emotional strength needed to navigate the challenges of doctoral research. Also, my husband Ashish Ranjan deserves a very special acknowledgement. I would not even have started my PhD without his support. Thank you being kind and patient with me.

I would also like to acknowledge and dedicate a big thanks to all my friends in Trieste, their encouragements played an integral role in my accomplishments, especially Dr. Chandradoy Chatterjee who provided me a lifeline during the most challenging times. Also, I would also like to thank my best friend Dr. Daya Sagar Dhungana and his family for encouraging me to do this PhD and helping me throughout my journey.

Henceforth, I would like to express again my deepest appreciation to everyone who played momentous roles in this journey, this thesis would not have been possible without the collective support and encouragement of these individuals and institutions. Thank you for being an integral part of this significant chapter in my academic life.

Contents

Abstract

Two-dimensional electron systems confined near the surface of narrowband semiconductors have piqued interest due to their ease of integration with superconductors, allowing for new hybrid device systems. Such hybrid systems lay the foundations of a radically new solid-state platform for scalable quantum computing based on Andreev quantum bits (qubits). These Semiconductor-superconductor hybrid systems resulting in Andreev qubits are among the most promising candidates, as high-quality superconducting thin films with transparent interfaces to a low-D semiconductor will improve coherence time as well as offer strong qubit-qubit coupling. InAs 2D electron gases (2DEGs) are the ideal semiconductor systems due to their vanishing Schottky barrier; however, their exploitation is limited by the non-availability of commercial lattice-matched substrates. For this work, a great effort has been made in the investigation of the structural and transport properties of InAs quantum wells grown by molecular beam epitaxy on GaAs (001) substrates over the years, to realize 2D electron gases with high electron mobility at low temperature. Due to the large lattice mismatch (7%) between the active InAs layer and the GaAs substrate, a step-graded buffer layer structure was employed to adapt the two different lattice parameters. We have optimized the buffer layer to reduce the residual strain in the quantum well region. Corresponding to this strain reduction, we see an increase of the electron mobility up to almost $10^6 cm^2/Vs$, in line with state of art samples on InP substrates. To understand the limiting factors of mobility in detail, we studied low temperature scattering mechanisms on these 2DEGs. The insights gained from this research enabled us to enhance the buffer layer to achieve higher electron mobilities.

These high mobility semiconductor heterostructures, were then used for integration into hybrid platforms. Topological superconducting regime was achieved with the optimization of mobility and distance of the QW from the surface to have proximity effect. This recipe allowed to reach a hybrid system with mobility around 8.6×10^4 cm^2/Vs for 2DEGs at 10 nm from the surface, with a charge around $4.95 \times 10^{11}/cm^2$ with silicon δ doping. On these shallow 2DEGs in-situ growth of aluminum films on near-surface InAs 2DEGs by Molecular Beam Epitaxy is demonstrated. Despite of the observed multidomain structure we obtained state of art electrical properties and superconducting proximity effect was observed in a Josephson junction. The growth protocol developed could thus set a new standard for the fabrication of Andreev qubits on GaAs technology.

Background

Quantum computers take advantage of quantum physics' inherent features, which hold the potential of effectively addressing problems that are intractable for classical computers [1]. Past few years have witnessed the proposition of several practical quantum computing technologies and which would represent a revolutionary achievement. Due to the rapid development of qubits, the global race to the quantum computer is in full swing. Numerous technology firms, including Google, IBM, Microsoft, and Intel ([https://quantumai.google/], [https://www.ibm.com/quantum], [https://azure.microsoft.com/en-us/solutions/quantum-computing], [https://www.intel.com/content/www/us/en/research/quantum-computing.html]) are competing for a role in quantum computing. All these advances and efforts in this field have brought a promising future for novel qubits. Quantum computers can be built using a wide range of quantum systems, including trapped ions [2,3], superconducting qubits [4,5], photons [6], and silicon [7]. The trapped ion qubits have been a promising technology, particularly in terms of the quality of the qubits. However, they are limited in scalability and by their relatively slow, μs-scale gate times. Superconducting qubits are also a good option for scalable quantum processor architecture because of their strong qubit-qubit coupling. They are currently in the forefront of industrial efforts. However, they yield shorter characteristic coherence times as collective degrees of freedom couple to the environment more effectively. Another viable platform is based on spins in semiconductor quantum dots. While this platform typically enables qubits with long coherence times, this also comes at the expense of more challenging state readout, weaker qubit-qubit coupling and slow multi-qubit gates. Also, Semiconductor quantum dots in silicon demonstrate exceptionally long spin lifetimes as qubits and are therefore promising candidates for quantum information processing [8].

As opposed to pursuing small improvements on these platforms using current technologies, this thesis is aimed at combining semiconductor channels with superconducting elements, resulting in the Andreev qubit, a radically new feature in hybrid nanostructures. This qubit,

which essentially unites the best of both worlds, is based on a microscopic spinful degree of freedom and couples to the superconducting condensate that surrounds it.

This combination is expected to have:

- longer qubit lifetimes than state of the art superconducting qubits,
- strong qubit-qubit coupling, even remotely, over macroscopic distances.

For these effects to show, direct epitaxial growth of aluminum as a superconducting material on semiconductors, is considered the most desirable approach for the production and integration of devices. Manufacturing constraints generally dictate that devices fabricated from III-V semiconductors tend to still use materials such as GaAs as substrates. Nevertheless, there are still several issues associated with direct epitaxial growth of InAs quantum well on GaAs, related to the large lattice mismatch between these two materials.

In this thesis, we have developed the growth protocols of Al/InAs hybrid systems on GaAs by Molecular Beam Epitaxy and investigated their structural and transport properties. In particular,

1. We have optimized the step-graded buffer layer structure employed to accommodate the lattice mismatch between the GaAs substrate and the InGaAs layer in order to minimize the residual strain inside the conductive channel.

2. We have studied the scattering processes limiting the low temperature mobility in these systems.

3. We have achieved in-situ growth of aluminum films on near-surface InAs 2DEGs with quality comparable or superior to the state-of-the art.

The electron mobilities achieved are high enough to envisage the fabrication of mesoscopic devices on these samples, such as Josephson junctions and hall bars as well as proximity effects are demonstrated with the help of Josephson junctions. These results open the way to explore more of the Andreev physics

Chapter 1

Introduction

1.1 Quest for quantum computing

As it is well said by R.P Feynman – "Nature is quantum and if we want to simulate it, we need quantum computer." As we know, when there is no known method for solving a problem in an acceptable amount of time using a classical computer, the problem is said to be classically hard. One example is the simulation of quantum systems. Why it is so difficult to model quantum systems? The fundamental problem is that it takes vast amounts of classical memory to completely describe quantum mechanical states. Not only is it difficult for classical computers to represent quantum states, but also to manipulate such complex information. As of this writing, only non-classical phenomena - quantum superposition and entanglement allow us to efficiently explore the high-dimensional complex Hilbert space where quantum states and quantum dynamics are defined. This was the inspiration for the effort to construct a quantum computer, in which quantum information is stored in quantum memory (qubits) and manipulated via quantum operations [9]. Then it took nearly three-fourth of a century after the discovery of quantum mechanics, and half a century after the birth of information theory and the arrival of large-scale digital computation, for people to realize that quantum physics fundamentally changes the nature of information processing and digital computation. This advancement provides physicists with an exquisitely distinct method of using and thinking about quantum theory. It is a surprising demonstration for computer scientists that the abstract structure of computation cannot be separated from the physics governing the instrument that executes the computation. Quantum mechanics introduces novel computational paradigms that were not conceived before and whose strength was not completely realized until the mid-1990s. Quantum computers would crack problems inaccessible to even the largest classical supercomputer today, which is called 'quantum supremacy'. Therefore, to master the new

technology in the foreseeable future, building a quantum computer becomes one core issue in today's research.

It is appealing to define a quantum computer as one whose operation is guided by quantum mechanical laws. But, considering the principles of quantum mechanics regulate the behavior of all physical occurrences, we must resist this temptation. Our laptop obeys quantum physics laws, but it is not a quantum computer. Quantum computers are different from classical computers as classical computers employ bits as their basic unit of data, with eight bits corresponding to one byte. Conventional computers write code in binary, as a 1 or a 0. Simply expressed, these 1s and 0s indicate whether the state is on or off. This is also known as serial processing, which is sequential in nature, which means that one operation must complete before the next one can begin. This means many computer systems use parallel processing, which is an extension of classical processing that can accomplish several computing tasks at the same time. Because bits of 1s and 0s are repetitive due to their binary structure, traditional computers also return a single result.

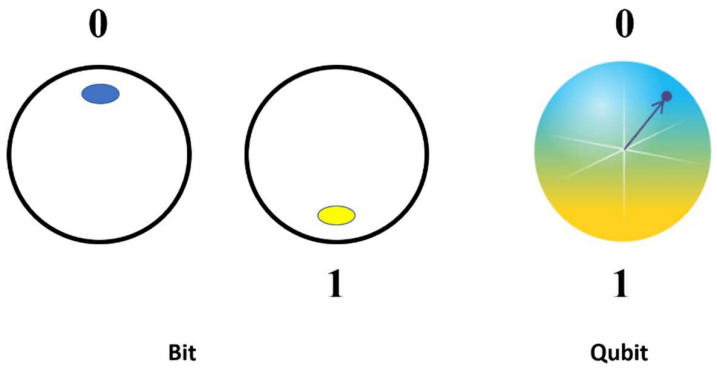

Figure 1.1*: V*isualization of a bit and a qubit. [https://1qbit.com/blog/quantum-computing/a-bit-or-two-about-qubits/]

Quantum computing, on the other hand, adheres to a separate set of principles. Qubits are the data units used by quantum computers. Qubits, unlike bits, can have a value of 1 or 0, but they can also be both 1 and 0, existing in several states at the same time as shown in figure 1.1. This is referred to as superposition, and it occurs when qualities are not specified until they are measured. This is why quantum information processors may be able to tackle some issues more effectively than classical processors. With the use of quantum computers, we can perform operations on data which has great importance in Machine learning, Cryptography, cyber

security, financial modelling, and other quantum algorithms. In these domains, quantum computers would solve problems that are currently unavailable to even the most powerful classical supercomputers, which is referred to as "quantum supremacy." As a result, creating a quantum computer has emerged as a critical topic in today's study to grasp the new technology soon. The former shows a considerable speedup over known classical algorithms and appears to strongly suggest that quantum processors are far more powerful than conventional ones. The latter proves that, in at least one scenario, quantum processors can solve problems quicker than a classical processor, albeit with a minor speed-up. Quantum processors appear to be obviously superior to classical processors for quantum physics problems because they can store the information required to represent the state of the system being simulated more efficiently. There are two types of quantum information processors reported. The processor in the first type is essentially a physics issue model that is used to directly measure properties of the corresponding system. In the second type, an array of quantum elements is employed as an information storage register, and calculations are performed via physical interactions between them, just like in a conventional computer. This chapter highlights theoretical and experimental research on Qubits carried out by scientists at many institutions all over the world over the past few decades.

1.1.1 Requirements for a quantum computer

The "DiVincenzo criteria" for a set of useable qubits summarize the needs for a workable quantum computer [10]:

1. Effective preparation of qubit states
2. Lower decoherence of qubits
3. Precision quantum logic operations for single qubits and between pairs of qubits
4. Measurement of qubit states with accuracy

Points 2, 3, and 4 are interrelated, as low decoherence is not really a meaningful criterion by itself. If it were required that qubits maintain coherence for the entire duration of a quantum computation, the task would appear hopeless: to have a fixed system error rate, the coherence of each qubit would have to scale exponentially with the number of qubits. However, it is theoretically possible to use qubits in an algorithm lasting much longer than their coherence times by using error correction. With quantum error correction, the important figure of merit is

the ratio of the qubit coherence times to the time needed for an error correction. Error correction typically involves several single and two qubit logic gates followed by projective measurement of a subset of the qubits, and succeeds in preserving the logical state of the computer if those operations and measurements are done with high enough accuracy and large enough system size. Therefore, to run a quantum computer, we need to be able to do only a few logic operations with high accuracy in times, short compared to the qubit coherence times. Similarly, the projective measurement must be done in a time short compared to the qubit coherence times, and must be done with high accuracy. By construction, the hardware coupled to the qubits to control their states introduces decoherence channels. The same is true for the apparatus used to measure the qubits' states. Navigating this tension is the main challenge of experimental quantum information. Therefore, the initial phase in this case is to effectively prepare the qubits so that they could potentially be employed in quantum computers.

1.2 Quantum bits

We require controllable and quantifiable quantum mechanical logic elements to develop a quantum computer. As in the classical case, these elements can take any number of possible states, but the analysis and construction are simplest in the case of two possible states. Following the term "bit" for a controllable information storage element with two states in classical computers, we refer to the quantum analogue as a "qubit". The term qubit was invented and first used in print by Benjamin Schumacher [11]. Qubits are a perfect example that demonstrate and highlight unconventional phenomena that quantum behavior can create in innovative ways.

In a quantum computer, the phenomenon of superposition is used as the basic unit of information, as in a bit in a classical computer, a qubit stores a binary value, either a one or a zero. However, it is manifested as a two-state quantum entity such as the nuclear spin of an atom, an electron that is either spin-up or spin-down, a photon with polarization either horizontal or vertical, etc. When measured, the qubit is found in only one of the two states. In Dirac notation, qubits are represented as a ket, where the basic values of 0 and 1 are denoted as $|0\rangle$ or $|1\rangle$. However, until it is measured, the qubit is in a superposition of 1 and 0, and there is generally a probability distribution on the value. Although these probabilities cannot be measured directly, they can take part in computations. A bit more formally, a qubit is a unit state vector in a 2-D Hilbert space where $|0\rangle$ and $|1\rangle$ are orthonormal basis vectors. For each qubit $|x\rangle$, there exist two complex numbers a and b such that:

$$|x> = a|0> + b|1> \quad (1.1)$$

Where, $|a|^2 + |b|^2 = 1$, Where, a and b define the angle which the qubit makes with the vertical axis and therefore es the probability that the given bit will be measured as a 0 or as a 1. Then, there is also the phase of the qubit which represents an angle of rotation around the vertical axis as shown in figure. 1.1. While this phase does not affect the probability of measuring the bit in a certain value, it is crucial for quantum interference effects.

"Groups of qubits in superposition can create complex, multidimensional computational spaces," according to IBM, allowing for more complicated computations. When qubits become entangled, changes to one directly influence the other, resulting in substantially faster information flow between qubits. In this section, we will discuss some possible physical systems that could be used to make qubits.

1.2.1 Semiconducting qubits

Semiconductor quantum dots appear to be suitable hosts for qubits in the development of a quantum processor. Intensive research has been conducted over the last twenty years, and many types of qubits based on various types of semiconductor spin qubits in Shallow donors and gate defined quantum dots have been generated. The spin degree of freedom quite naturally defines a qubit, as spin-up or spin-down in the case of one electron (Loss and DiVincenzo, 1998) [10], or as two distinct nuclear spin states (Kane, 1998) [7]. These spin qubit devices are known for its long-lasting quantum coherence, fast control, and potential for miniaturization and scaling. Recent breakthroughs include high-fidelity single and two-qubit gates, as well as prototype quantum algorithms. These achievements inspire future study into the development of a fault-tolerant quantum computer. Two phenomena govern the electrical characteristics of quantum dots. To begin, the Coulomb repulsion between electrons on the dot results in an energy cost for adding an additional electron to the dot. Because of this charge energy, electron tunnelling to or from reservoirs can be blocked at low temperatures; this process is known as Coulomb blockade [12]. Second, confinement in all three dimensions causes quantum effects that affect electron behavior. Because of the ensuing discrete energy spectrum, quantum dots act similarly to artificial atoms in many aspects [13]. The fundamental physics underlying dots with more than two electrons has already been discussed [14]. As a result, we concentrate on single and linked quantum dots with one or two electrons. That is why semiconductor quantum dots are also called as “artificial atoms” as they can trap few or single electron These systems are

particularly significant since they serve as the foundation for the planned electron spin-based quantum information processors.

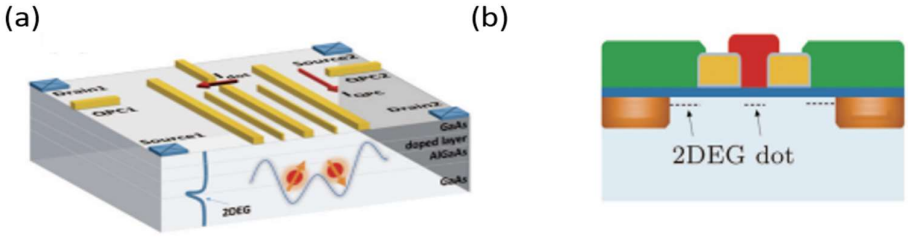

Figure 1.2: Device structure of the semiconductor quantum dot. Figure (a) is the schematics of a double quantum dot fabricated using doped AlGaAs/GaAs heterostructures. The location of 2DEG and the electrons with spin directions in the double quantum dot are also shown. (b) Cross section of a CMOS quantum dot, dotted lines denote where 2DEG and a quantum dot form. [15]

Materials mostly used for the quantum dots are GaAs and Si. Due to the high mobility of electrons in GaAs/AlGaAs heterostructure, GaAs was the first material to host qubits based on quantum dots. [16–18] As illustrated in Figure. 1.2 (a), the electrodes on the surface of GaAs offer voltage to form a potential well for trapping electrons in the two-dimensional electron gas (2DEG). Silicon is also in this case an excellent host material for spin qubits, for its weak hyperfine interaction and spin–orbit coupling [19] that reduce the magnetic noise. A silicon quantum dot can be formed either in the Si well of an Si/SiGe heterostructure or in a CMOS channel as shown in fig 1.2 (b). Also, Eriksson *et al.* demonstrated a charge qubit based on Si/SiGe quantum dots showing promising future to realize quantum computing. [20] Several different architectures of the quantum dot-based quantum computer have been promoted recently such as hybrid qubits (hybrid superconductor-semiconductor devices have been put forward, demonstrating coherent coupling between a quantum dot and a microwave field confined in a superconducting resonator) [21,22] to overcome the major issues of weaker qubit-qubit coupling and slower multi qubit gates.

1.2.2 Superconducting qubits

Superconducting qubits have emerged as one of the leading candidates for scalable quantum processor architecture since 1999 [23]. In these recent years, superconducting quantum computing has developed rapidly, in 2014 five qubits superconducting quantum system was achieved [24]. This was a major milestone achieved in the field of quantum computers.

Superconducting qubits provide the following benefits over qubits based on other quantum systems such as trapped ions, nuclear magnetic resonance, linear optical systems, spin qubits and so on:

- The designability of a superconducting qubit system is excellent. Qubits of many sorts, such as charge qubits, flux qubits, and phase qubits, can be created. Different factors, such as the qubit's energy level and coupling strength, may also be modified by varying capacitance, inductance, and Josephson energy. As a result, the Hamiltonian of superconducting qubits may be created.
- Present-day semiconductor microfabrication technology is used to create superconducting qubits. High-quality devices can be developed utilizing modern chip-making technology, which is beneficial to manufacturing and scalability. Thus, these systems are good in scalability
- The superconducting qubit system's circuit design makes it very simple to couple multiple qubits. Superconducting qubits can be easily coupled via capacitance or inductance in general.
- Superconducting qubit operation and measurement are compatible with microwave control and operability. Thus, commercial microwave devices and equipment with ease of control may be employed in superconducting quantum computing investigations.

Superconducting qubits are classified into three types based on their degrees of freedom: charge qubits, [10,23–26] flux qubits [27], and phase qubits as shown in figure 1.3 [28]. The charge qubit is composed of a Josephson junction and a capacitor, with adjusting the voltage V we can control the number of Cooper pairs. In flux qubit, L is the loop inductance and by changing the bias flux & can adjust the energy level structure of the qubit. In Phase qubit we can adjust the bias current I that can tilt the potential energy surface.

The ratio E_J /E_C distinguishes these three types of superconducting qubits, where E_J is Josephson energy and E_C is charging energy. Based on the three superconducting qubit architectures, many new types of superconducting qubits are derived, such as Transmon-type qubit, C-shunt flux qubit, Fluxonium, 0- πqubit, hybrid qubit, and so on. Transmon-type qubits, such as Transmon, Xmon, Gmon, and 3D Transmon, are now the most common superconducting qubits due to their simplicity and versatility in cQED systems.

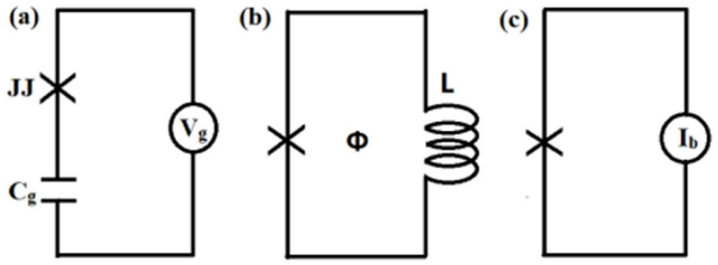

Figure 1.3: Various types of superconducting qubits a) Charge qubit composed of a Josephson junction and a capacitor b) Flux qubit c) Phase qubit [28].

Koch et al. suggested Transmon in 2007 [29]. In the charge qubit, the charge dispersion reduces exponentially in E_J/E_C, while the anharmonicity decreases algebraically with a slow power law of E_J/E_C. Xmon is a derivative of Transmon, which was proposed by Barends et al. in 2013 [30]. The Xmon qubit, unlike the original Transmon's interdigital capacitor, is produced by a cross capacitor and is connected to a shared transmission line through a resonant cavity. The Xmon qubit has quick control, extended coherence, and simple connection, making it ideal for scalable superconducting quantum computing. Gmon [31] is based on the Xmon qubit, but the qubits are associated with a junction that functions as an adjustable inductor to vary the coupling strength. The Gmon architecture avoids the problem of frequency congestion caused by fixed coupling, and it provides a versatile platform for applications ranging from quantum computing to quantum simulation. Manucharyan et al. developed fluxonium in 2009 [32] to overcome both the inductance and offset charge noise concerns. A series array of large-capacitance tunnel junctions is coupled in parallel with a tiny junction in the Fluxonium design. Next is the 0-π qubit which was first proposed by Kitaev, Brooks and Preskill [33,34] and experimentally realized by Gyenis et al. [35] in 2019. 0-π qubit is designed with a symmetrical circuit to obtain an interleaved double potential well. The two ground state wave functions of a qubit are highly localized in their respective potential wells and do not disjoint each other. The transition matrix elements between the corresponding two ground state energy levels are very small. Therefore, 0-π qubit is not sensitive to charge and magnetic flux noise. To overcome the disadvantages of different types of superconducting qubits hybrids systems [36–39] were proposed to combine the advantages of different quantum systems. In 2010, Marcos et al. proposed a novel hybrid system that coupling Nitrogen Vacancy (NV) centers in diamond to superconducting flux qubits [38]. The hybrid system takes advantage of these two systems. The flux qubits are well-controlled, but their coherence time is short, which could be used as a control element. The NV centers have long coherence times, which have the potential to be used as a long-term memory for a superconducting quantum processor.

These most recent breakthroughs in superconducting quantum computing, has gained popularity in recent years, and it is also showing great promise in the long run. Because of the benefits mentioned before, superconducting qubits have emerged as the main contender for scalable quantum computing. However, significant hurdles remain in the development of large-scale quantum computing. The fundamental drawback of superconducting qubits is their short coherence durations, which is due to their tunability and enormous size. Because superconducting qubits are not real 2-level systems, the undesirable |1> |2> transition must be avoided with care during information processing. To keep superconducting qubits, cool enough, dilution refrigerators are needed, and breakthroughs in the capacity of such cryostats should be accomplished before developing a system with millions of qubits.

1.3 The Magic of hybrid systems

Within the framework of quantum information processing superconductors and semiconductors are two of the most well-studied classes of materials. Superconductors [40] and semiconductors [17], on their own, have remarkable qualities with far-reaching applications. Even in the presence of disorder, electron pairing leads in the passage of dissipation-less current in superconductors. The defining feature of semiconductors, on the other hand, is their low charge carrier density. Thus, the chemical potential can be directly changed by applying an electric field (the field effect). Relativistic effects result in increased g-factors and significant spin-orbit coupling in some semiconductors.

What if we combined the properties of superconductors and semiconductors in a single electronic system? What kind of new physics would emerge? What further power could we obtain? These are the questions raised by superconductor-semiconductor heterostructure experiments. The essential notion behind such heterostructures is that if the contact between the two materials is good enough, electrons can travel freely over the interface (their wavefunctions are no longer localized to one material or the other). In this way, electrons might inherit qualities from both materials while also possessing all the properties outlined above. Superconducting quantum devices offer exceptional connectivity and controllability, whereas semiconductor spin qubits distinguish themselves with their extended quantum coherence, swift controllability, and potential for downsizing and expansion. Recent years have witnessed remarkable advancements in amalgamating superconducting circuits with semiconductor devices to create hybrid quantum systems that harness the advantageous properties of both components. Superconducting cavities play a pivotal role in facilitating coherent quantum

interactions across substantial distances, linking electronic attributes like the spin of individual electrons on a semiconductor chip, thus serving as a crucial connectivity element for quantum devices.

A lot of experiments are going on in this direction. With low effective mass, strong spin-orbit coupling, and high Landé g factor [41], the two-dimensional electron gas (2DEG) in InAs quantum wells is an interesting platform for mesoscopic physics experiments, but only a few realizations of mesoscopic devices [42]. More recently, lithographically defined nanowires comprised of the s-wave superconductor aluminum proximity-coupled to InAs 2DEG grown on semi-insulating InP have experimentally revealed evidence of Majorana zero modes [43]. Motivated by the possibility to explore mesoscopic phenomena and novel topological states in a lower disorder environment, significant effort is now dedicated to improvement of InAs 2DEG electronic properties. For example, the growth of composite quantum wells of InGaAs/InAs enabled improvement of the carrier mobility to $\mu = 1.0 \times 10^6$ cm^2/Vs for InAs quantum wells buried 120 nm below the top surface and grown on semi-insulating (100) InP substrates [44].

Some works were done on GaSb substrates, which has a similar lattice parameter to InAs but has some disadvantages like parasitic conduction through the substrate; due to the small band gap of GaSb, substrates are not perfectly insulating and the inability to fully deplete the 2DEG and residual sidewall conduction with surface gates [45]. Growth on GaAs would overcome these drawbacks (and take advantage of a lower cost material with a well-developed technology), but difficulties related to the large (7%) lattice mismatch to InAs must be faced [46,47]. This thesis will be dedicated to the design, fabrication, and operation of devices based on InAs 2DEGs on GaAs substrates.

These semiconductor platforms with strong spin-orbit interaction (SOI) connected to a superconductor are of particular interest to us because they have the potential to host topologically protected Majorana zero modes (MZM) suitable for Andreev qubits [48,49]. MZM signs have already been seen on binary III-V semiconductor/superconductor hybrids such as InAs/Al NWs.

Table 1.1: Typical values for the bulk Δ0 and maximum values for the proximity-induced Δ_{ind} superconducting gaps in different semiconductor-superconductor heterostructures.

Semiconductor-Superconductor heterostructure	InSb-NbTiN	InSb-Al	InAs-Al
Δ0, meV	3	0.2-0.3	0.2-0.3
max[Δ_{ind}], meV	1	0.2	0.2

Aside from induced superconductivity, achieving topological protection and MZMs necessitates the application of a magnetic field whose size is determined by the hybrid system's effective SOI and g-factor. As a result, achieving effective topological protection is dependent on the capacity to develop materials with the necessary qualities. Unexplored material platforms include ternary-based semiconductors like InGaAs, which are predicted to have much stronger spin-orbit coupling than binary compounds and could potentially provide a material with strong enough topological protection to realize topological quantum information applications [50]. These topological quantum computation holds the promise of a high degree of fault tolerance, possibly allowing a single-module quantum computing system capable of addressing crucial issues.

For the devices with superconductor-semiconductor interfaces, standard deposition of the superconductor material implies exposure to ambient air of the semiconducting materials surfaces. There has been significant progress in improving these interfaces by gently etching the oxide and optimizing the superconducting deposition [51]. Then an important step forward was taken with epitaxial growth of thin aluminum films on pristine semiconductors, without breaking vacuum [52]. High-quality epitaxial superconductor-semiconductor interfaces have been realized in different heterostructures like Al/InAs, InAsSb/Al [53,54]. Typical values of the proximity-induced superconducting gap in different semiconductor-superconductor heterostructures are listed in table 1.1. SC gap of Al depends on the film thickness. Note that Δ_{ind} in aluminum heterostructures is close to the bulk superconducting gap indicating on strong tunneling regime between semiconductor and superconductor [51,55,56]. The basic requirements for the Al film are that it should stay thin enough to withstand high parallel magnetic fields without being driven normal, and second, it should have a uniform morphology along the semiconductor interface, ensuring translational invariance in order to avoid disorder-induced sub-gap states. In-situ Al deposition using MBE should ensure both requirements,

together with the attainment of an oxide-free, highly transparent interface, and has been exploited in this thesis work.

Chapter 2

Instruments and Techniques

This chapter's objective is to provide a brief overview of the equipment and processes used in this thesis. The first section discusses the fundamentals of Molecular Beam Epitaxy (MBE) and concentrates on the MBE machine installed at CNR-IOM. This section also describes the main morphological characterization techniques: first, high resolution X-Ray Diffraction (XRD) which gives precise quantitative information on the crystal structure and is of fundamental importance for MBE growth calibration of indium alloys, and then Atomic Force Microscopy (AFM), used to probe the sample surfaces. Later in this section the growth of $In_xGa_{1-x}As/In_xAl_{1-x}As$ heterostructures containing a two-dimensional electron gas is discussed, then it is focused on the fabrication techniques that are used to pattern samples with Hall bar devices and nanometer sized top metal gates needed to perform transport measurements. Finally, last section is dedicated to the description of the experimental setup used to perform transport measurements at cryogenic temperatures.

2.1 Molecular beam epitaxy

Molecular beam epitaxy (MBE) is an Ultra-High-Vacuum (UHV) based technique for producing high quality epitaxial structures with monolayer (ML) control. MBE has evolved into one of the most widely used techniques for producing epitaxial layers of metals, insulators, semiconductors, and superconductors, both at the research and industrial production levels, since its introduction in the 1970s as a tool for growing high purity semiconductor films.

The term epitaxy is derived from the Greek root’s "epi" and "taxis," which mean "to arrange upon." In other words, epitaxy is an arrangement of one or more thermal particles atop a heated and ordered crystalline substrate to form a thin layer whose crystallinity matches that

of the substrate despite differences in material composition. Figure 2.1 shows a scheme of a typical MBE system. The apparatus consists of an ultra-vacuum chamber in which there are several material sources that provide the molecular beams that hit the sample that is kept under temperature control. When needed, the sample is maintained in rotation to improve the growth homogeneity. The mechanism that supports MBE growth is rather simple: it essentially consists in the synthesis of atoms or clusters of atoms by the heating of a solid source. They then travel in a UHV environment and collide with a heated substrate surface, where they disperse and finally become integrated into the expanding film. As the name implies, the material is supplied to the surface of wafer to deposit the material.

Earlier, MBE accomplishments include the development of GaAs / $Al_xGa_{1-x}As$ lasers [57], the production of high-quality GaAs and AlGaAs superlattices [58] and quantized electron transport [59] in these superlattice interfaces. This paved the way for nanoscale bandgap engineering and the study of quantum processes in condensed materials such as quantum cascade lasers and NWR devices. Furthermore, advanced in-situ characterization methods such as reflection high-energy electron diffraction (RHEED) or mass spectroscopy studies can be carried out in the MBE chamber. One disadvantage of MBE is that the growing procedure must take place in a very clean atmosphere. Residual gases in the growth environment cling to the substrate similarly to source materials (though less effectively), causing crystal mismatches and/or functioning as unwanted dopants. Given that even very thin structures of a few microns might take several hours to grow, it's simple to see how a poor vacuum can impair sample quality so severely that even the most perfect structure design cannot compensate.

2.1.1 Growth Apparatus:

Some basic components of the MBE system are:

- A stainless-steel UHV growth chamber is coupled to a preparation chamber, where substrates are degassed prior to growth. All components of the growth chamber must be able to withstand bake-out temperatures of up to 200 degrees Celsius for lengthy periods of time in order to limit outgassing from the internal walls.
- The pumping system must be capable of efficiently reducing residual pollutants. The pumping system is typically made up of ion pumps with supplementary Ti-sublimation and cryogenic pumps for pumping certain gas species. The base pressure of an MBE

chamber is typically between 10^{-11} and 10^{-12} mbar, resulting in an impurity concentration of less than 10^{15} cm^{-3} in developed structures.

- Liquid N_2 cryopanels surround internally both the main chamber walls and the source flanges. Cryopanels prevent re-evaporation from parts other than the hot cells and provide thermal isolation among the different cells, as well as additional pumping of the residual gas.
- Effusion cells containing the evaporation materials are critical components of an MBE system as they provide great flux stability, uniformity, and material purity. To enhance flux uniformity, the cells (typically six to ten) are arranged on a source flange and co-focused on the substrate. During a workday, the flux stability must be greater than 1%, with day-to-day changes of less than 5% [60]. This means that the temperature control must be on the order of one degree Celsius at 1000°C [61]. A mechanical or pneumatic shutter, commonly constructed of tantalum or molybdenum, is put in front of the cell to trigger the flux emanating from it.
- The substrate manipulator secures the wafer on which the growth occurs. It can perform continuous azimuthal rotations around its axis to increase wafer uniformity. The heater behind the sample is intended to maximize temperature consistency while reducing power consumption and impurity outgassing. An ionization gauge, which may be pushed into the molecular beam and utilized as a beam flux monitor (BFM), is situated opposite the substrate holder.
- The RHEED gun and detection screen are utilized to precisely calibrate the material fluxes evaporated by the effusion cells as well as used to assess the morphology and crystalline order of the surface. It also helps to monitor the epitaxial development monolayer by monolayer.
- The Reflectometer is also utilized for in-situ thickness monitoring during growth. Normal incoming light impinges on the substrate, and its reflection is recorded. A light from a white bulb with a subsequent spectrum analyzer can be employed, or, as in our system, monochromatic diode(s). We obtain a harmonic response in time by recording such reflected signal throughout growth, where the maxima-minima distances are given by

$$d = \frac{\lambda}{4n} \tag{2.1}$$

where n is the refractive index and λ is the wavelength of the probing light. The thickness, and hence the growth rates, can be monitored in-situ by carefully calibrating the refractive index for specified materials using an iterative approach utilizing X-ray diffraction data.

- The quadrupole residual gas analyzer (RGA) is a mass spectrometer that analyzes the residual gas composition in the chamber. This equipment is also used to identify helium leaks in the vacuum system through helium detection.

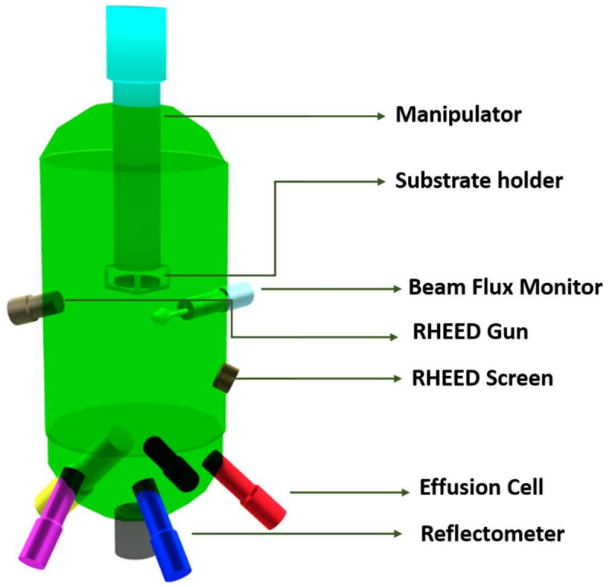

Figure 2.1: 3D schematic of the growth chamber in Molecular beam epitaxy.

2.1.2 Growth process:

Generally, three primary phases can be defined in the MBE process [62]. The first is the crystalline phase constituted by the developing substrate, which has both short- and long-range order. On the other end of the spectrum, there is the disarray of molecular beams. There is a near-surface zone between these two phases where the molecule beams hitting the heated substrate interacts with it. In this region at the phenomena most relevant to the MBE process occur. Atomic or molecular species get physiosorbed or chemisorbed on the surface, where they might go through a variety of processes (Figure 2.2).

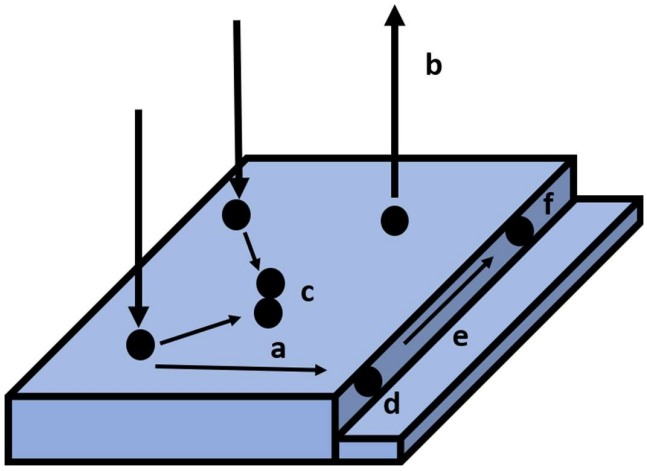

Figure 2.2: Different surface processes that takes place in the MBE. Atoms can diffuse on a flat surface (a), where they can reevaporate (b), meet other atoms to form two-dimensional clusters (c), reach a step where they can be incorporated (d), or further migrate along the step edge (e) to be incorporated at a kink (f).

Molecular beam epitaxy technique of growing a compound crystal by condensing it from base material vapors on a proper substrate has an intrinsic problem, which is the vast differences of temperatures needed for the substrate and the source materials to attain good stoichiometric growth conditions. Therefore, the partial pressures of the components must meet a certain relation and the substrate temperature must be in a range that allows for sufficient atom movement without reevaporating the crystal's components. The first promising approach was “Günther's three-temperature-method” [63]. While he succeeded to control the temperatures of the components of his setup separately, the crystal quality was not sufficient to trigger interest for the device production.

A prominent example is the MBE growth of III-V semiconductors, where the substrate is kept at an intermediate temperature between the evaporation temperature of the group III and group V source materials. Group V species have a much higher vapor pressure than group III atoms, therefore typical cell working temperatures are lower for group V evaporation (around 300 °C for As) than for group III species (around 1100 °C, 800 °C and 1000 °C, for Al, In, and Ga, respectively). At the substrate temperature, the vapor pressure of group III species is nearly zero; this means that every atom of the III species that impinges on the substrate is chemisorbed on its surface; in other words, group III atoms have a unit sticking coefficient. The high vapor pressure of the group V species favors, on the contrary, the re-evaporation of these species from the sample surface. Due to the higher group V species volatility with respect to group III, growth is usually performed with a V/III beam flux ratio much higher than one. This flux imbalance does not affect the one-to-one crystal stoichiometry between III-V species. In fact, as shown by Foxon and Joyce [64,65] in the case of homoepitaxial growth of GaAs, As atoms do not stick if Ga atoms are not available on the surface for bonding. So, in the case of GaAs, the growth rate is driven by the rate of impinging Ga atoms on the substrate.

The flux J of atoms evaporated from an effusion cell can be described as in equation 2.2 [61],

$$J = 1.1\ X\ 10^{22}\ X\ \left[\frac{aP}{d2\sqrt{MT}}\right]\ cos\theta \text{ mol cm}^{-2}s^{-1} \tag{2.2}$$

where a is the aperture area of the effusion cell, d is the distance of the aperture to the sample, θ is the angle between the beam and the normal to substrate, M is the molecular weight of the beam species, T the temperature of the source cell, and P is the vapor pressure of the beam; the vapor pressure is itself a function of the source cell temperature as in equation 2.3,

$$\log \mathrm{P} = \mathrm{A}/\mathrm{T} + \mathrm{B}\log \mathrm{T} + \mathrm{C} \tag{2.3}$$

where A, B and C are material-dependent constants. For a growth rate of about 1 μm/h the typical fluxes are ~ 10^{16} atoms cm^{-2} s^{-1} for group V elements and ~ 10^{15} atoms cm^{-2} s^{-1} for group III. In the case of alloys with mixed group III elements, such as InGaAs and InAlAs, the reactions with the group V elements are identical to those observed in the growth of binary compounds, such as GaAs [64,65]. The only difference is that the optimum growth temperature range is driven by the less stable of the two group III atoms, i.e. by indium in the case of InGaAs and InAlAs alloys. In fact, Turco et al.[66] observed that the incorporation of

In in InAlAs alloys grown on GaAs substrates decreases for samples grown at temperatures higher than 500°C, while significant Ga or Al re-evaporation takes place only at higher temperatures (about 650°C for Ga, and about 750°C for Al). For the growth of In-based alloys at substrate temperatures below 500°C, a unit sticking coefficient can be assumed; the resulting growth rate and composition are simply computed from the two binary growth rates that constitute the alloy. For example, if R_{InAs}, and R_{GaAs} are the growth rates for InAs and GaAs respectively, then the total growth rate of the alloy is $R_{InGaAs} = R_{InAs} + R_{GaAs}$ while the indium concentration x is the same as in the gas phase and is given by equation 2.4

$$x = \frac{R_{InAs}}{R_{InAs} + R_{GaAs}} \tag{2.4}$$

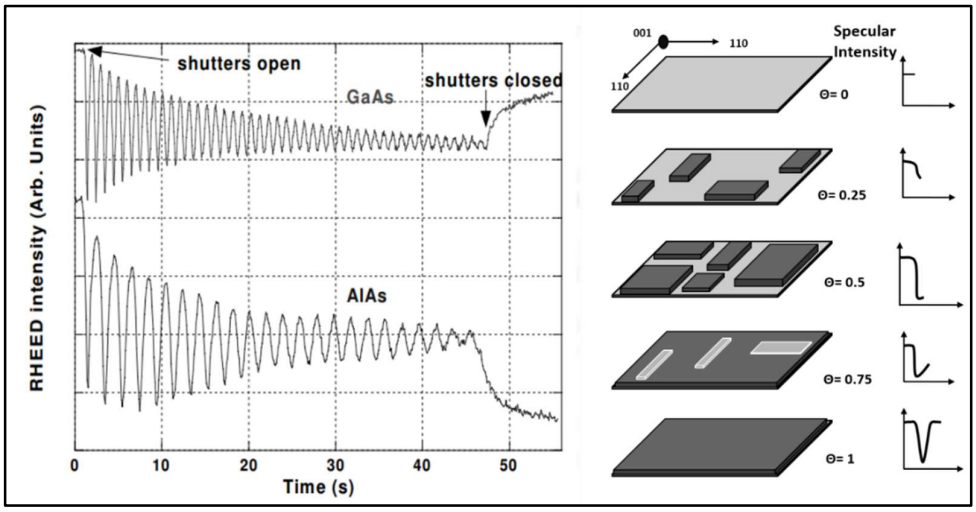

Figure 2.3: In the left panel, RHEED oscillations of an actual measurement for GaAs and AlAs grown on GaAs (001). In the right panel a schematic view of the relationship between RHEED intensity and monolayer coverage Θ.

2.1.3 Calibration of growth rate

To grow the ternary alloys such as $In_xGa_{1-x}As$ and $In_xAl_{1-x}As$ (known indium concentration x) for the semiconductor, the three growth rates R_{GaAs}, R_{AlAs}, and R_{InAs} must be precisely measured prior to growth.

- **GaAs and AlAs-** The intensity oscillations of the specular spot of the RHEED signal during the formation of a GaAs or AlAs film on a GaAs substrate define the growth rates of GaAs and AlAs [61]. A high energy (up to 20 keV) electron beam is focused on the sample surface at grazing incidence; the electron diffraction pattern is displayed

on a fluorescent screen and captured by a CCD. The electron beam is scattered solely by the first atomic layers due to grazing incidence and the short mean free path of electrons in materials, resulting in a surface sensitive diffraction pattern. Furthermore, the grazing geometry restricts RHEED electron interference with molecule beams, making the approach suited for real-time investigation during growth. The intensity of the zero-order diffraction spot or the specular spot is recorded as a function of time during the growth of crystal. An example is shown in figure 2.3, where we can notice the intensity of the spot has an oscillatory behavior. This arises because of the flat surface, present when a monolayer is complete and reflects the electrons optimally, however when a half-monolayer is done then the electron beam is partially scattered by the stepped surface. Starting with a flat surface and progressing with growth, the incident electron beam is partially scattered by the island steps of the growing monolayer, diminishing the reflected intensity, as seen schematically in the right panel of figure 2.3. Scattering becomes maximal at half monolayer coverage, whereas once the new monolayer is completed, the surface flattens again due to island coalescence, and the reflected intensity recovers its value. The increased frequency causes a progressive dumping of the oscillation intensity. As a result, a RHEED oscillation period corresponds to the formation of a single monolayer. By measuring the time required to complete a particular number of oscillations, one may compute the growth rate in monolayer/s for a constant effusion cell temperature and simply convert it to units of Å/s if the lattice parameter of GaAs or AlAs is known. Prior to sample growth, this calibration is performed virtually every day on a make do substrate. With constant cell temperatures, the day-to-day variation of R_{GaAs} and R_{AlAs} is 1%; however, the long-term behavior of these rates is predictable, and is constant (within 12%) until the cell is almost empty, unless major changes to the cell environment occur (such as refilling, etc.).

- **InAs**- RHEED oscillations cannot be used in general to assess InAs growth rates. This is because obtaining excellent quality, monolayer-flat InAs surfaces cannot be grown directly on GaAs. In fact, even after the first one or two monolayers, the substantial lattice mismatch between InAs and GaAs (~7.2%) encourages the creation of 3D islands. However, the relationship (2.4) gives an alternate technique for evaluating the InAs growth rate by measuring the GaAs growth rate in-situ using RHEED oscillations

and the In concentration in a thick InGaAs layer ex-situ using X-ray diffraction measurements (see section 2.5) In flux calibration is a time-consuming process that includes growing many samples of $In_xGa_{1-x}As$ and doing repeated X-ray diffraction observations foe each sample. Because of this, and owing to the relative stability of the fluxes until the cells are nearly empty, the Influx calibration is only conducted every few months, after substantial maintenance operations to the MBE chamber.

The MBE chamber, which was established at CNR IOM in Trieste, is primarily dedicated to the creation of GaAs-based heterostructures with extremely high purity. This type of technology demands some special changes. Two 3000 l/s cryopumps are replacing the ion pumps, resulting in a cleaner and more powerful pumping system. Mounting all-metal gate valves prevents viton seal outgassing. P-doping does not utilize any group-II elements, such as Be, because they are known to significantly impair carrier mobility. High-limit and copy cells are used to avoid cell topping off or fixing for extended periods of time. Following the installation of the MBE system, substantial degassing, and a three-month bake-out phase at 200°C were carried out to increase performance.

2.1.4 Substrate handling

As cleanliness is crucial for MBE-growth in general, substrate handling is an essential part of growth operations even more for highest quality structures. Growth substrates are commercially available with a high level of purity and crystal quality; and they are perfect as per MBE standards. A popular mounting procedure exploits the strong adhesive force that liquid gallium exerts on substrate and holder when a thin layer is deposited between the two. While this method results in an indium or gallium-contaminated back (unfavorable for further processing), gluing has several advantages over clamping the substrate to the holder:

(1) Because to its high thermal conductivity, liquid gallium provides optimal temperature distribution over the whole substrate area.
(2) The adhesive force is also dispersed evenly throughout the entire surface, whereas spring-loaded clamps exert punctual force, generating strain in the substrate.
(3) The liquid gallium approach, when completely disseminated, eliminates air pockets beneath the substrate, which could cause undesirable outgassing and possibly damage to the substrate.

(4) When it comes to substrate size and shape, the glueing approach offers a lot of leeway (for example, a square wafer can be loaded and processed just as readily as four quarter wafers on one holder to compare different manufacturer's substrates).

2.2 X-ray diffraction

X-rays are electromagnetic radiation with wavelengths ranging from 0.01 to 1 nanometer. When high-energy electrons are dialed back and lose energy, X-beams are produced. This should be accomplished by passing a high voltage (10 kV) between a cathode and an anode. Following that, high-energy electrons are extracted from the cathode and strike the anode. X-rays are released at this period. The frequency of the electrons with the maximum energy will be defined by the fundamental charge of electrons, $q_e V = h\, f_{max}$ where $q_e = 1.60218\ X\ 10^{-19} C$, and the voltage applied between the electrodes, $\lambda_{SWL} = \frac{hc}{q_e V}$.

Wave diffraction can be used to study crystalline order. When the wavelength is about equal to the lattice constant (as it is for x-rays in crystalline substances), the diffracted beams contain information about the crystal structure, as demonstrated by Bragg's equation. When constructive diffraction occurs, these beams have distinct intensity peaks, which may be utilized to calculate the periodicity of the crystal lattice using Bragg's equation. Since Max von Laue's initial observation of X-ray diffraction by a crystal in 1912 [67,68], and the Bragg's quantitative explanation of this phenomenon, this approach has proven to be a potent instrument for obtaining precise quantitative information about crystal structures.

2.2.1 Bragg's law

Figure 2.4 depicts parallel atomic planes that act as plane reflectors. d is the distance between these parallel surfaces. The angle formed by the incident beam and the plane's normal (θ) equals the angle formed by the normal and the reflected beam. The path difference between two nearby waves may be expressed as $\Delta = 2d\ sin\theta$, as illustrated in figure 2.4.

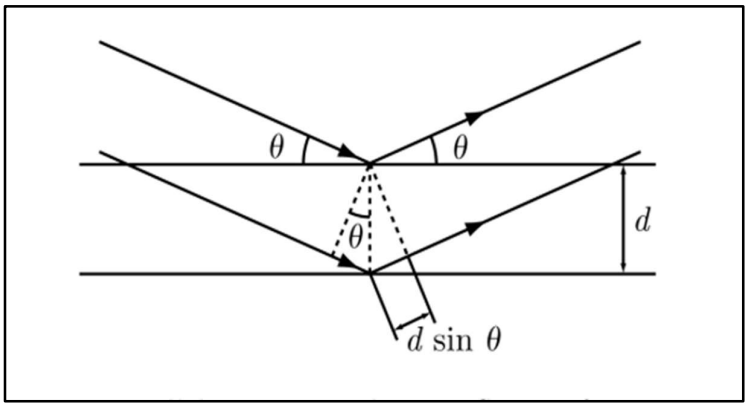

Figure 2.4: Bragg's Law. Two parallel waves reflecting from two parallel atomic planes separated by the distance d [69].

When the route difference is an integer multiple of the wave length, the waves reinforce one another. This is referred to as a Bragg reflection, and it happens at any integer multiple of λ:

$$2d\ sin\theta_B = n\lambda \tag{2.5}$$

This is known as Bragg's law. If the path difference is half the wavelength (or any integer multiple of the wavelength plus a half), the reflected waves cancel each other out:

$$2dsin\theta_{\boldsymbol{B}} = (n + \tfrac{1}{2})\,\lambda \tag{2.6}$$

The spacing of the reflection planes determines the Bragg angle θ_B. The interplanar distance for a particular crystal plane (hkl), in the unit cell of a crystal with lattice constant a is:

$$d = \frac{a}{\sqrt{h^2 + k^2 + l^2}} \tag{2.7}$$

2.2.2 Diffractometer

To measure accurately the incident and diffracted angle of the monochromatic X-ray radiation, a High-Resolution X-Ray Diffractometer (HRXRD) is needed. Such an instrument is schematically depicted in figure 2.5 and is composed of four main elements:

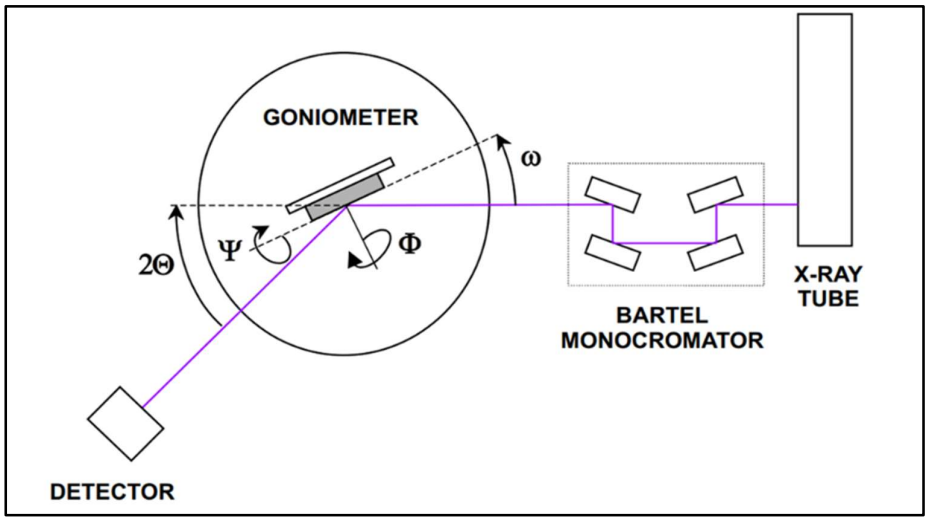

Figure 2.5: Schematic view of a four-axes diffractometer. The sample is colored in gray and all four controllable rotation angles are indicated.

- The X-ray tube: It consists in general of a metal anode that is impacted by a stream of high energy (30-40 keV) electrons released by a nearby cathode; the core level electrons of the anode's atoms are stimulated, and when they recombine, they emit X-ray photons at a specific range of wavelengths characteristic of the anode's element. A copper anode tube was employed in our configuration.
- The monochromator chooses only one of the transmitted wavelengths. The wavelength must be carefully chosen for high resolution diffraction measurements. To accomplish this, the X-rays are subjected to repeated Bragg reflections in suitably selected single crystals, which has the added benefit of considerably lowering the angular divergence of the outgoing beam. We have always utilized a so-called Bartel monochromator for our experiments, in which the beam undergoes four times the 220 reflections in germanium single-crystals. This results in a wavelength determination uncertainty of less than one part in 100,000 and an angular divergence of 12 arcsec.
- The goniometer oversees measuring the Bragg angles and properly aligning the crystal planes regarding the incident beam. The angles are to be be adjusted: 2θ is twice the diffraction angle ω, and it is the angle between the incident beam and the sample surface. Because these two angles are required to calculate the lattice plane spacing, they must be fixed and determined as precisely as feasible. The resolution in our instrument is 10^{-5} degrees.

- The detector collects and counts the X-ray photons. According to the resolution to be achieved it can be coupled to a receiving slit that simply limits the acceptance angle of the detector or to another germanium monochromator (which increases the resolution, but on the other hand reduces greatly the count rate, thus increasing the acquisition times).

2.2.3 Strain and alloy composition in epilayers

Dislocations and crystal lattice strain are essential subjects in semiconductor materials and devices. Strain is frequently employed as a design parameter in new semiconductor materials to improve electron mobility [70]. X-ray diffraction was employed in this thesis for indium flux calibration as well as indium concentration, residual strain measurements and dislocation density in $In_xGa_{1-x}As/In_xAl_{1-x}As$ quantum wells grown on GaAs substrates. High-resolution X-ray diffraction (HRXRD) is a very sensitive and non-destructive method for detecting crystal lattice strain in semiconductor materials such as gallium arsenide and all elements on the periodic table's "metalloid staircase" [71,72]. Because the existence of defects such as dislocations and point defects cause lattice deformation, the advantage of employing X-rays is that we can investigate the average effect of millions of faults influencing lattice periodicity. Rocking curves (RCs) and reciprocal space mapping (RSM) X-ray diffraction methods enable the linkage of structural parameters to epitaxial development processes, electrical/optical properties, and so on.

As we concentrate on $In_xGa_{1-x}As/In_xAl_{1-x}As$ quantum wells grown on GaAs substrates our work here is simplified on the analysis of diffraction data since all indium containing layers are grown epitaxially on GaAs <001>. They have the same crystal lattice (face-centered cubic), and have lattice constants of comparable size. This enables the overlayer crystal structure to be measured in comparison to GaAs. Typically, a rocking curve or ω-2θ scan is used to quantify the difference $\Delta\theta$ in the angle of the overlayer's diffraction peak with respect to the peak of the substrate. A rocking curve is defined as a simultaneous scan of the angles 2θ and ω so that reciprocal lattice vectors of different length but identical orientation are probed. Before measuring the rocking curve, the substrate's crystal plane must be oriented about the diffractometer setup by maximizing the peak intensity of GaAs with respect to the two angles Ψ and Φ.

As Hornstra and Bartels [73] pointed out, the measured angular difference $\Delta\theta_M$ between the epilayer and the substrate might differ from the true difference $\Delta\theta_B$ due to tilting effects between the substrate and the overlayer. This tilt effect, however, may be avoided by measuring four rocking curves following sequential 90-degree rotations of the sample around the Φ axis; the proper Bragg angle difference is then calculated in equation 2.8.

$$\Delta\theta_B = \frac{\Delta\theta_M^0 + \Delta\theta_M^{90} + \Delta\theta_M^{180} + \Delta\theta_M^{270}}{4} \tag{2.8}$$

As we know that, perfect cubic crystal shows the relation $a_\perp = a_{||} = a$. In theory, measuring merely the (004) rocking curves and deducing the crystal structure of the developed material would suffice. When an overlayer with a different lattice parameter than the substrate is epitaxially grown, the overlayer is tetragonally distorted to match the substrates in plane lattice parameter, compensating with an opposing distortion of the out of plane dimension. Even if the overlayer is grown well beyond the critical thickness, and even if care is made to relax the strain due to lattice mismatch and have a cubic lattice for the overlayer, a minor tetragonal distortion cannot be ruled out. That is why the overlayer primitive cell requires both (004) and (224) rocking curves. Because all samples were grown on (001) oriented GaAs substrates, we took the rocking curves near the symmetric (004) Bragg reflection of GaAs to measure $a_\perp$, the lattice parameter along the growth direction, and the rocking curves near the asymmetric (224) reflections of GaAs to evaluate $a_{||}$, the lattice parameter in the <110> directions. The rocking curves were recorded in the vicinity of the asymmetric (224) reflections of GaAs with both grazing incidence (224 ω +) and grazing exit (224 ω −) angles.

The [001] lattice parameter is calculated as in equation 2.9,

$$a_\perp = \frac{\lambda}{2Sin\,(\theta_B^{(004)} + \Delta\theta_B^{(004)})} \tag{2.9}$$

Then the <110> lattice parameter is

$$a_{||} = \sqrt{\frac{8}{(\frac{2\mathrm{Sin}\left(\theta_B^{(224)} + \Delta\theta_B^{(224)}\right)}{\lambda})^2 - (\frac{4}{a_\perp})^2}} \tag{2.10}$$

In the equations 2.9 and 2.10 $\theta_B^{(004)}$ and $\theta_B^{(224)}$ are the Bragg angles of GaAs for the (004) and (224) reflections, and $\Delta\theta_B^{(004)}$ and $\Delta\theta_B^{(224)}$ are the angular distances of the overlayer peak with

respect to the GaAs. A typical (004) rocking curve for our semiconductor heterostructure is plotted in figure 2.6.

To get the indium concentration x of the alloy layer knowing both the in plane and out of plane lattice parameters, one must consider the tetragonal distortion and rely on elasticity theory to derive the "unstrained" lattice parameter of the alloy [74]. Practically one must solve the following equation:

$$\varepsilon_{\perp}(x) = -2\frac{C_{12}(x)}{C_{11}(x)}\varepsilon_{||}(x) \tag{2.11}$$

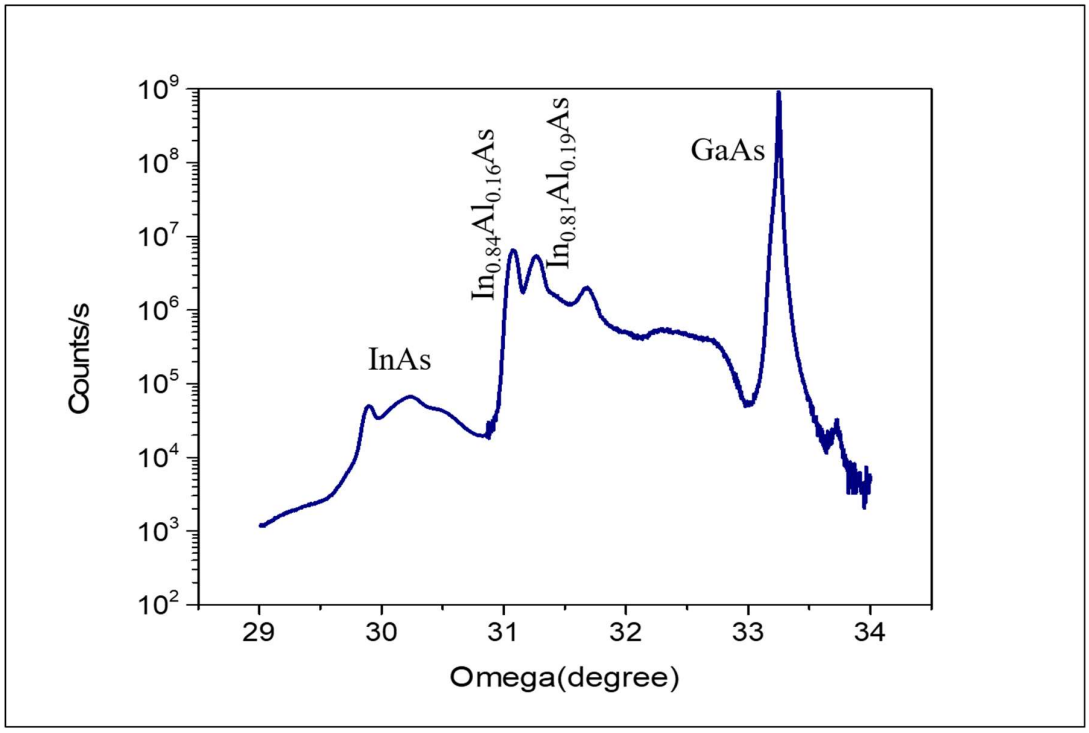

Figure 2.6: A typical (004) rocking curve from our samples for relaxed buffer layer on GaAs.

where $\varepsilon_{\perp}(x) = \frac{a_{\perp} - a_0(x)}{a_0(x)}$ and $\varepsilon_{||}(x) = \frac{a_{||} - a_0(x)}{a_0(x)}$ with $a_0(x)$, $C_{11}(x)$ and $C_{12}(x)$ are the lattice parameter of the unstrained unit cell and the stiffness constants of the layer with In concentration x respectively. These values are obtained by linear interpolation of the binary compounds values as stated by Vergard's law and confirmed by recent literature [75].

2.2.4 2-D Reciprocal Space Mapping (RSM)

The diffractometer employed to perform the RSMs measurements presented in this thesis is a Phillips X'Pert-MRD using a Cu-Kα radiation with a wavelength λ = 1.54056 Å. with Malvern Panalytical Empyrean high-resolution XRD equipped with 1.2 KW Cu anode and point detector was employed to carry out HRXRD measurements in triple axis geometry, in which the incident optics contains ½° divergence slit and 2xGe (220) asymmetric hybrid monochromator ensuring the collimation of $K_{\alpha 1}$ (λ = 1.540598 Å) in the plane of scattering, while 2xGe (220) asymmetric triple axis analyzer was placed prior to detector, in order to obtain superior angular resolution. The HRXRD measurements of asymmetric (224) reflection were carried out mainly in grazing-exit configuration due to its sensitivity in obtaining in-plane lattice parameter information [76].

2.2.5 MCX Beamline:

In this work we have also used MCX beamline at ELETTRA (the Italian national Synchrotron Radiation facility in Trieste), to carry out non-single crystal diffraction experiments using synchrotron Radiation. This beamline uses a bending magnet beamline for Material Characterization by X-rays. This beamline has been designed to work in the range 3-12 keV, exploiting the high brilliance of ELETTRA bending magnets in this spectral region. The main target of this beamline station is research and development in physics and engineering of materials surfaces, thin films, and coating technology. The intrinsic flexibility of the proposed geometry makes MCX an ideal tool for diffraction measurements from polycrystalline materials in general thin films. The experimental set-up of the MCX beamline is shown below

- **Source:** The storage ring of Elettra – Sincrotrone, Trieste operates at two different energies: 2.0 GeV with a ring current of 310 mA and 2.4 GeV with a current of 160 mA. MCX is installed on a bending magnet X-ray source. When the ring is operating at an energy of 2 GeV its critical energy is 3.2 keV, at E = 2.4 GeV the critical energy is 5.5 keV. The source provides a broad energy spectrum with usable photons of energies as high as 25 keV.
- **Optics:** The optical setup of the beamline consists of two mirrors and a monochromator. The first cylindrical mirror is Pt coated and collimates the beam on the monochromator. The second optical element is a fixed exit monochromator equipped with two Si (111) crystals. The second crystal is mounted on a bending

mechanism for focusing in the sagittal plane. The second Pt-coated mirror is placed downstream the monochromator and can be used flat or can be bent, with a radius of 6 km for focusing in the longitudinal direction. The overall optical layout works in a strictly 1:1 configuration, with the monochromator at 18 m from the source and the focus (sample position), and the mirrors are positioned symmetrically around it. The optical setup of the beamline produces an X-ray beam with energy between 6 and 21 keV corresponding to a wavelength between 2.0 and 0.6 Å. The beam spot at the experiment can be varied from point focus (0.3 × 0.3 mm^2), to line focus (5 × 1 mm^2). The flux at the sample is ~10^{11} photons per second. The effect of the optical elements on the diffraction line profile is discussed in detail in this article [77].

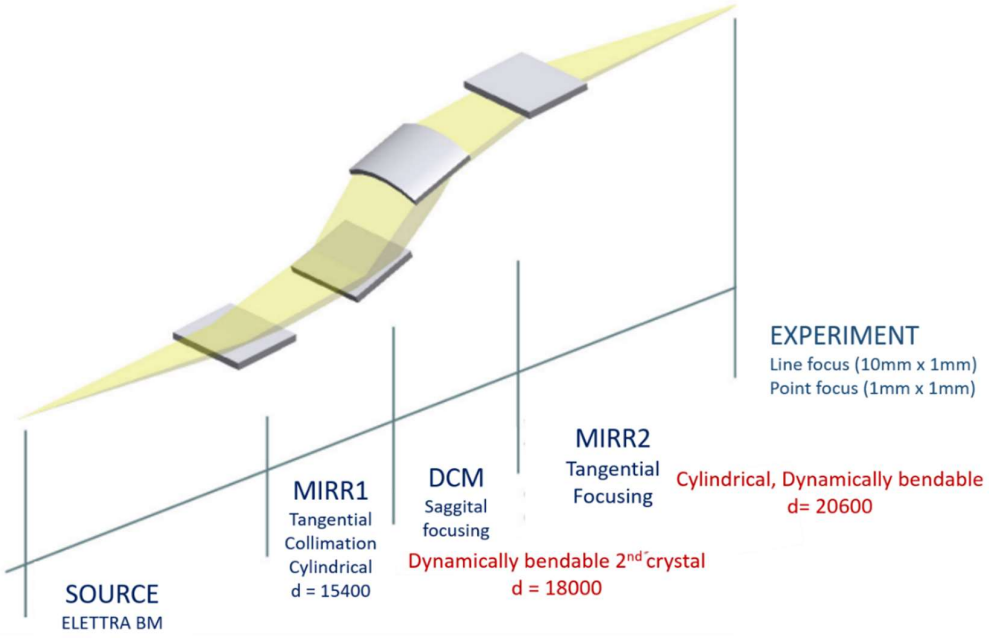

Figure 2.7: Schematic of the MCX Beamline optical system, showing, from left to right, the first is the source with Elettra bending magnet, then there is MIRROR 1 (vertical collimating) mirror, Then the dynamically bendable crystal and the second MIRROR 2 (vertical focusing) mirror to the experiment station. Distances from the source are given in millimeters [77].

The experimental station is based on a 4-circle Huber diffractometer, equipped with a high-count rate fast scintillator detector. The 2θ arm can be equipped with a pair of slits or an analyzer crystal for improved angular resolution. In a standard diffraction measurement, data is collected in flat plate (reflection mode) or capillary mode (transmission mode). For the latter mode a cryo-stream or a hot air blower may be installed so the samples may be cooled to 100

K or heated to 1273 K. Measurements of the In concentration and the residual strain in the QW were carried out using this Huber diffractometer using an X-ray energy of 8 keV. Symmetric (0 0 4) Bragg scans were used to measure lattice parameter in the growth direction. The exact composition of the 0.81 and 0.84 regions was determined by asymmetric (2 2 4) Bragg scans of thick layers with complete lattice relaxation. Also, Bragg scans on our samples were done at MCX beamline λ ~1.5498 Å to have clear Bragg peaks on our samples with Al layer.

2.3 Atomic force microscopy

Atomic Force Microscope (AFM) has been an integral part of nanotechnology since its invention in the late 1980s. Whereas before, investigating nanoscale materials was time-consuming, the AFM has made it possible to undertake these measurements in a reproducible manner. AFM's able to obtain high resolution images of both conductive and insulating samples. The AFM belongs to the family of the scanning probe microscopes (SPMs). The working concept is based on a cantilever with a sharp tip's capacity to detect minuscule interatomic distances.

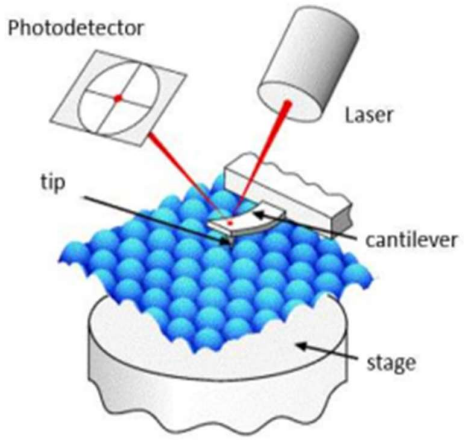

Figure 2.9: Shows the schematic of an Atomic Force Microscope. The tip here interacts physically with the sample, this interaction is measured by a photodetector which records the laser signal reflected from the top of the cantilever. The stage can be used to move the sample or the cantilever depending on the AFM [78].

The basic concept behind all SPMs is simple: the material to be examined or the microscope probe (tip) is placed onto a piezo-resistive crystal (piezo). Using voltages, the piezo is deformed with sub-nanometer precision in all three dimensions. The parameter utilized to identify the tip-sample distance varies amongst SPMs. The force between the tip and the sample is the measuring parameter for the AFM. A laser beam is reflected from its point of origin off a cantilever and towards a four-quadrant photodetector in a standard AFM setup. Interatomic forces may be detected in both the lateral and vertical directions using a four-quadrant detector. The position and intensity of the reflected beam are recorded on the detector as the AFM interacts with the sample [79] as depicted in figure 2.9. Depending on the AFM's operation mode, the information captured by this detector can be utilized in a variety of ways.

An AFM can be used in one of three modes: contact, non-contact, or intermittent contact or tapping. As illustrated in Figure. 2.10, each mode may relate to a certain section of the force-distance curve. The tip is touching the sample surface in contact mode. The tip sample interactions are repulsive, with magnitudes ranging from 10^{-6} to 10^{-9} N. Because the forces driving the feedback system are short-range repulsive, the spatial resolution can be quite high. The disadvantage is that because the tip is always in physical touch with the sample when scanning, very large (on the atomic scale!) lateral friction forces exist, which can damage the sample surface, the tip, and cause artefacts in the image.

In non-contact mode, the tip-sample distance is 10 to 100 nm. The tip-sample force is attractive owing to van der Waals interactions, with a typical value of 10^{-9} to 10^{-12} N and a positive derivative. The cantilever is vibrating at a frequency r slightly above its resonance frequency ω_0 far away from the sample. As the tip is approaching the sample, the interaction induces a decrease in the resonance frequency ω_{int} according to $\omega_{int} = \sqrt{\omega_0^2 - \frac{1}{m} * \frac{\delta F^{ts}}{\delta r}}$, where F^{ts} is the tip-sample force. This induces a decrease of the amplitude of the oscillation (see figure 2.10) which is monitored by the feedback loop to control the tip-sample distance. The intensity of the tip-sample interaction in non-contact mode is 10^3 to 10^6 times less than that of the contact mode; As a result, this operating mode is recommended for imaging extremely sensitive samples such as films made from organic materials. However, the achievable spatial resolution is lesser because non-contact AFM is based on long-range Van der Waals interactions.

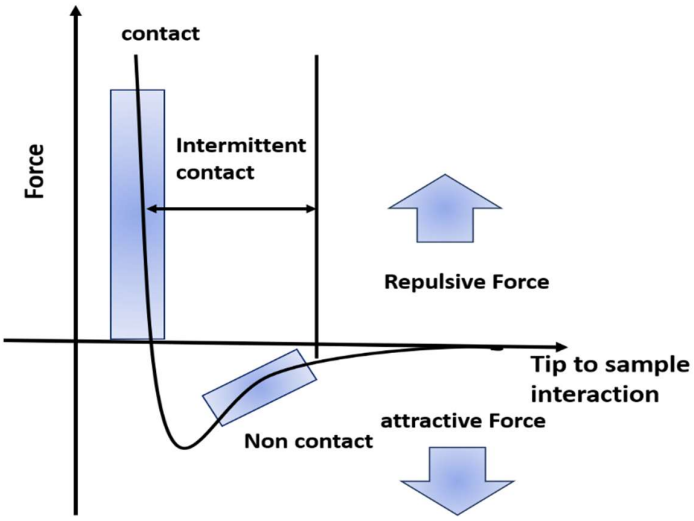

Figure 2.10: Typical force versus tip-sample distance curve. The regions Indicated are the force regimes of contact, non-contact, and intermittent-contact mode.

The intermittent contact mode is based on the same principles as non-contact mode, except the cantilever in ICM vibrates at a frequency just below its natural frequency. As a result, when the tip gets closer to the sample, the vibration amplitude rises (see Figure.2.9) until the tip reaches the sample surface at the conclusion of each oscillation. This causes the vibration amplitude to be reduced to the given value. The vibration amplitude, as in NCM, is utilized to adjust the tip-sample distance. Intermittent contact mode has spatial resolution equivalent to contact mode and interaction strength halfway between Contact and Non-contact mode; moreover, lateral friction forces are nearly nonexistent, allowing imaging of sensitive materials.

2.4 Transmission electron Microscope

Transmission electron Microscope **(**TEM) microscopes employ an electron particle beam to see specimens and provide a greatly magnified picture. TEMs can magnify things up to 2 million times. To form an image, they use a high voltage electron beam. An electron gun at the top of a TEM releases extremely powerful electron beam that go through the vacuum tube of the microscope. Rather of utilising a glass lens to concentrate the light (like in light microscopes), they utilise an electromagnetic lens to focus electrons into an extremely narrow beam. This beam then travels through the very thin material, and the electrons either scatter or strike a fluorescent screen at the bottom of the microscope (figure 2.11). On the screen, an image of the specimen with its various components colored differently depending on their

density shows. This picture can then be examined immediately in the TEM or photographed. TECNAI 20 was used to generate TEM pictures of phase pure powders at 1200 kV accelerating voltage. The powder samples were dissolved in ethanol and ultrasonicated for 1 hour before being put onto a copper grid for imaging. The sample must be exceedingly thin for a detectable number of electrons to travel through it. As a result, far more time is spent polishing and thinning the samples than is spent studying the samples under the microscope. The images, on the other hand, can be examined at exceptionally high resolution, allowing users to detect individual atoms. This high resolution enables us to see crystallization that we would not have been able to see using other approaches.

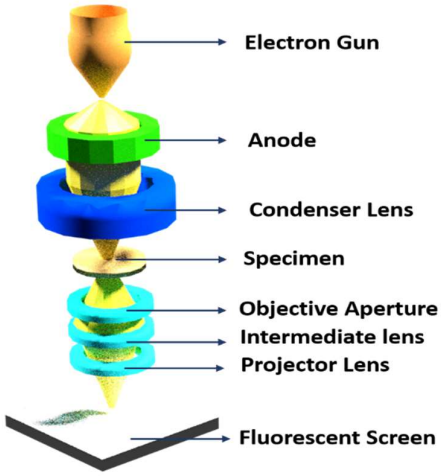

Figure 2.11: 3D schematic of transmission electron microscope.

2.4.1 Sample Preparation for TEM:

A sample must be processed in order to be thin enough to enable electron transparency in the TEM. The sample thickness should be less than 90-100 nm, however for some methods, such as phase contrast imaging, thicknesses of 50 nm or less are necessary. We are more interested in examining samples in cross-section than in plan view, therefore the talk that follows focuses on the former. However, with certain process adjustments, both conventional and FIB procedures may create plan view samples.

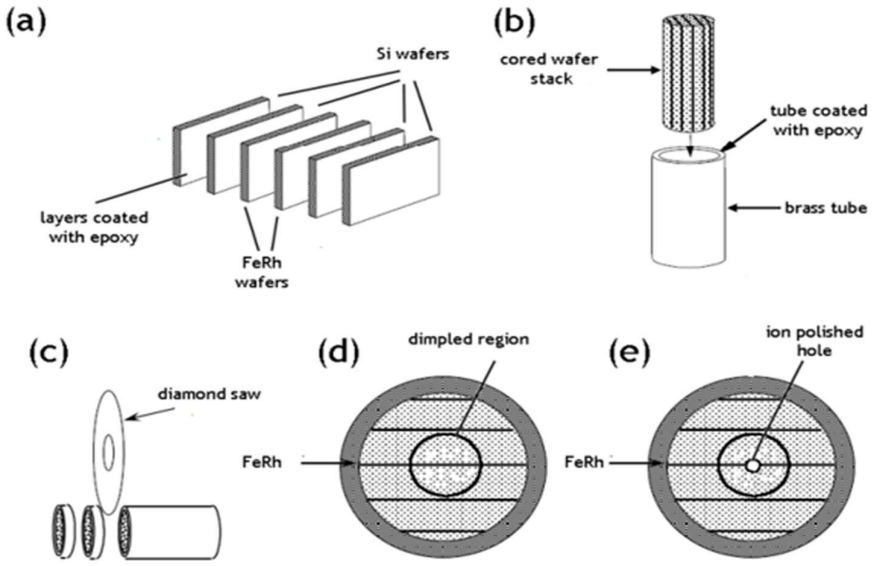

Figure 2.12: Schematic of the various stages of cross-sectional TEM sample preparation, by a conventional, mostly mechanical method. (a) The sample is cut into wafers and stacked together with silicon wafers cured together with epoxy. (b) A cylinder is cut out of the stack and encapsulated in a brass tube with epoxy. (c) Cross sections are cut from the tube and polished to ~100 μm. (d) The sample is dimpled until there is a ~10 μm thick region in the center of the sample. (e) The sample is ion polished on both sides until there is a small hole in the middle of the sample. At this point, the region around the edge of the hole is ~20-50 nm thick and thin enough for HRTEM imaging [80].

Cross-sectional TEM provides a far better picture of what is going on at and around interfaces. It can also be used to assess strain, interfacial diffusion, and changes in chemical composition across the sample. For metallic thin film samples, three procedures are available: ion polishing, focused ion beam, and tripod polishing. For our samples, we employed the ion polishing procedure, which we are going to go through in detail. Ion polishing is the conventional method and by far the preferred option. It produces exceedingly high-quality samples with minimum specimen damage despite the mechanical effort done to the sample and therefore, resulting in an incredibly narrow region of interest in the center of the sample. It is a lengthy procedure with numerous steps as compared to focused ion beam. Due to the mechanical nature of the preparation, it is also possible that the samples will break throughout the procedure. The process is depicted schematically in figure 2.12 [80].

An ultrasonic cutter with a 3 mm^2 attachment is used to cut off two regions of interest from a thin film sample. This produces a cross section that will be observed in the TEM along either the [100] or [110] direction. The wafers are then joined together using an epoxy glue,

with the thin sheets facing each other. To provide bulk for the following phase in the process, many layers of Si wafer cut using the previously described procedure are attached using epoxy on either side of the sample wafers. The epoxy is then cured in a vise at 130°C for an hour to drive out excess epoxy and ensure proper contact between the wafers. With the sample encapsulated in the tube, the sample is cut into 700 - 800 μm thick discs using a slow cutting diamond saw. A high thickness is originally chosen so that any potential damage from the cutting operation may be removed by grinding and polishing the sample. The sample is ground down on both sides using a disc grinder until the cross section is 70 - 100 μm thick. It is critical that both sides of the cross section stay parallel throughout this stage, because otherwise the sample's quality would suffer. To produce electron transparency, polishing, dimpling, and ion polishing are applied solely to the sample's substrate side.

Dimpling is done with the cross section which is 70-100 μm in thickness, a dimple grinder thins the middle of the sample but still provide structural stability to stop the sample from breaking. Ultimately, a ~10 μm thickness in the center is desired, so 35-45 μm must be removed from each side. The first 30-40 μm are polished using a copper grinding wheel combined with a 0.05 μm gamma alumina suspension as a polishing compound. The final stage of sample preparation is ion polishing, which comprises low energy polishing with a precision ion polishing system (PIPS). The PIPS employs an Ar+ source with a 2-5 keV energy range, progressively milling away the material with a modest incidence angle until a hole form in the center of the sample. Once a hole has formed, the energy of the ions can be lowered to 3 keV to softly polish the sample. Then, the cross-section is suitable for TEM analysis. The regions of interest near the hole's border will be 20-50 nm thick, which is ideal for atomic lattice imaging using HRTEM.

In this thesis TEM is used to gain insight into the structural quality and probe the nano structural assessment of the interfaces. We have used High-resolution Transmission Electron Microscopy (HRTEM) by using a JEOL 2010 UHR field emission gun microscope operated at 200 kV with a measured spherical aberration coefficient Cs of 0.47 ± 0.01 mm. Cross-sectional TEM specimens were prepared using conventional mechanical polishing followed by dimpling, and ion etching with Ar-gas with angle 6° and accelerating voltage 3.5 kV. We estimated the strain in the InAs QWs by using geometric phase analysis (GPA) [81]. In the GPA method, any shift of the atomic lattice relative to some reference lattice in an image is determined by mapping corresponding local shifts of diffraction peaks in the Fourier transform of the image.

The scripts implemented in the FRWR tools menu [82] for Gatan Digital Micrograph software was used to calculate the strain variation. [111] and [111] Bragg reflections were used to calculate the 2D symmetric strain map within the QW. A circular aperture around Bragg spots was applied to measure the strain map with a spatial resolution of 3 nm.

2.5 2-Dimensional Electron Gases

One of the most significant advances in semiconductors, both in terms of physics and in terms of device development, has been the realization of structures with basically two-dimensional (2D) electrical behavior. This means that, at least during some phases of the device's operation, the carriers are confined in a potential such that their motion in one direction is restricted and thus quantized, leaving only a two-dimensional momentum or k-vector describing motion in a plane normal to the confining potential. Metal oxide semiconductor (MOS) structures, quantum wells, and superlattices are the key systems in which such 2D behavior has been examined. A novel 2DEG was introduced in 1978 by Dingle and his coworkers which is formed by MBE grown AlGaAs/GaAs heterostructures [83].

The transport experiments reported in this thesis are based on the concept of two-dimensional electron gas (2DEG). This section describes the experimental realization of 2DEGs. The first experimentally produced 2DEG was formed in the inversion layer of a silicon is shown in figure 2.13; previous success has been obtained with MBE-grown remotely doped structures. The formation of a 2DEG in the instance of GaAs/AlGaAs single interface heterostructures is accomplished by properly doping a GaAs/AlGaAs heterostructure formed using MBE. A heterostructure is a layered sequence of two or more semiconductors with varying band gaps that are integrated in a single crystal. GaAs and AlGaAs are excellent candidates for heterostructure manufacturing since their lattice constants are almost identical: a_{GaAs}= 5.653Å and a_{AlAs}= 5.661Å at 300 K [84]. Figure 2.14 depicts the creation of a 2DEG in a GaAs/AlGaAs heterostructure in a schematic manner. The Fermi energy E_F of intrinsic GaAs is in the center of the gap between the valence band E_V and the conduction band E_C. It comes into touch with an AlGaAs doped layer, which has a wider band gap and is either uniformly or remotely n-doped. In equilibrium, E_F must be the same throughout the whole crystal, and the band structure self-aligns. The undoped GaAs conduction band is bent down at the interface between the two semiconductors, whereas the doped AlGaAs conduction band is bent up (lower half of Fig.2.14). As a result, a triangle potential well forms.

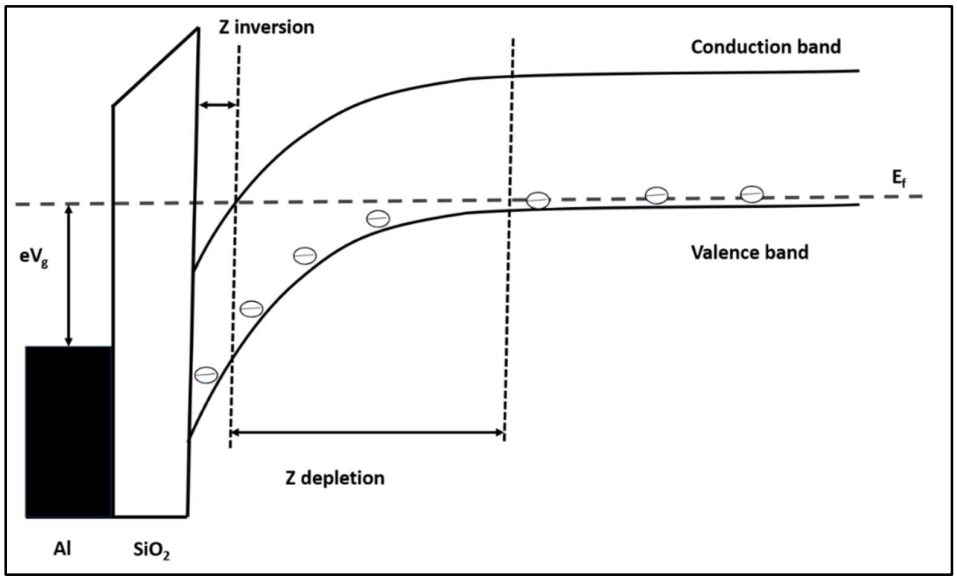

Figure 2.13: Energy diagram of a Si MOSFET (Metal-oxide-semiconductor field effect transistor) [85].

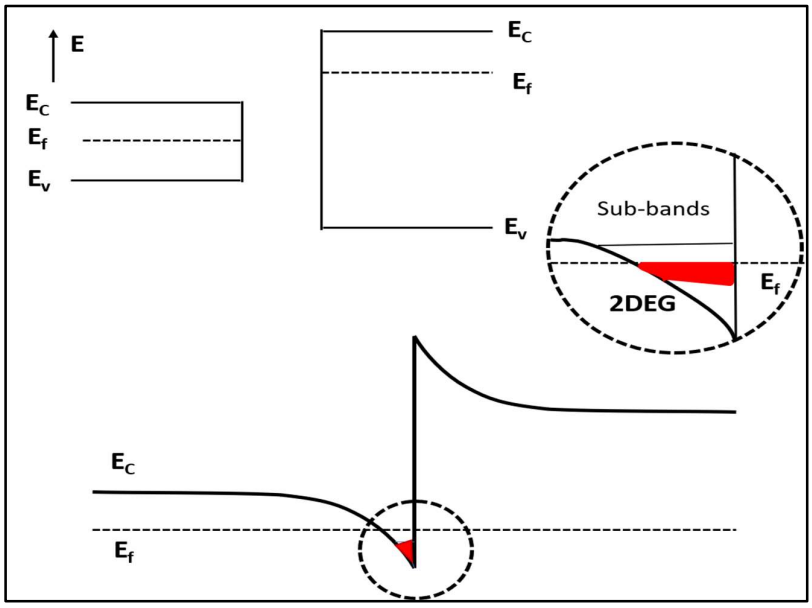

Figure 2.14: Sketch of the formation of a triangular potential well at the interface of two semiconductors with different band gaps.

The doping is introduced only in the high band gap material and may be separated from 2DEG by an undoped spacer layer. This is known as modulation doping. This has a great impact on the electron mobility since scattering by impurities is greatly suppressed and thus can yield low temperature mobility up to $10^7 cm^2/Vsec$ in GaAs/AlGaAs [86]. The mobility also

translates to the mean free path which in these structures, can reach up to ~350 micron [87]. A quantum well is created by sandwiching a thin layer of material with a smaller band gap (well) between two layers of material with a greater band gap (barriers) (see figure 2.15). To name a few III-V combinations, the pair of materials for the well/barrier construction can be GaAs/AlGaAs, InGaAs/InAlAs, InGaAs/InP, and InGaAs/GaAs. Because the well characteristics are under strong control and may be modified as needed, quantum wells have the benefit of being the most adaptable two-dimensional system. As a first approximation, the well is a rectangular potential profile whose width is controlled with monolayer accuracy (it is the thickness of the low band gap material) and whose depth is determined by the conduction band offset (CBO) between the well and the barrier materials. Figure 2.15 shows a self-consistent Poisson-Schrodinger calculation of the conduction band profile and the carrier density for one of the $In_{0.81}Ga_{0.19}As$ samples characterized in this thesis.

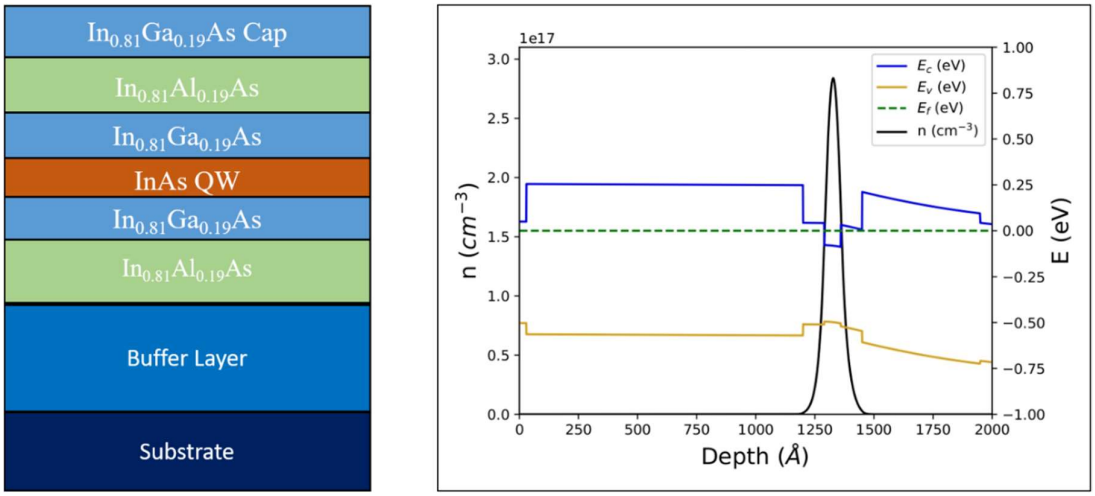

Figure 2.15: The image in the left shows the sketch of the layer sequence of the InAs Quantum well starting from the active layer then towards the substrate. The right graph is the profile of the calculated conduction band minimum along the growth direction (blue curve), and the carrier density profile (black curve); the horizontal green line is the Fermi level.

2.6 Device Fabrication

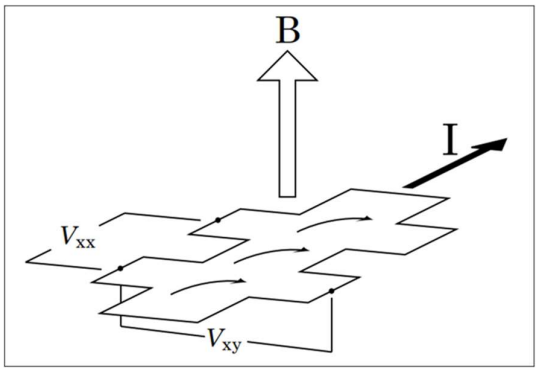

Figure 2.16: Typical Hall bar geometry used in transport measurements.

This section outlines the process used to create semiconductor heterostructure devices starting from an epitaxial 2DEG. These devices enable transport measurements to be taken on the 2DEG itself. The sample is patterned with suitably planned structures in the first manufacturing process. The geometry of the devices employed in this thesis, known as Hall bar geometry, and the common hall bar geometry is depicted in figure 2.16. This design is particularly suitable for studying the mobility and carrier density of 2DEGs using the traditional and quantum Hall effect. In this work electron beam lithography and a wet chemical etching method are generally used to define hall bars. The details of hall bar fabrication are in *Appendix 1.*

2.6.1 Electron beam lithography

Electron beams can be implemented to create smaller patterns with greater edge resolution than the finest photolithography. Electron beam lithography (EBL) employs the same principles as optical lithography in that a thin coating of polymer (often poly-methyl-meta-acrylate, or PMMA) is applied to the sample surface. When a polymer is subjected to a beam of high energy electrons (usually 30-100 keV), its chemical characteristics change, causing the exposed portions to become soluble (for positive resists such as PMMA) or insoluble (for negative resists such as SU-8) in a suitable solution. After dissolving the soluble section of the resist, the remaining resist-covered surface is shielded against subsequent process steps that are either subtractive (like etching) or additive (like metal deposition) as shown in figure 2.17. Moreover, electron beam technology has been developed for imaging purposes for

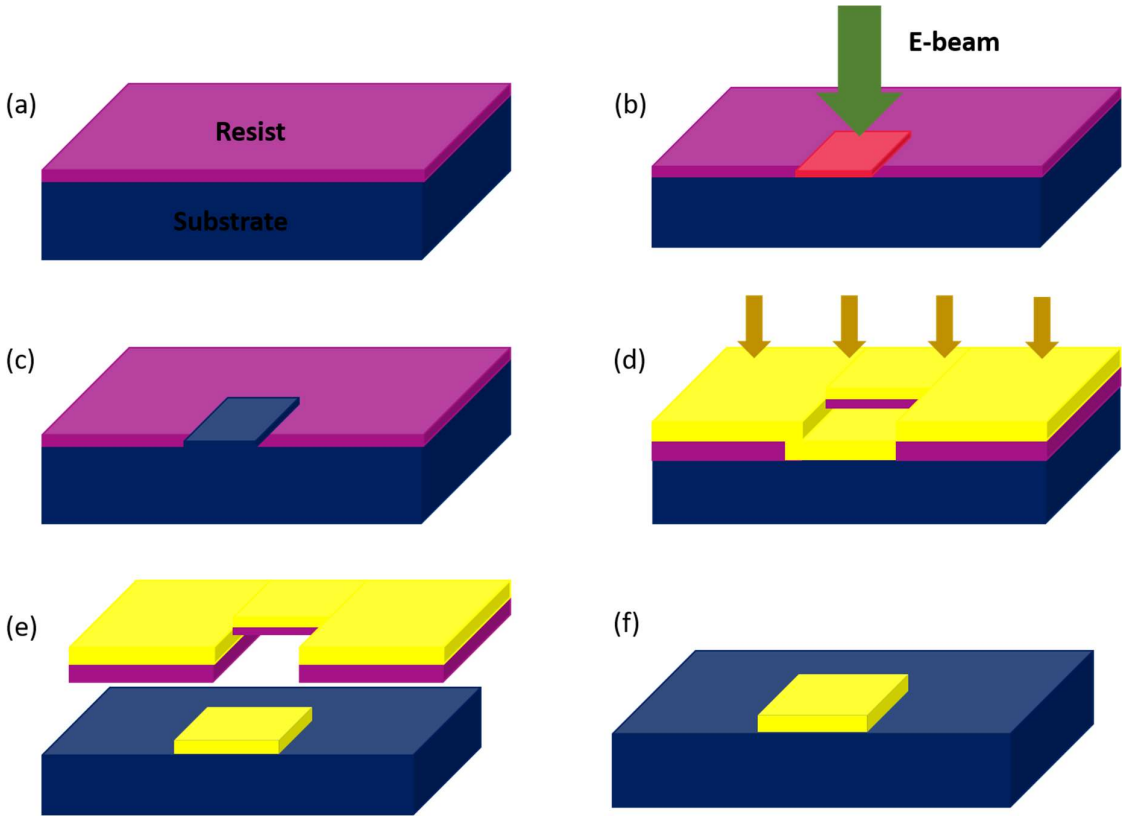

Figure 2.17: Basic steps involved in electron beam lithography. First, the electron beam resist is spin coated onto the sample surface, as in (a). The sample is then exposed by the electron beam in the desired pattern shape(s), as in Fig (b). The sample is developed so that the affected area of the resist is washed away (in the case of positive e-beam resist), as in Fig. (c). A subsequent etch, or in the case of Fig. (d), deposition step affects only the area of the wafer that no longer contains resist. The resist is lifted off, leaving a sample surface with the desired etch or deposition in only the desired areas (Fig. (e-f)).

scanning electron microscopes (SEMs) in the early 1960s [88,89], producing electron-optical columns able to raster an electron beam with a diameter of 1 nm with nanometer precision over millimeter wide areas. This gives unprecedented flexibility in pattern design and shortens the time from the pattern design to the transfer of the pattern on the sample, since the electron beam is directly writing the desired pattern on the sample. As a drawback, it being a serial writing method, EBL is unsuited to large scale serial fabrication, where the parallel production of thousands of identical patterns at a time by optical lithography is preferred. This main disadvantages of electron-beam lithography of limited throughput and hefty capital costs is being researched and will undoubtedly be producing less-expensive, higher-throughput devices

in the next two decades. In scientific research, though, where flexible design is a must and volume production are not needed, electron beam lithography comes very handy.

In this thesis, EBL has been extensively used to define small (in the range 1 μm to ∼10 nm) features on the surface of the samples. Limited data show that the critical yield determinant, pattern defect density, may be lowered and machines can be designed to produce economically. This newer electron-beam technology is coming from the lab to build the next generation of lithography and quality control tools for microelectronic device manufacturing.

2.7 Transport measurements

Electron mobility is a fundamental parameter to define a 2DEG quality, being one of the benchmarks to assess the magneto-transport behavior of a 2DEG and all associated phenomena. Electron mobility and its scaling with certain parameters like sample temperature, 2DEG electron density, QW width etc. allows to draw conclusions about the type and relative influence of scattering mechanisms the 2DEG is subject to, and from there to the crystal's properties and quality itself. It is also well established that, given comparable structures, growth parameters and MBE setup conditions. An advantage of electron mobility as a characterization number is its easy accessibility: a relatively simple magneto-transport setup at the temperature of liquid helium will allow to calculate μ from easily measurable sample properties. With electron mobility commonly obtained from a Hall bar measurement, it is easily determined with the van der Pauw method that was presented by Leo J. van der Pauw in 1958. The method allows deriving the (three-dimensional) resistivity ρ of an arbitrarily shaped bulk sample solely by four-point resistance measurements.

There are four conditions that must be respected to have meaningful use of the van der Pauw method.

1. The sample should have flat shape and uniform thickness.

2. No isolated holes should be present in the sample.

3. A homogeneous and isotropic sample must be considered.

4. All four contacts must be located at the edges of the sample.

Other than these conditions we must be careful that the measurement contact surface should be at least an order of magnitude smaller that the surface area of the entire sample. For very small

surfaces where the contact surface cannot be neglected additional geometric correction factors are to be added. The resistivity and hall mobility of our samples were determined by using van der Pauw structures with the help of the probe station with four probe heads and SR830 lockin amplifier, the output voltage is recorded. This approach includes passing a current via four tiny contacts around the circle of a flat, square-shaped sample of uniform thickness. Because the geometric spacing of the connections is immaterial, this approach is particularly suitable for measuring very tiny samples. The effects of sample size, which is the approximate probe spacing, are insignificant.

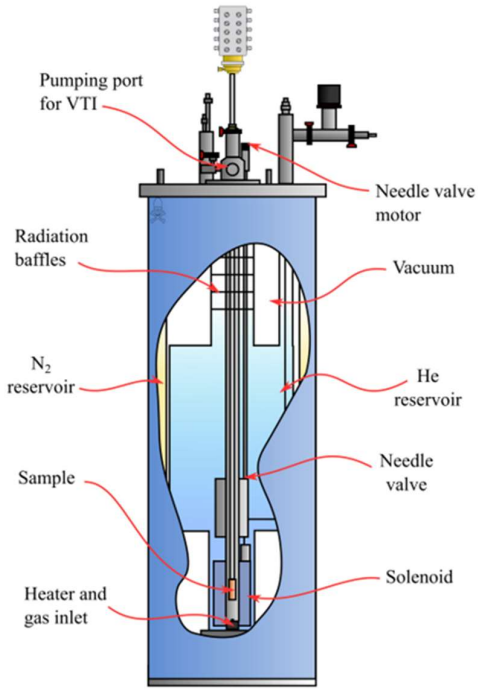

Figure 2.18: Schematic diagram of the ^{4}He cryostat used in this thesis [90].

The transport properties of the fabricated devices (hall bars and Josephson junctions) were investigated using a variable temperature ^{4}He cryostat for experiments from ambient temperature to 1.4 K and magnetic fields up to 7 T. The sample holders enable measurements to be taken in a magnetic field that is either perpendicular or parallel to the sample. The sample in the ^{4}He cryostat is cooled by thermal exchange with cold ^{4}He vapors from the cryostat's liquid ^{4}He reservoir (shown in Figure. 2.18). It is possible to cool the sample to 4.2 K in this manner. Further cooling can be accomplished by lowering the pressure in the chamber containing the sample to a few mbar. As a result, the ^{4}He from the reservoir undergoes adiabatic

expansion, lowering its temperature to 1.4 K. Carrier density n and mobility μ of a 2DEG are measured in a four-wire setup, which is schematically described in Fig. 2.16. A current I is driven through the main channel of the Hall bar. At zero magnetic field (B=0), the potential drop V_{xx} induced by the current between two lateral contacts is measured. From V_{xx} it is possible to obtain the longitudinal resistivity, ρ_{xx}, of the 2DEG as

$$\rho_{XX} = \frac{V_{XX}}{I} * \frac{w}{L} \tag{2.12}$$

where w and L are the width and length of the Hall bar, respectively. The dimensions of the typical Hall bars used in this thesis are w = 19 μm and L= 40 μm. If a magnetic field B perpendicular to the plane of the 2DEG is applied, the Lorentz force, $\vec{I}\,X\,\vec{B}$, induces a potential drop V_{XY} between two transverse contacts (classical Hall effect). From the Drude model [14] it is than possible to obtain the following relations:

$$\rho_{XX} = \frac{1}{en\mu} \tag{2.13}$$

$$n = \frac{B}{e} * \frac{1}{V_{XY}} \tag{2.14}$$

where n is the carrier density of the 2DEG. Combining Eqs. (2.13) and (2.14) with Eq. (2.12) results in the mobility μ of the 2DEG,

$$\mu = \frac{V_{XY}}{V_{XX}} * \frac{L}{B.w} \tag{2.15}$$

The characterization of 2DEG mobility and carrier density is typically done at T= 4 K with a magnetic field B of 0.3 T for Vander pauw measurements, and at T= 1.5 K with Magnetic field up to 12 T for devices such as hall bars and Josephson junctions. These measurements are typically performed using a conventional four wire lock-in technique with an AC excitation current of 100 nA at a frequency of about 20 Hz.

Chapter 3

Growth of high mobility InAs 2DEGs

One of our main goals in this work was to grow high electron mobility 2DEGs in virtually unstrained InAs QWs. To reach this result we had to develop a virtual substrate, nearly lattice-matched with InAs, bearing no crystal defects, and grown on a commercially available material. InAs has a lattice parameter of 6.0584Å and when we compare it with GaAs it has a significant percentage change of 7.17%. This lattice mismatch needs to be accommodated as direct growth of one material over the other would result into dislocations and/or 3D nucleation, depending on the amount of mismatch [91,92]. This purpose can be accomplished by the insertion of $In_xAl_{1-x}As$ graded buffers to accommodate InAs QWs on GaAs substrates. In this work we have used the quantum well thickness of 7nm, therefore to sustain the additional strain created by making the InAs QW thicker, we increased the In composition of the InGaAs and InAlAs regions from 0.75 to 0.81 as compared to the previous works done at IOM [46,93–95]. Section 3.1 reviews briefly the main problems encountered when trying to perform lattice-mismatched growths, particularly focusing on III-V semiconductor systems. Section 3.2 describes the growth procedures involved in the samples grown for this work. In Section. 3.3 we describe the structural properties of our $In_xAl_{1-x}As$ buffers analyzed by X-Ray Diffraction (XRD) and cross-sectional Transmission Electron Microscopy (TEM) and the morphology of surfaces and interfaces are analyzed in Section 3.4 using Atomic Force Microscopy (AFM).

3.1 Lattice-mismatched growth

Different semiconductor crystals have different lattice characteristics and even different crystal structures. This makes it extremely difficult to produce heterostructures without any crystal defects. The most well-known exceptions are GaAs, AlAs, and other related alloys. Not only do GaAs and AlAs crystals share a zinc-blende structure, but their lattice properties differ so little that almost any thickness of any alloy of these binaries may be formed without concern

for strain building. Furthermore, because the band gaps of GaAs and AlAs are dissimilar, conduction-band engineering in AlGaAs/GaAs systems is simple. GaAs/AlGaAs multilayers can be easily fabricated using various techniques (such as MBE, MOCVD) and we get extremely high mobility 2DEGs in modulation doped single heterointerfaces, [96] high mobility 2-Dimensional Hole Gases [97], 2DEGs in almost arbitrarily shaped quantum wells, coupled 2DEGs in multiple quantum wells and very high quality superlattices

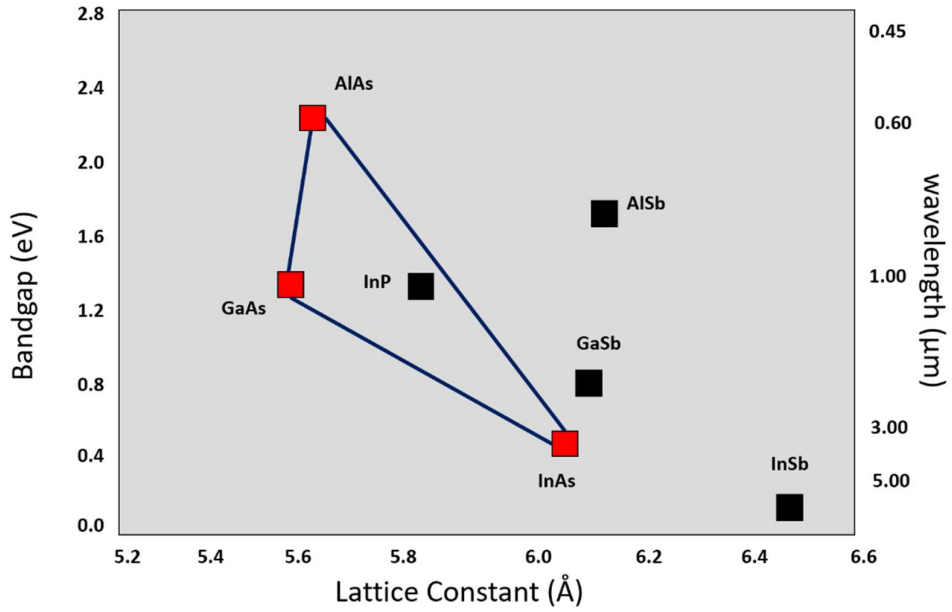

Figure 3.1: Band gaps and lattice parameters of the binary semiconductors used in this work. (This figure is re-elaborated from the book Physics of Semiconductor Devices [98].)

As can be seen in figure. 3.1, the situation for InAs (and thus $In_xGa_{1-x}As$ alloys) is not as good: the lattice mismatch between InAs and the most common III-V commercial substrate, GaAs, is huge (almost 7%), and with InP (the other most common commercially available substrate) it is more than 3%. The only possible lattice-matched growth of an $In_xGa_{1-x}As$ alloy is with x = 0.53 on InP. The main reason for choosing GaAs is its higher resistivity ~10^8 Ω.cm compared to InP ~10^7 Ω.cm [https:// eesemi.com] also less expensive than InP. Therefore, it is an advantage for high frequency applications. Also, it was not a suitable choice in our MBE setup for two reasons: first, our target was $x \geq 0.81$, so strain buildup would have been a problem anyhow; second, phosphorus is a contaminant for high mobility 2DEGs in GaAs/ AlGaAs, so InP cannot be used as substrate in our MBE chamber. Thus, the only choice has been using GaAs as a substrate, and find a way to relax the strain to grow $In_{0.81}Ga_{0.19}As$ layer with a low defect density in the active region of the structure.

3.1.1 Formation of Heterostructures

Because of the lattice mismatch, we require a virtual substrate, and if we begin developing an epilayer with a different lattice parameter than the substrate, strain will accumulate in the epilayer. When the epilayer has a greater lattice parameter than the substrate (as is the case for $In_xGa_{1-x}As$ grown on GaAs), this strain is compressive, the initial atomic layers of the growing film have the in-plane lattice parameter matched to that of the substrate, and the out-of-plane lattice parameter expanded to accommodate the mismatch (also known as *Pseudomorphic* growth).

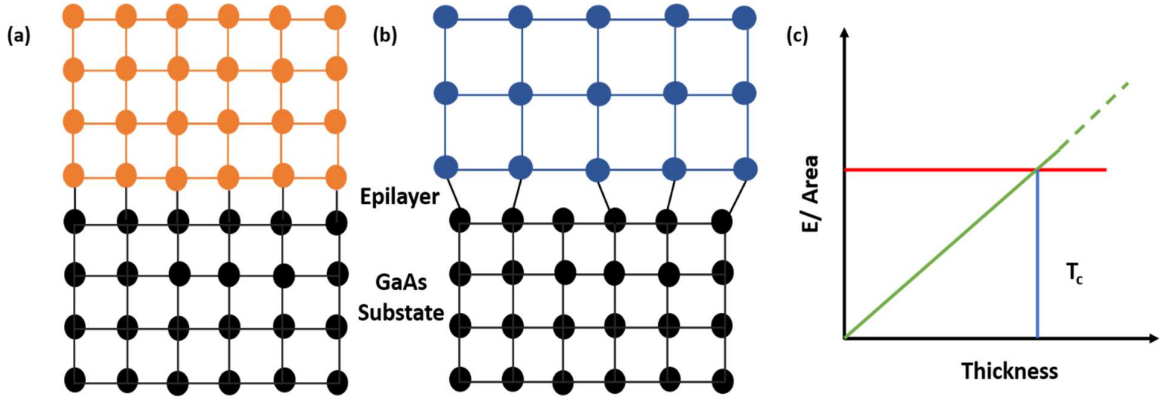

Figure 3.2: Shows the difference between materials whose lattices match the substrate and can be deposited with no strain relief (a) and individual linear defects that accommodated the strain between slightly mismatched layers showing misfit dislocations (b). (c) shows the graph of elastic energy per unit area versus epilayer thickness for (b). The horizontal red line represents the critical energy for dislocation formation.

This comes at a cost in terms of energy, since elastic energy accumulates within the crystal. When the elastic energy surpasses the energy cost of a crystal defect, the defect becomes energetically favorable and spreads across the epilayer-substrate interface. This procedure is illustrated in figure 3.2. (c) The thickness at which defects begin to form is known as the critical thickness. There are several equilibrium models to predict the critical thickness of a strained layer, but MBE growth is far from equilibrium, and critical thickness calculations must rely on growth specific parameters.

The growth of an epilayer beyond the critical thickness, with the formation of crystal defects that lead to the relaxation of the epilayer, is referred to as metamorphic. These buffer layers are grown to provide a virtual substrate with the desired lattice constant on which

subsequent device layers with low dislocation density can grow (metamorphic growth). Buffer layer growth is initiated on a standard commercial substrate, and the composition is either gradually or stepwise changed to achieve, or at least approach, the final different lattice constant, since the goal is to achieve a relaxed layer as the virtual substrate. For our samples with such a large lattice mismatch, we grow a buffer layer first where strain relaxation through misfit dislocation (MD) formation takes place to obtain a virtual substrate lattice-matched to $In_{0.81}Ga_{0.19}As$ as shown in figure. 3.2. Therefore, the optimization of this buffer layer is the important part of this chapter.

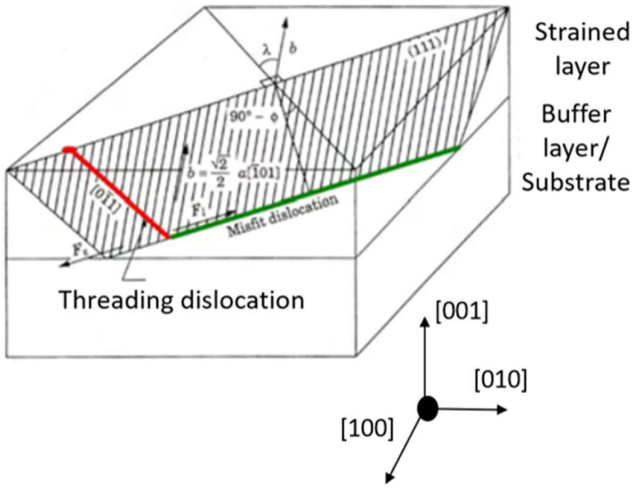

Figure 3.3: Shows a threading dislocation: the TD (drawn in red) originates from a MD (green line) lying in the [001] plane and runs all the way to the free surface [99].

Another defect commonly associated to strain relaxation is the so-called threading dislocation (TD), which is a MD which forms on a plane that is not the growth plane [99]. Figure 3.3 schematically represents a TD running through a strained layer grown in the [001] direction; in this example the TD, running along the [0-11] direction, originates at the interface between the substrate and the strained layer at the end of a normal MD aligned along [-110]. This kind of dislocations is to avoid, since they propagate all the way to the surface, and are detrimental for most semiconductor applications: they are sources of scattering for electrons and holes. This is true also for MDs, but the fact that they form at the interface between the substrate and the grown layer allows to keep them at a safe distance from the active layer, thus reducing their potential harm.

Therefore, to grow the dislocation-free lattice mismatched layers there are two strategies:

1. for small lattice mismatch: to grow *pseudomorphic* strained layers below the critical thickness;
2. for large lattice mismatch: to grow first a buffer layer where strain relaxation through MD formation takes place, i.e. to obtain a virtual substrate lattice-matched to $In_xGa_{1-x}As$. So, the optimization of the buffer layer is the main part of this chapter.

3.1.2 Previous work on the growth of semiconductor heterostructure at CNR-IOM:

Several investigations have been carried out to better understand the mechanics of strain relaxation in $In_xGa_{1-x}As$ or $In_xAl_{1-x}As$ layers in cases where a lattice mismatch to the substrate exists at CNR and they were inspired by some old works on GaAs substrates to reduce the strain in the quantum well region [100,101] . It was shown that a defect-free region with an arbitrary indium concentration can be obtained on GaAs substrates by inserting a step- or linear-graded buffer layer (BL) with increasing In composition to smoothly adapt the substrate's lattice constant to the one of the top layer. This relaxes the strain and it buries the dislocations away from the top layers making them defect-free epitaxial layers. The low temperature development of the BL [102] and the insertion of an AlGaAs/GaAs superlattice between the GaAs substrate and the BL [103] appear to be the key parameters in achieving this goal. Then BLs were grown the on GaAs substrates to almost unstrained $In_xGa_{1-x}As$ QWs, (with $x \geq 0.7$) containing a 2DEG. [104–106] In these cases, the BL indium concentration was at the most equal to that of the QW. The increasing indium concentration of the buffer up to values greater than the target concentration of the active layers has already proven to be beneficial in InAlAs/InGaAs metamorphic QWs. [95] Also, From the previous works we have also increased the InAs QW thickness from 4 [107] to 7 nm [47] allows to increase the fraction of the 2DEG density contained in the binary QW region from 45% to 69%. The mobility and carrier density achieved in these samples were 3.5×10^5 cm^2 /Vs at $n = 5.3\times 10^{11}$ cm^{-2} and then with the change in the QW thickness we achieved electron mobility of 7.1×10^5 cm^2 /Vs at $n \sim 3 \times 10^{11}$ cm^{-2} [47]. This work was our starting point towards high mobility heterostructures.

3.1.3 Samples Grown for this work:

To ensure the formation of a metamorphic, dislocation-free QW region of $In_xGa_{1-x}As$, we have grown step-graded $In_xAl_{1-x}As$ BLs with increasing indium concentration x on GaAs (001) wafers to favor the accommodation of the QW lattice parameter on the GaAs substrate. The

growth procedure divided in three phases characterized by different growth temperatures (represented in figure. 3.4) [46,47,108]:

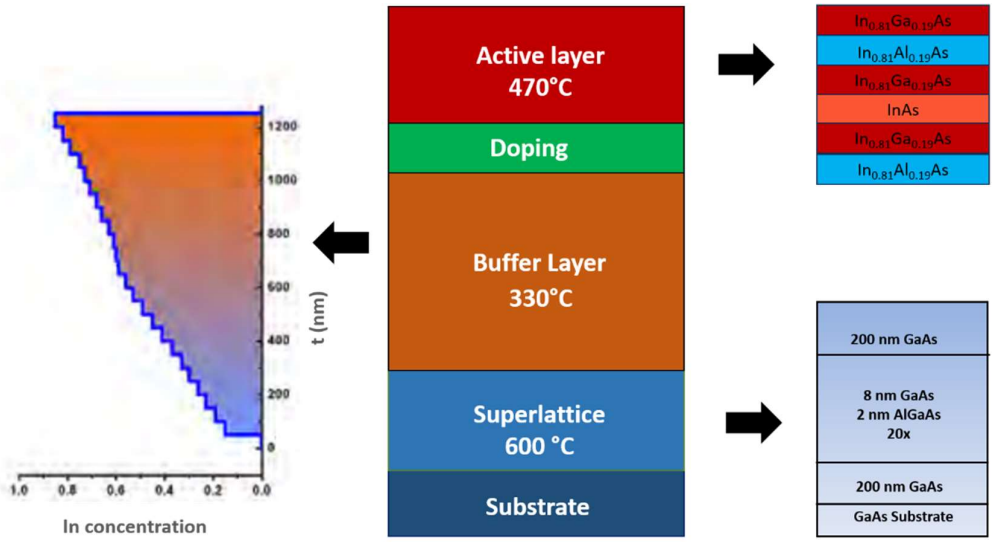

Figure 3.4: Growth sequence of the InAs/GaAs samples. In the middle, a schematic view of the three parts of the growth. Each part is expanded on the sides. The buffer layer composition is shown on the left, where the vertical axis represents the distance from the top of the interfacial layer, and the horizontal axis is the indium concentration x. The active layer and the GaAs/AlGaAs superlattice are shown in right.

1) Substrate preparation: For the preparation of substrate, we degas an GaAs (001) (shown in fig) wafer at 580°C to remove the surface oxide. Then we grow a 200 nm thick undoped GaAs layer on the top of wafer which was then followed by a 20 period GaAs/ $Al_{0.33}Ga_{0.67}As$ (8 nm/ 2 nm) superlattice. Then we again grow a second 200 nm undoped GaAs layer at 600°C. These three layers helps to reduce the wafer roughness, the diffusion of interface impurities in the grown layer, and reduces the risk of threading dislocation formation during the growth of top layers [103]. Growing these layers at high temperature gives optimal quality GaAs.
2) Buffer Layer: For the growth of the buffer layer the substrate temperature is decreased to 330°C as the low growth temperatures decrease the decrease roughness, since the cross-hatch that develops from the dislocations is growing more at high temperature, [109] where we can have faster surface kinetics. This growth temperature has been optimized based on transport measurements. The inspiration of this buffer layer sequence has been derived from the work of Gozu and coworkers [106] initially and then it was modified at our labs in several years. Their graded buffer is substantially the same as ours up to x =

0.81. At this indium concentration they end the buffer and start the growth of the active layer. However, according to our experimental findings and the strain relief model described ahead, this is insufficient to completely release the strain accumulated in the buffer. The result is a residual compressive strain to which the active layer is subject with consequent mobility reduction (shown with XRD results in next section). In our buffer layer we have then increased the indium fraction x over 0.81, with the aim of relaxing more effectively the active layer.

The 1.2 μm-thick $In_xAl_{1-x}As$ buffer layer is grown in 50 nm steps with increasing indium concentration, starting from x=0.15 to x=0.81. The increase in x between each step is not constant throughout the buffer, but is ∼0.035 up to ∼60% and then it is decreased to ∼0.015 up to the end of the buffer. The In concentration is adjusted by raising the In cell temperature while keeping the Al flux constant; there is no growth pause between stages, therefore the interface is not abrupt, because the In cell temperature rise and subsequent flux stabilization take many seconds. This buffer layer is terminated by a top $In_{0.84}Al_{0.16}As$ step (thus with In composition higher than the $In_{0.81}Ga_{0.19}As$/ $In_{0.81}Ga_{0.19}As$ barriers) of thickness t as shown in the figure 3.5 (a), with t varying from 50 nm to 300 nm to tune the strain in the quantum well region (Figure 3.5 (a)). Even though no intentional doping is introduced in the growth, the QWs are intrinsically n-type. This has already been shown by our group in previous works and is because of the deep donor impurities in the $In_{0.75}Al_{0.25}As$ layers. [107]

3) Active layer: The QW region consists of a 7 nm thick InAs quantum well embedded in a double $In_{0.81}GaAs/In_{0.81}AlAs$, grown at 470°C. [47] Increasing the InAs QW thickness from 4 [95], to 7 nm allows to increase the fraction of the 2DEG density contained in the binary QW region from 45% to 69% (as can be seen in the 1D Poisson-Schrodinger simulation of figure 3.5 (b)), thus reducing effects of interface and alloy scattering on electron transport. The Quantum Well is sandwiched between two $In_{0.81}Ga_{0.19}As$ barriers of 9nm, followed by a 117nm thick $In_{0.81}Ga_{0.19}As$ layer so that we have quantum wells buried under a thick layer minimizing the surface effects. Then a 3 nm-thick $In_{0.81}Ga_{0.19}As$ capping layer is grown to protect the surface from oxidation. Here our Quantum well is ~ 130 nm from the top layer.

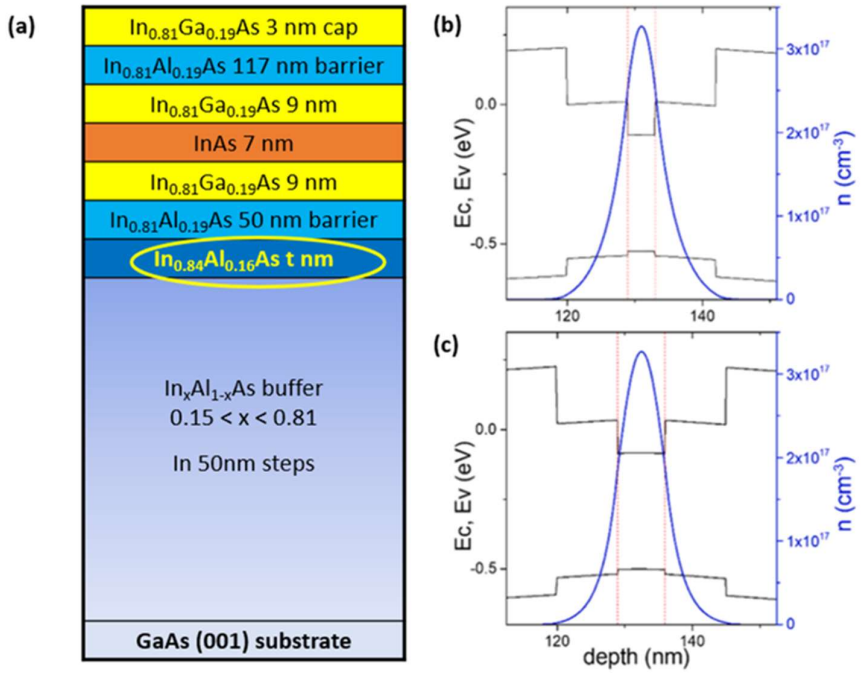

Figure 3.5: Shows the Schematics of the growth sequence. The InAlAs buffer layer 't' altered in this work is marked in yellow circle (b, c) Shows the 1D P-S simulations [110,111] of a 4 nm (b) and 7 nm (c) InAs/$In_{0.84}Ga_{0.16}As$/$In_{0.84}Al_{0.16}As$ QW. Valence and conduction band profiles are indicated in black, while 3D electron density is indicated in blue. Boundaries of the InAs QWs are marked as vertical red dashed lines. A ~ 3×10^{16} cm^{-3} n-type background doping was assumed in the $In_{0.84}Al_{0.16}As$ barriers [47].

3.2 Structural properties

We have performed XRD and TEM measurements to assess the structural properties of our sample with different 't' varying from 50 nm, 150nm and 300 nm to tune the strain in the quantum well. We have used experimental TEM and XRD results to compare the strain in the QW region.

3.2.1 XRD

To quantify the residual strain on the active layer we have performed High Resolution XRD measurements in a series of samples with different thickness t of the top $In_{0.84}Al_{0.16}As$ buffer layer. Three samples with t = 50 nm, 150 nm and 300 nm were chosen for HRXRD measurements. Strain analysis is done using Vurgaftman's data [75]. Figure. 3.6 shows ω-2θ rocking curves of (004) reflection. The broad feature at lower angles with respect to GaAs

comes from emission of the buffer layer, with two distinct peaks emerging on the left-end side, corresponding to both $In_{0.81}Al_{0.19}As$ and $In_{0.84}Al_{0.16}As$ regions. A broad and weak feature at around 30° is visible in the (004) reflection and ascribed to InAs emission, while it rises just above noise level and it is rather difficult to assess in (224) (not shown). An overall shift of (004) peak positions of InAs as well as InAlAs layers towards GaAs substrate peak indicates the reduction of out-of-plane strain (higher lattice relaxation) with increase of underlying $In_{0.84}Al_{0.16}As$ buffer layer thickness, which agrees with our previous observations [47]. Dashed lines in the figure clearly indicates peak shifts for both $In_{0.81}Al_{0.19}As$ and $In_{0.84}Al_{0.16}As$ as t increases from 50 nm to 300 nm. Within this broad buffer layer feature, a peak emerges at about $\omega \approx 31.4°$, which is due to the accumulation of $In_xAl_{1-x}As$ steps with x around 0.6 in the design of the BL [46], and slightly shifts to the right with increasing t similarly in the 0.81 and 0.84 regions, because of a different strain propagation within the buffer layer.

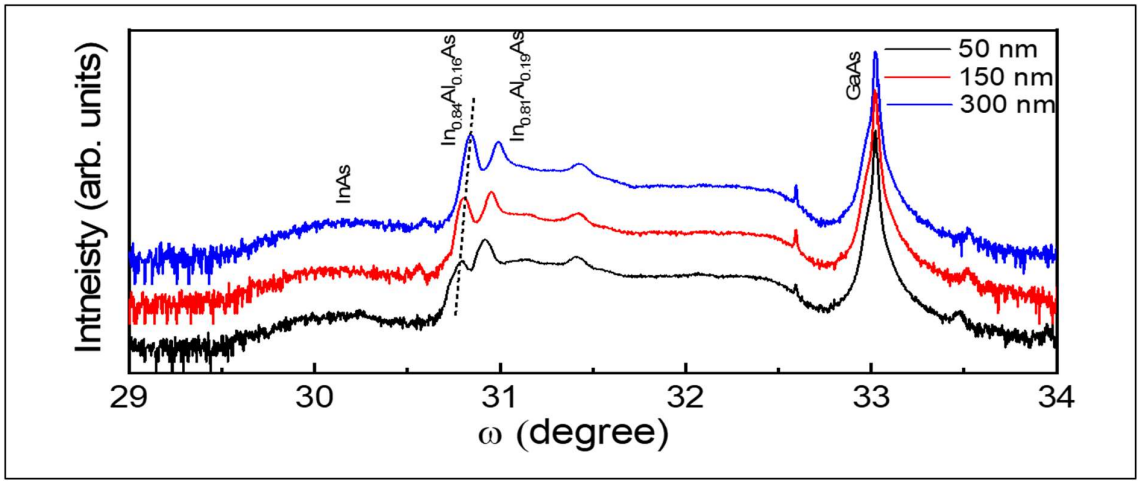

Figure 3.6: ω-2θ rocking curves on (004) reflection of InAs QWs with different $In_{0.84}Al_{0.16}As$ buffer layer thickness, as indicated.

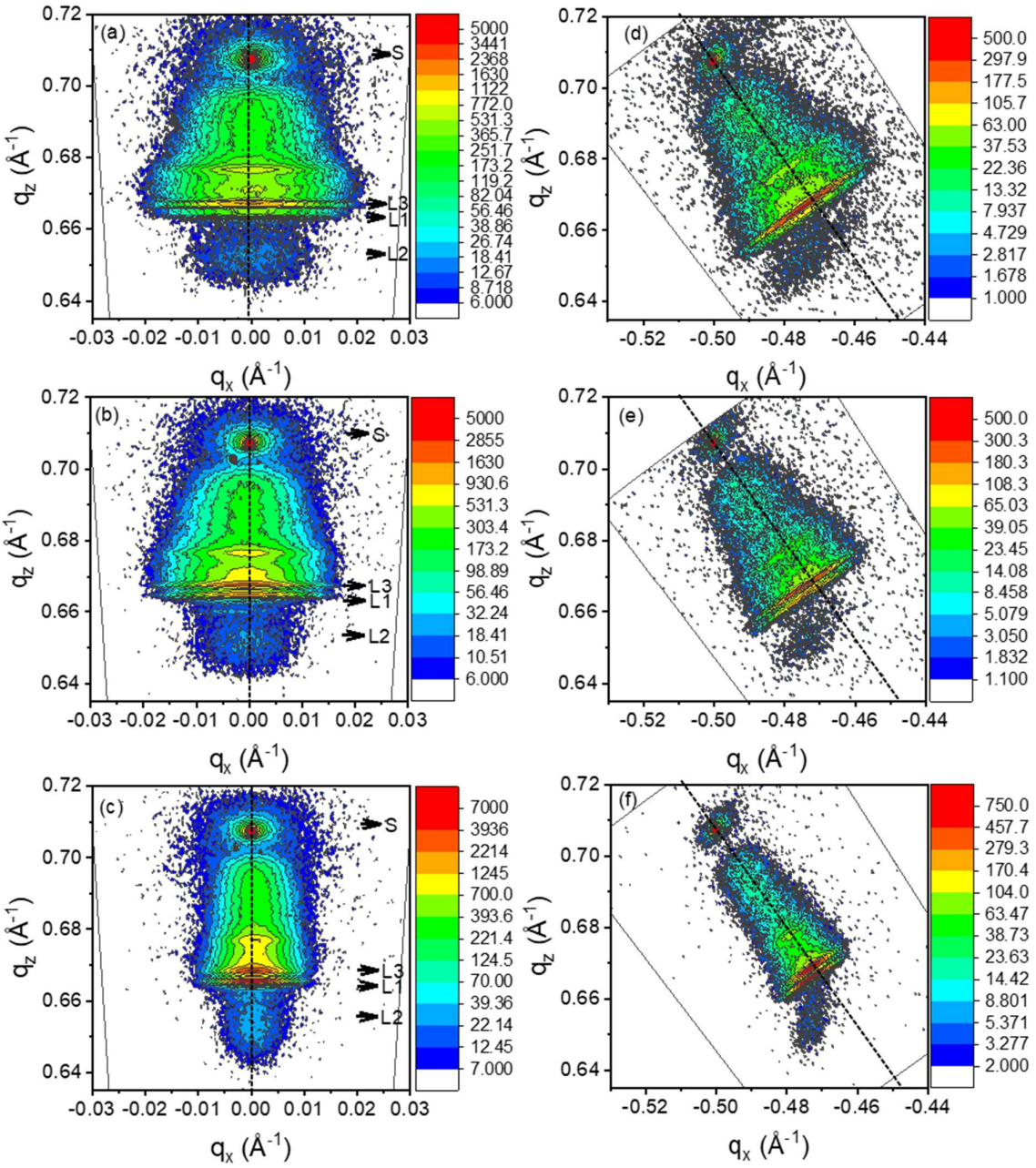

Figure 3.7: Shows Reciprocal space maps of symmetric (004) reflection (a-c) and asymmetric (224) reflection (d-f) of InAs QWs with $In_{0.84}Al_{0.16}As$ buffer layer thickness (a, d) 50 nm (b, e) 150 nm and (c, f) 300 nm. Corresponding peaks of substrate, $In_{0.84}Al_{0.16}As$, InAs and $In_{0.81}Al_{0.19}As$ peaks were labelled as S, L1, L2 and L3, respectively.

To further study the strain, lattice relaxation and mosaicity of all the layers in detail, particularly the InAs QW region, Reciprocal Space Maps (RSM) of (004) and (224) reflections were performed and plotted in reciprocal coordinates, as shown in Figure. 3.7 (a)-(f). The reciprocal

space co-ordinates of the scattering vector (q_x, q_z) are related to the incident angle ω and scattering angle 2θ as [112].

$$q_x = \frac{1}{\lambda}\left[\cos(\omega) - \cos(2\theta - \omega)\right] \tag{3.1}$$

$$q_z = \frac{1}{\lambda}\left[\sin(\omega) + \sin(2\theta - \omega)\right] \tag{3.2}$$

The out-of-plane and in-plane lattice parameters $a_\perp$ and $a_\parallel$, respectively were obtained for each layer from their respective (q_x, q_z) coordinates of (224) reflection using the relations [113,114]:

$$a_\parallel = \frac{2\sqrt{2}}{q_x}\ ;\ a_\perp = \frac{4}{q_z} \tag{3.3}$$

These equations provide an effective way to estimate both $a_\parallel$ and $a_\perp$. It may be mentioned that $a_\perp$ can also be calculated from (004) coordinates, which is nearly similar, as all the samples were aligned with respect to the GaAs substrate. It was found that the $a_\perp$ decreased, while $a_\parallel$ increased monotonically with increase of buffer layer thickness for all the layers including InAs QW layer, which indicates the presence of biaxial strain in all the layers due to the tetragonal distortion in cubic lattice geometry. [114]The corresponding out-of-plane strain ($\varepsilon_\perp = (a_\perp - a_0)/a_0$) and in-plane strain ($\varepsilon_\parallel = (a_\parallel - a_0)/a_0$) were also calculated for all the layers, which are summarized in Table 3.1 and plotted in Figs. 3.8 (a) and (b), respectively. In the calculations of $\varepsilon_\perp$ and $\varepsilon_\parallel$, a_0 is the standard lattice parameter, which is estimated from Vegard's Law (discussed above) for each layer depending upon their In concentration. The data are shown in Table 3.1 and elaborated from Figure 3.8 (a) $\varepsilon_\perp$is tensile for all the layers, and is decreasing and tending to relax with increasing buffer layer thickness. In contrast, $\varepsilon_\parallel$ (Table 3.1 and Figure 3.8 (b)) is compressive for almost all the layers and it is also tending to relax with increasing buffer layer thickness. These observations confirm the biaxial nature of strains in all the layers. Note that the InAs layers were highly strained compared to InAlAs ones yet less strained in QW with 300 nm buffer layer compared to the QW lower thickness buffer layers. These strain values are in coherence with the literature. [47] In an ideal case of pure biaxial strain in zinc blend cubic lattice, $\varepsilon_\parallel$ is expected to commensurate with $\varepsilon_\perp$ ($\varepsilon_\perp = -\frac{2C_{12}}{C_{11}}\varepsilon_\parallel$; C_{12} and C_{11} are elastic constants). The proportional constant slightly differs but the phenomenon of biaxial strain holds in this scenario.

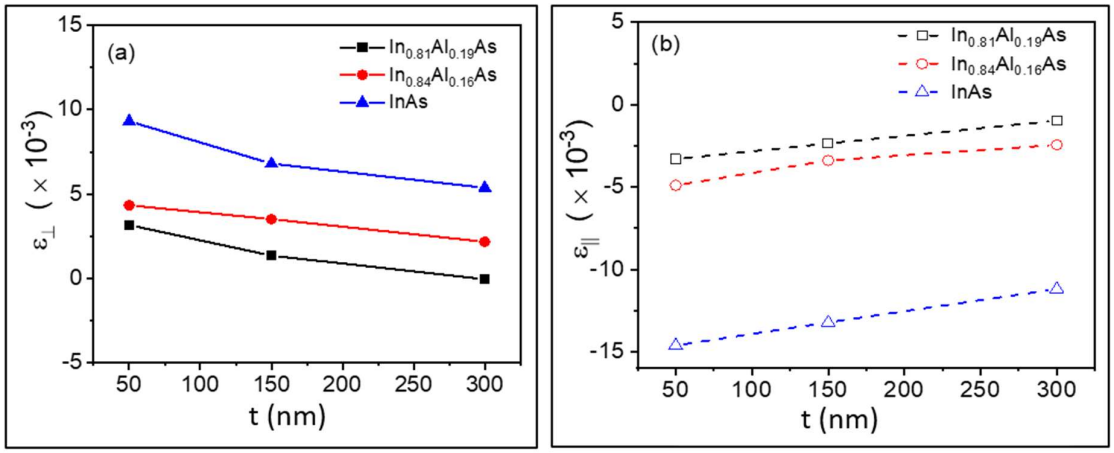

Figure 3.8: Shows the (a) Out-of-plane strain ($\varepsilon_\perp$) and in-plane strain ($\varepsilon_\parallel$) values for InAs, $In_{0.84}Al_{0.16}As$ and $In_{0.81}Al_{0.19}As$ layers obtained from reciprocal space maps.

Table 3.1: Shows the summary of $\varepsilon_\perp$ and $\varepsilon_\parallel$ values for InAs, $In_{0.84}Al_{0.16}As$ and $In_{0.81}Al_{0.19}As$ layers obtained from reciprocal space maps.

t (nm)	$\boldsymbol{\varepsilon_\perp}$ (×10^{-3})			$\boldsymbol{\varepsilon_\parallel}$ (×10^{-3})		
	InAs	**$In_{0.84}Al_{0.16}As$**	**$In_{0.81}Al_{0.19}As$**	**InAs**	**$In_{0.84}Al_{0.16}As$**	**$In_{0.81}Al_{0.19}As$**
50	9.3	4.3	3.2	-14.6	-4.9	-3.3
150	6.8	3.5	1.4	-12.2	-3.4	-2.3
300	5.4	2.2	-0.03	-11.2	-2.4	-1.0

The asymmetric (224) RSMs (Figure. 3.7 (d-f)) also reveals partially strained (not relaxed) InAs layers in all the samples. Black dashed lines in Figure 3.7 (d-f) are the joining lines between reciprocal lattice points of the substrate and the origin of reciprocal space, on which the reciprocal lattice points of fully relaxed epilayers are expected to fall. The reciprocal lattice points of InAs are tending closer to the line of fully relaxed state, with increase of buffer layer thickness. The degree of lattice relaxation (R%) was for InAs QW layers was quantified by using the relation [112,114]:

$$R\% = \frac{(a_\parallel - a_s)}{(a_{FR} - a_s)} \times 100 \qquad (3.4)$$

where $a_\parallel$ is the in-plane lattice parameter, a_{FR} is the lattice parameter of the fully relaxed epitaxial layer and a_s represents the substrate lattice parameter (GaAs). The estimated R% for

InAs layers as well as InAlAs layers were summarized Table 3.2. As seen in Table 3.2 the R% for InAs layers increasing from ~78% to 83% with increase of buffer layer thickness, indicating the partially strained nature but tending to relax (fully relaxed ~ 100%) with increase of buffer layer thickness. This is expected as the lattice mismatch is decreasing with increase of buffer layer thickness (Figure. 3.8 (a)). Similar observation is true for InAlAs layers also but with a higher degree of relaxation, as can also be observed from Figure 3.7 (d-f) and seen in Table 3.2.

Table 3.2: Shows the summary of degree of lattice relaxation values for InAs, $In_{0.84}Al_{0.16}As$ and $In_{0.81}Al_{0.19}As$ layers obtained from reciprocal space maps.

t (nm)	Degree of lattice relaxation (R%)		
	InAs	**$In_{0.84}Al_{0.16}As$**	**$In_{0.81}Al_{0.19}As$**
50	78.15	91.37	93.99
150	81.74	94.03	95.71
300	83.27	95.70	98.25

Mosaicity of all the layers, particularly InAs was also studied using the RSMs shown in figure 3.7. This mosaicity gives us a better understanding of the crystalline quality of the strained QW region, we measure the average mosaic tilt and variations in the local mosaic tilt in the heterostructures According to mosaicity model, the microstructure of epitaxial layer is assumed to be made up of mosaic blocks with finite coherence lengths in lateral and vertical directions, which exhibit small variations in orientation with respect to each other and to the sample frame. The angle of tilt with respect to the substrate normal (out-of-plane rotation $\Delta\omega$) and twist about substrate normal (in-pane rotation $\Delta\phi$) are another set of microstructural parameters that characterize these domains (Figure 3.9) [115,116].

The reciprocal lattice point broadening in the q_x-q_y plane (Δq_x) is caused by mosaic tilt (often referred as mosaic spread) and lateral coherence length (LCL) (often referred as lateral correlation length) [115,116]. Mosaic tilt of epilayer is a measure of dislocation density ($\propto$ $tilt^2$) in epitaxial studies [116–118], which can be can be obtained from their respective Δq_x value of a symmetric reflection (004), however, it is overlapped by contributions from finite LCL [115,116].

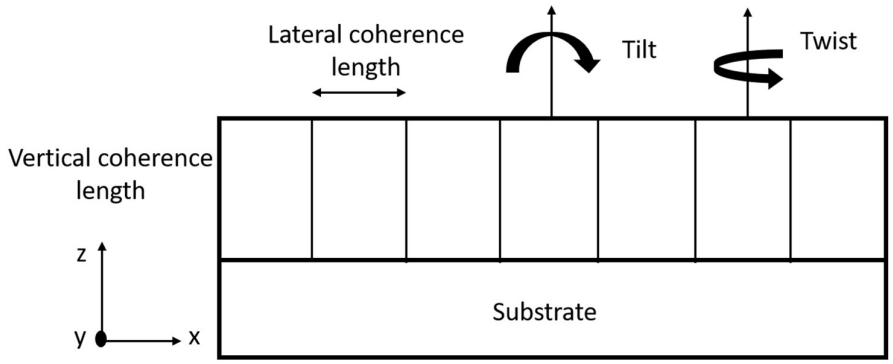

Figure 3.9: Illustrates the mosaic layer structure with the four characteristic parameters lateral and vertical coherence length, tilt, and twist.

In order to estimate mosaic tilt and LCL, Williamson-Hall plotting is required using ω-rocking curves of set of symmetric reflection ((00*l*); *l* = 2, 4, 6). [115,117] It is seen from Figure. 3.7 (a-c) that the Δq_x is decreased for InAs as well as InAlAs layers, with increase of buffer layer thickness, which reflects the decrease of mosaic tilt. Alternatively, mosaic tilt value was extracted from asymmetric (224) reflection RSMs, which can separate the LCL contribution. To support the weak features of InAs peaks and their broadening in figure 3.7, slow ω-rocking curves of (004) and (224) reflections (technically equivalent to horizontal line scans in Fig. 3.7) of InAs were also performed and shown in Fig. 3.10 (a) and (b), respectively, which depicts the similar observation on ω-broadening (Δq_x) and hence, the tilt. We have seen that the mosaic tilt value of InAs layers significantly decreased from t = 300 nm to t = 50 nm which indicates the monotonic reduction of dislocations in the epilayer, consequently, an improvement in the microstructure (crystalline quality) with increase of buffer layer thickness. The maximum tilt variation observed in strained sample 1.5° which is far less, only 0.03° in the GaAs substrate because such maps fall within only one or a few mosaic blocks [119]. The significant decrease in dislocations results in reduction of residual strain in the epilayer, consequently, accommodating/facilitating the lattice relaxation process. On the other hand, increase in LCL was observed with increase in buffer layer thickness, supporting the improvement of microstructural quality. Interestingly, similar observations are true for InAlAs layers (x: 0.81 & 0.84) also. As an overall effect, the increase of $In_{0.84}Al_{0.16}As$ buffer layer thickness leading to the improvement in its microstructural quality in terms of residual strain, relaxation (R%) and mosaicity (tilt and LCL), thus, governing the microstructural quality of successive InAs QW layer in the growth process.

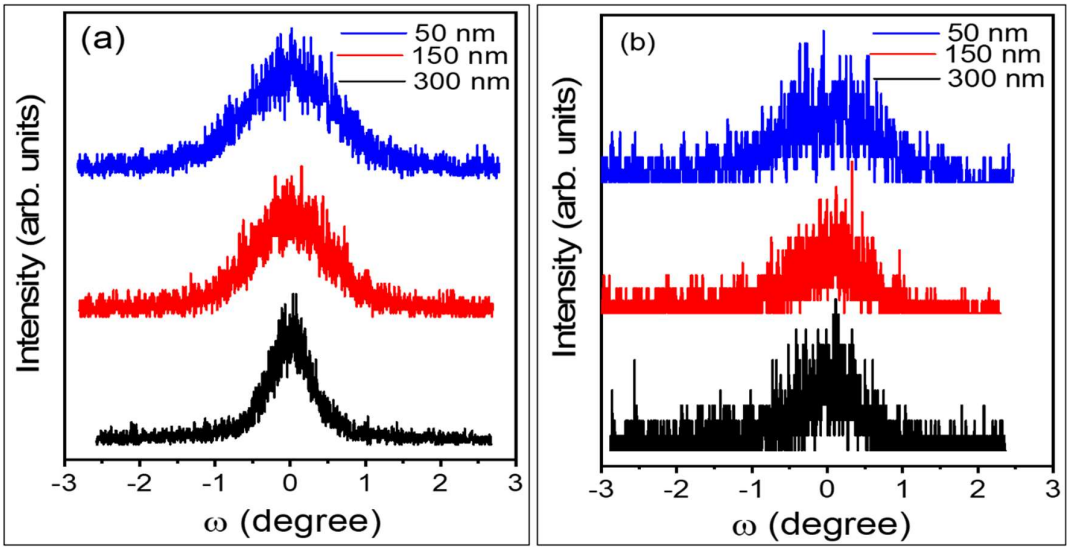

Figure 3.10: ω-rocking curves of InAs QWs layers on (a) (004) and (b) (224) reflections with different $In_{0.84}Al_{0.16}As$ buffer layer thickness, as indicated.

3.2.2 TEM

We performed TEM measurements for the two InAs/GaAs samples with different *'t,'* 50 nm, and 300 nm. Figure 3.11 shows the overview of these samples. Figure 3.11 (a, b) shows the low magnification image. These images show crisp interfaces between the buffer layer and the QW, implying minimal In and Ga intermixing. Also, we have calculated the thickness of the QW well region and its around 7 nm which is in agreement with its nominal value. Figure 3.11 (c, d) shows the bright field image at low magnification. This gives us the overview of buffer layers and QW. From these overviews it is evident that the strain is released through misfit dislocations in the lower part of the buffer layer, whereas the active layer is defect free.

In figure 3.12 (a, b) we show cross sectional HRTEM images of the QW regions taken along the (0 1 1) zone axis, showing that interfaces are coherent and epitaxial. These images are formed by interference of two or more Bragg reflections. And the interaction of incident electron beam with a specimen with a different material is different because of different scattering factors and this leads to a phase contrast of the crystal lattice for the different materials. The QW interfaces are indicated in all the images. Both samples exhibit flat and atomically sharp interfaces. The position of QW can be identified from HRTEM image

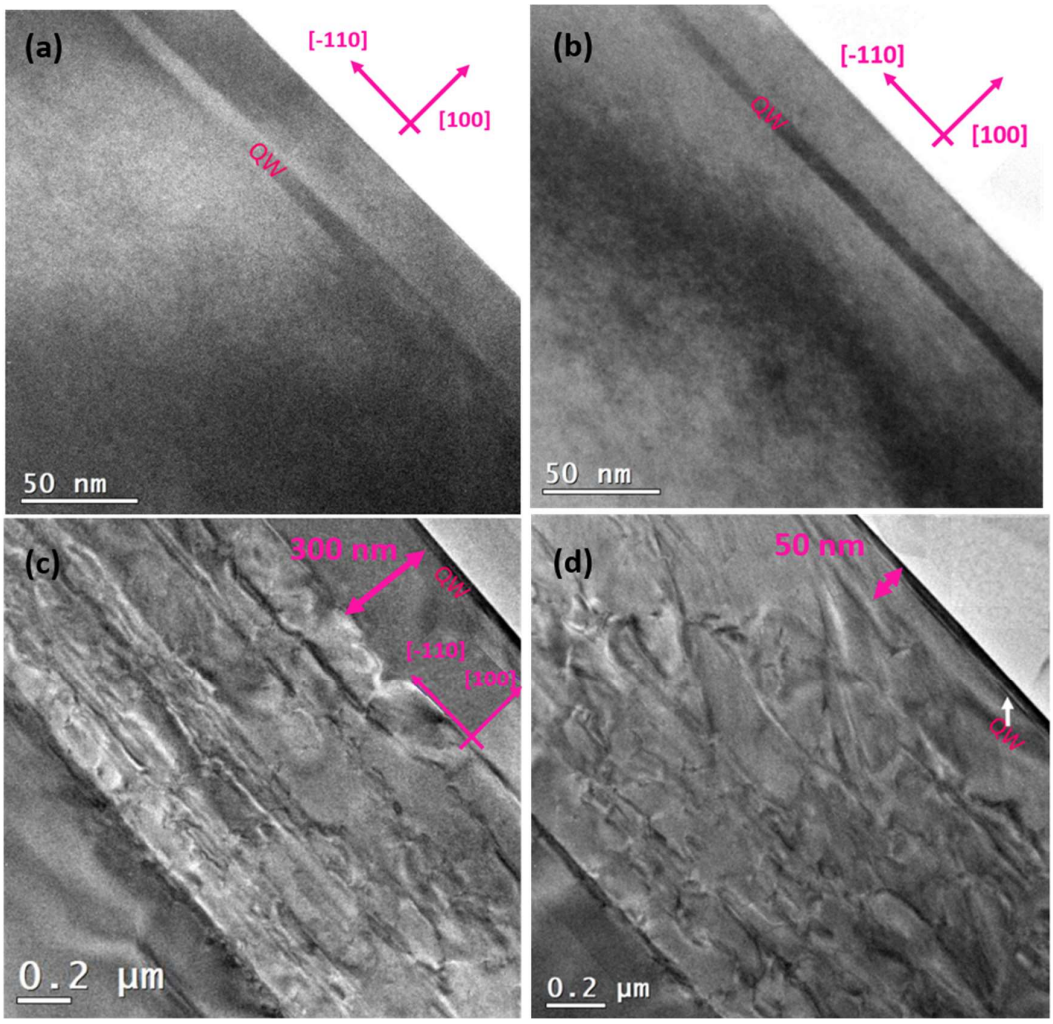

Figure 3.11: Overview of structure using low magnification image (a) t = 300 nm and (b) t = 50 nm. Shows the cross-section of the samples (c) t = 300 nm and (d) t = 50 nm measured with TEM with bright field image, it is evident that the strain is released through misfit dislocations in the lower part of the BL, while the upper part is defect free (within the limits of TEM statistics).

intensity variations. Also, from these HRTEM images, the strain variation within the QW is calculated with respect to the $In_{0.81}Al_{0.19}As$ layers using GPA developed by Hÿtch et al. [81] In the GPA method, any shift of the atomic lattice relative to some reference lattice in an HRTEM image is determined by mapping corresponding local shifts of Bragg diffraction peaks in the power spectrum of the recorded HRTEM image.

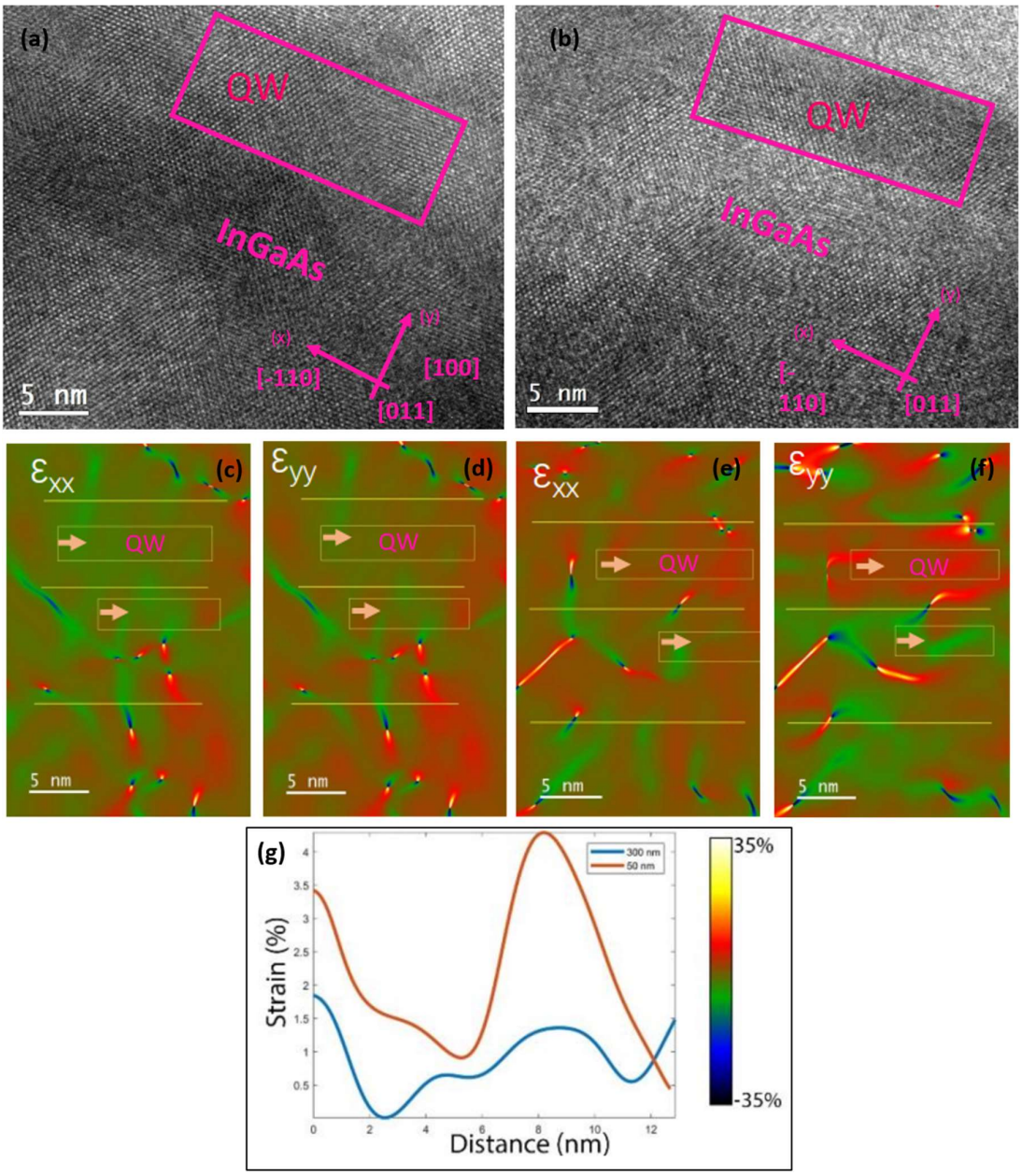

Figure 3.12: HRTEM images of (a) t = 300 nm, (b) t = 50 nm. The strain variation within the QW is calculated with respect to the $In_{0.81}Al_{0.19}As$ layers using GPA with (111) reflections. Out-of-plane lattice strain maps ε_{yy} of QW (top) and InGaAs (bottom) regions (c, d) for t = 300 and (e, f) for t = 50 nm. (green color indicates compressive strain and red color indicates tensile strain) (g) Strain profiles from the yellow boxes showing QW area along yellow arrows.

At first, in the power spectrum, two noncolinear Bragg spots are selected and masks are applied. Secondly, a complex image is extracted from the inverse Fourier transform of the masked Bragg spots. Then geometric phases of the two reciprocal lattice vectors are extracted from the complex image. Finally, this geometric phase is used to calculate the displacement field as the

geometric phase contains the local displacements of atomic planes. In the present work, strain variation was calculated with scripts in the FRWR tools menu (FRWR, 2012) with Gatan Digital Micrograph software. Two Bragg reflections were used to calculate the 2D symmetric strain map within the QW. A circular mask around the Bragg spots was applied to measure the strain maps with a spatial resolution of 5 nm. Out-of-plane lattice strain maps ε_{yy} ($\varepsilon_{\perp}$) and in plane lattice strain ε_{xx} ($\varepsilon_{||}$) of QW was calculated with respect to the InGaAs layer below the well for t = 300 nm and 50 nm are presented in Figure. 3.12 (c, d, e, f) respectively. It can be noted that the QW region for t = 50 nm has a higher average strain and exhibits some sharp variations, which for t = 300 nm are present in the barrier only, whose nature is still being investigated.

To quantify the strain value within QW (Figure 3.14 (g)), horizontal line scans has been taken from the region marked in the images. These line scans were averaged over 100 pixels along the growth direction of heterostructures and the calculated strain percentage in the QW region is quite higher in sample with t = 50 nm. The calculated mean out of plane strain values within QW for t = 300 nm and 50 nm are 0.9 ± 0.5 % and 2.2 ± 1.1 % respectively. The reduction of strain in the well with increasing t is in line with the XRD measurements, although the absolute values appear to be higher. Besides, the strain fluctuations around the average are more than double in the 50 nm sample, with respect to the 300 nm one.

3.3 Surface morphology:

AFM measurements were done in non-contact mode on all the samples with different t. AFM topographies have been recorded with image sizes of 20 × 20 µm. The acquired data have been flattened with a consistent protocol to remove long wavelength modulations that are artifacts due to AFM scanner nonlinearities. Figure 3.12 reports 20 × 20 μm^2 topographies of the samples and their RMS roughness in [-110] and [110] directions are indicated in table 3.5. The surface of all these samples shows a distinct cross-hatch pattern of roughness. The surface profiles should reasonably mimic the buried interfaces between the QW and barriers in the active layer, due to the reduced surface diffusion of adatoms at our growth temperatures and the fast sample cooldown at the end of the growth. The rectangular geometry of the pattern reflects the orientation of the GaAs substrate, where the quasi-periodic modulations occur along the [110] and [-110] directions in the [001] surface. Despite the effort to accommodate the lattice mismatch strain in the buffer layer, the presence of the cross-hatch pattern is an unavoidable feature typical of metamorphic growth, which prevents the attainment of truly

long-range monolayer-flat 2D layers [120]. These crosshatched morphology on the surface of strained InGaAs epilayer grown on GaAs substrate occurs when the threading dislocation density in the epilayer is low. The morphology of the crosshatched patterns could not be observed when the lattice mismatch of the strained epitaxy was smaller than 2% [120], The formation of cross hatch pattern depends on many factors such as growth temperature, misfit strain and the thickness of the epitaxial layer. Typically, a cross-hatch pattern is only observed for moderate crystal lattice mismatch for a single layer and this range can be extended if grading or metamorphic approach is applied [121]. Cross-hatch patterns of this kind have been found on $Si_{1-x}Ge_x/Si$ [122], $In_xGa_{1-x}As/GaAs$ [123,124], and $In_xGa_{1-x}As$ /InP [125,126]. Despite several attempts to explain how this roughness forms, there is no general agreement on the exact dynamics. One explanation could be related to locally enhanced or suppressed growth rate due to the nonconstant strain field generated by dislocation bunching [123,127].

As shown in figure 3.13, we can clearly see the qualitative differences in the images as we increase the buffer layer thickness. With the increase in buffer layer thickness, we can see more regular cross hatch pattern which is due to the reduction of strain in the underlying layers. The total RMS roughness increases as t decreases. t = 50 nm is 4.4 nm while on sample with t = 300 nm is 3.2 nm. Also, there are no evidence of surface defects on all these samples (as these defects are mainly associated with deep tranches on the surface), which could be seen on the surface of dislocated InAs QWs [46]) The 1D RMS roughness of all the samples in both [-110] and [110] directions (calculated by averaging values of different line scans in each direction) versus the buffer layer thickness are shown below in the table 3.5. With the line scans, we can see the periodicity of sample with t = 300 nm in [-110] direction is around ~ 1.15 μm and in [110] direction its ~330 nm whereas with t = 50 nm, where the periodicity in [110] direction is 400 nm and is almost half as compared to [-110] direction (~ 800 nm). This anisotropy has a vast impact on the scattering mechanism which will be discussed in detail in next chapter.

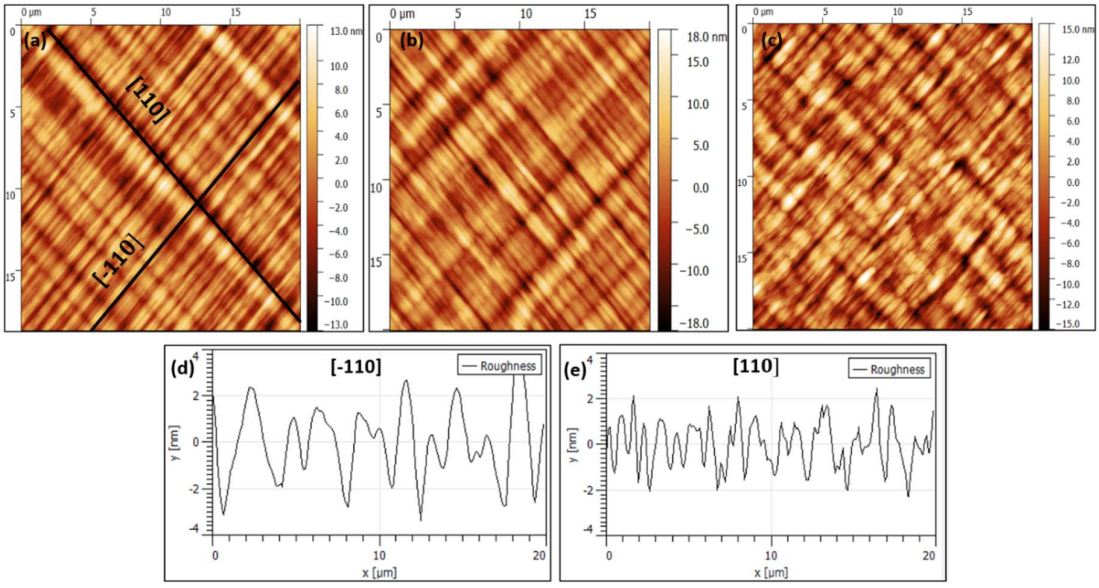

Figure. 3.13: Shows the representative AFM topography of the InAs/GaAs samples grown during this work, showing the characteristic cross-hatch pattern of surface roughness. The crystallographic directions that form the perpendicular network of corrugations are indicated in the image. The image size is 20x20 μm^2, while the vertical scale is 25 nm. (a) t = 300 nm (b) t= 150 nm (c) t = 50 nm. (d, e) shows model line scans of RMS in the two orthogonal directions of t = 300 nm.

Table 3.3: Shows the RMS roughness value of samples with t = 50, 150 and 300 nm in both (-110) and (110) directions.

		300 nm	**150 nm**	**50 nm**
RMS Roughness	[-110]	1.2 nm	1.4 nm	1.5 nm
	[110]	1.4 nm	2.5 nm	2.8 nm
Periodicity	[-110]	1.15 µm	950 nm	800 nm
	[110]	330 nm	360 nm	400 nm

3.4 Conclusion

The main goal of this chapter was to optimize samples for ensuring minimum strain and to work on the gradually slowing progress in the field of 2DEG's mobility. However, this is not the end of the line. Improvement in sample quality have and surely will open the road to new and exciting physics. In this chapter, we have shown that proper design of the strain-relieving BL strongly influences residual strain of metamorphic InAs/ GaAs QWs. Terminating the BL with an $In_{0.84}Al_{0.16}As$ step with at least 300 nm thickness minimizes the strain in the QW

region. The XRD, TEM and AFM analyses, indicate that how we have tuned the strain in the QW region and in next chapter we will do the transport measurements and study the role of strain as a scattering mechanism limiting electron mobility in metamorphic InAs QWs. Understanding these scattering mechanisms which affect the electron transport in our material system would be crucial in order to try to approach the limit set in GaAs/AlGaAs 2DEGs. How this task is to be mastered in a practicable way is only one of the challenges the future and the experimenters hold for the MBE community. In the next chapter we will analyze in deeper detail the scattering mechanisms of our InAs 2DEGs, with the goal of exploring the possibilities for future improvement

Chapter 4

Scattering mechanisms in InAs quantum wells

High electron mobility in these heterostructures is sought not just to develop a more efficient material platform for Andreev qubit quantum technologies, but also to explore fundamental elements of condensed matter physics. Therefore, to increase the electron mobility we need to work towards a "more ideal" system of free-like electrons to investigate their fundamental properties. In particular, for reaching high electron mobility we need to understand the mechanisms that are limiting it.

For 2DEGs in lattice-matched GaAs/AlGaAs heterostructures, studies on the mobility limiting mechanisms, and successive refinements in the growth process, have given outstanding results in previous years in the field of semiconductor physics and device technology [128]. One of the notable aspects of the novelty of AlGaAs/GaAs heterostructures is its ability to control electronic band structures with a high degree of freedom due to the perfect lattice matching. By varying the Aluminum and Gallium composition in the AlGaAs layer, it's possible to create heterojunctions with specific band offsets. This control is essential for the design of high-electron mobility devices. There clearly exists a strong interest in further improvement of GaAs/AlGaAs heterostructures [86,129]. It is therefore important to understand dominant sources of scattering and elucidate the ways to minimize them.

The scattering caused by ionized impurities has been identified as the main limiting factor of low temperature mobility in these systems; this has led to the growth of GaAs/AlGaAs heterostructures in extremely clean MBE systems to avoid the presence of unwanted impurities, and to confine the donors required to supply charge to the 2DEG far away from the 2DEG itself through modulation (remote) doping. This allowed to reach electron mobilities up to 56×10^6 cm^2/Vs [130]. For InAs/InGaAs the situation in far more complex, as we have seen in the previous chapter. Metamorphic growth due to lattice mismatch introduces unavoidable effects such as residual strain, roughness, and composition modulation, point defects and possibly

residual dislocations [46,131,132]. In the previous chapter we have seen that an optimization of the growth protocol leads to substantial improvements of the morphological properties of these systems. With such modifications in the growth protocols, we will show at the beginning of this chapter that we have achieved high mobility samples better than the state of art on the InP substrates, up to the 10^6 m^2/Vs range, depending on the InAlAs buffer layer thickness. Starting from these technological achievements, the main goal of this chapter will be to identify the main scattering mechanisms and to relate them to the growth protocols, with the aim to reduce them.

In particular, we will discuss the low temperature transport measurements and then will go over a theoretical model that covers the key low temperature scattering mechanisms in semiconductor heterostructures. This hypothesis will be applied to our samples allowing us to determine the major sources of scattering, mostly from low temperature transport observations. The insights gained from this research enabled us to enhance the buffer layer to achieve higher electron mobilities.

4.1 Transport measurements:

In the previous chapter we have studied the growth and structural characteristics of the samples with different buffer layer thickness 't' and we saw that as we increase 't,' the strain in the QW region is decreasing. We assessed the low temperature transport properties of the 2DEG formed in the same InAs QWs using the Van der Pauw method at 4.2 K. Figure. 4.1 shows that μ increases from 6×10^4 cm^2 /Vs for t = 50 nm up to 7.1×10^5 cm^2 / Vs for t = 300 nm, i.e., more than an order of magnitude, whereas, n lies in the $3–3.5 \times 10^{11}$ cm^{-2} range, and is independent of 't'. Thus, the mobility of these samples increases dramatically as the out of plane strain decreases, while carrier density is similar for all the samples. As we have seen in the previous chapter, for 't' above 200 nm, the 0.84 region becomes virtually strain-free, while in the 0.81 region the strain switches from compressive to tensile [47]. Mobility data combined with the previous XRD and TEM analyses, indicate that strain plays a major role as a scattering mechanism limiting electron mobility in metamorphic InAs QWs, and that a careful design of the strain-relieving $In_xAl_{1-x}As$ BL can increase electron mobility by more than one order of magnitude. In this chapter we will further investigate these samples to show the mobility dependence on electron density in gated Hall bars to elucidate the scattering mechanisms.

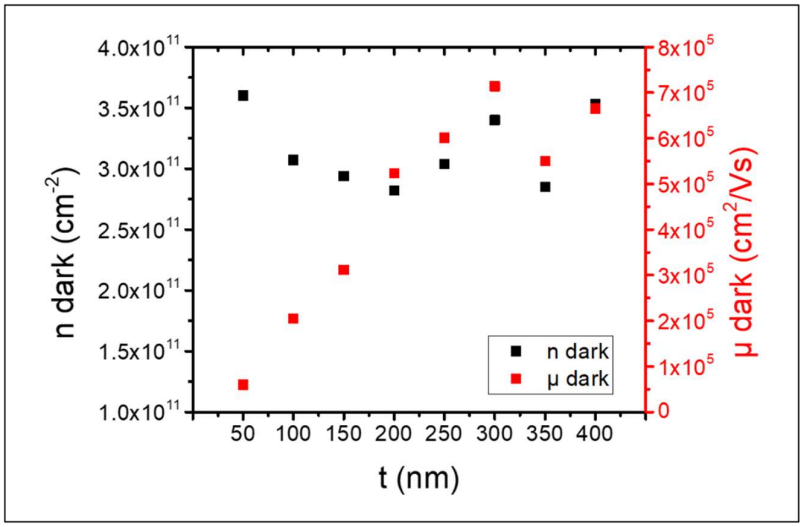

Figure 4.1: Low-temperature (T = 4.2 K) electron charge density and mobility in the InAs/GaAs 2DEG as a function of t.

4.2 Low temperature scattering mechanisms

Low temperature scattering mechanisms in two-dimensional electron systems have been discussed in a review by T. Ando and coworkers [133]. Based on this theoretical framework, the HMMBE group at CNR has successively modeled the low temperature scattering mechanisms in $In_{0.75}GaAs/In_{0.75}AlAs$ QWs which provided the bases for our further optimization and studies [93,95].

According to Gold, at low temperatures, there are three main sources of scattering in a 2DEG system with a single sub-band:

1. Ionized impurity scattering (II), due to Coulomb interaction between the conduction electrons and an ionized impurity background uniformly distributed in the material.
2. Interface roughness scattering (IR), due to the non-planarity of the interfaces defining the quantum well, which act as fluctuations in the width of the quantum well which confines the electrons.
3. Alloy disorder scattering (AD), due to the random distribution of the indium and gallium atoms inside the crystal matrix. This scattering potential is assumed to arise from the difference in electron affinity, band gap, and electronegativities of the two constituent binaries, InAs and GaAs in our case.

These three scattering sources are modeled, within the relaxation time approximation, assuming that the scattering processes are elastic and that the scattering centers are randomly distributed. Additionally, the quantum well is modeled as square well with infinite barriers, and the resulting ground state 1-D wavefunction is a half-period sine wave.

The relaxation time τ_α for a single source of scattering can be computed as

$$\frac{1}{\tau_\alpha} \cong \frac{1}{2\pi\varepsilon_f} \int_0^{2k_f} \frac{q^2}{\sqrt{4k_f^2 - q^2}} \frac{< |U(q)|^2 > \alpha}{\epsilon^2(q)} \, dq \tag{4.1}$$

where k_f and ε_f are the Fermi wavevector and the Fermi energy of the electrons in the 2DEG, respectively, and $\epsilon(q)$ is the dielectric function of the electron gas, whose analytical expression can be found in reference [134]. $<|U(q)|^2>_\alpha$ is the random scattering potential peculiar to each scattering mechanism, with α being 'II' for the ionized impurity scattering, 'IR' for the interface scattering, and 'AD' in the case of alloy disorder. The random scattering potential caused by ionized impurities, in the case of a homogeneous distribution of the impurities in the material, has the form

$$< |U(q)|^2 >_{II} = N_B L \left(\frac{2\pi e^2}{\epsilon_L q}\right)^2 F_B(q) \tag{4.2}$$

Here N_B is the ionized impurity density, L is the width of the QW, e is the electron charge, ϵ_L is the dielectric constant of the barriers, and $F_B(q)$ is a form factor considering the finite extension of the electron gas in the z direction, whose analytical form depends only on the geometry of the quantum well [135]. The random potential due to the alloy scattering is described as

$$< |U(q)|^2 >_{AD} = x(1-x)\frac{a^3}{4} (\delta V)^2 \frac{3}{2}\frac{1}{L} \tag{4.3}$$

a is the lattice parameter of the alloy and δV is the spatial average of the fluctuation of the alloy potential over the alloy unit cell. At last, the interface roughness between the barriers and the well is characterized by its amplitude Δ in the z direction and its coherence length Λ in the xy plane. Its random scattering potential is [136]

$$< |U(q)|^2 >_{IR} = 2\frac{\pi^5}{m_z^2}\left(\frac{\Delta^2\Lambda^2}{L^6}\right)^2 e^{\frac{q^2\Lambda^2}{4}} \tag{4.4}$$

where m_z is the electrons effective mass in the z direction.

Usually, the quality of a 2DEG structure and with that the positive or negative outcome of a growth experiment is determined by the already mentioned magneto-transport characterization, yielding electron density n and mobility μ. The electron mobility is governed by the interaction of electrons with various scattering sources, which define the average scattering time τ according to

$$\mu = \frac{e.\tau}{m*} \tag{4.5}$$

τ is the average time of flight for an electron between two scattering events. This total scattering time is composed of the individual values of the different scattering types, according to the Matthiesen's rule:

$$\frac{1}{\tau} = \sum\frac{1}{\tau_i} = \frac{1}{\tau_{II}} + \frac{1}{\tau_{AD}} + \frac{1}{\tau_{IR}} \tag{4.6}$$

where τ_i denotes the individual scattering times. It is important to understand that a given scattering mechanism does not lower or raise the mobility of a 2DEG, but it rather sets the maximum mobility value that is possible:

$$\frac{1}{\mu_{res}} = \sum\frac{1}{\mu_i} = \frac{1}{\mu_{II}} + \frac{1}{\mu_{AD}} + \frac{1}{\mu_{IR}} \tag{4.7}$$

μ_{res} is the resulting total electron mobility and μ_i denotes the limit set by each individual scattering process.

Figure 4.2 illustrates an example for an $In_{0.75}Ga_{0.25}As/In_{0.75}Al_{0.25}As$ QW 2DEG taken from reference [93] showing the individual mobility limits set by these scattering processes and how they sum up to a final mobility that can be fitted to the experimental values obtained by a magneto-transport measurement. This figure nicely illustrates that eliminating one scattering process completely just removes this specific mechanism's influence, which does not necessarily increase the mobility [137]. So, for example, a growth parameter adaptation aiming at reduction of background impurity scattering may very well be successful, but still go

completely unnoticed if the sample's mobility is governed by e.g. interface roughness scattering. For example, for the samples of ref. [93], the interface roughness is not playing an important role because with the measured roughness parameters, the mobility due to IR scattering is in fact at least four orders of magnitude larger than the observed one. In these systems the fermi length is much smaller than the coherence length, yielding negligible impact on the mobility.

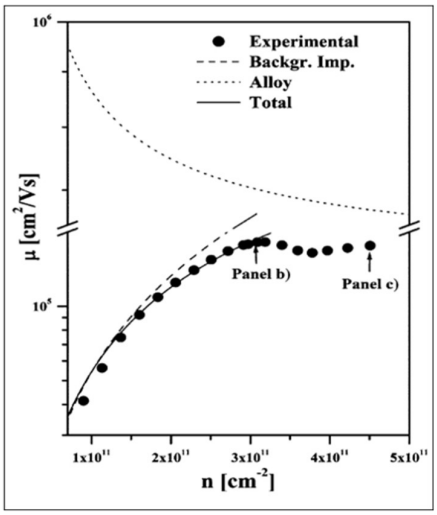

Figure. 4.2: Shows the low-temperature electron mobility measured in an $In_{0.75}Ga_{0.25}As/In_{0.75}Al_{0.25}As$ QW 2DEG, as a function of the carrier concentration. Solid line: fit of the sample experimental data considering scattering with BI (long-dashed line) and AD (short-dashed line) [93].

4.3 Trasport measurements on gated Hall bars

The key point of this discussion is to notice that the value of the mobility can be computed from known material properties (m^*, L, $\epsilon(q)$, ϵ_L, k_f, ε_f, F(q), x, and a), and few scattering-type specific parameters: N_B for the ionized impurity scattering, δV for alloy disorder scattering, and Δ and Λ for interface roughness scattering. This allows, in principle, to estimate the scattering parameters knowing the measured mobility of the sample. Of course, with a single mobility value little conclusion can be drawn on four parameters. However, a deeper insight can be acquired if any of the material properties can be varied in a controlled way. The easiest property to vary within the same sample is the carrier density, n, which in turn determines both the Fermi wavevector, K_f, and the Fermi energy, ε_f, according to the semiclassical relations for a two-dimensional system [138].

$$K_f = \sqrt{2\pi n} \tag{4.8}$$

$$\varepsilon_f = \frac{\hbar^2 K_f^2}{2m^*} \tag{4.9}$$

In a quantum well system, there are two basic approaches to modify the carrier density of a 2DEG. The "persistent photoconductivity" phenomenon is one example. This entails slowly freezing the sample from ambient temperature to cryogenic temperature to freeze the charge state of the donor impurities. When the sample is illuminated with brief pulses of light, some of the donors ionize, providing extra charge to the 2DEG. The consequence is a rise in carrier density for each light pulse, which has been utilized to modify the carrier density in an InGaAs/InAlAs system, for example, by Ramvall and co-workers. [139,140] The second method for modifying the 2DEG charge is to apply a voltage to a metal gate deposited on the sample surface. The main advantage of the persistent photoconductivity approach is that it does not require any additional sample processing; the disadvantages are that (i) the minimum charge density attainable is limited by the charge density in the dark, and (ii) photoionizing the donors changes the background ionized impurity density of the sample, thereby changing their contribution to scattering. To apply a voltage to a surface metal gate, on the other hand, the gate must be manufactured. Furthermore, the gate voltage can significantly affect the band profile, changing the extent of the charge dispersion of the 2DEG.

In this work we have chosen to fabricate gated hall bars on the three structures discussed in chapter 3 (t = 50, 150 and 300 nm). These gated Hall bars were patterned using EBL with an aspect ratio of 1:2 with the process explained in *appendix 1.* The measurements were performed in a liquid-helium cryostat that can be pumped to a base temperature of about 4.1 K. Magnetic fields of up to 12 T were generated by a superconducting solenoid. The signals were measured with lock-in amplifiers applying a modulated bias current of around 1 mA. We have varied the gate voltage in these structures while sweeping the magnetic field at each bias value. Gating is preferred over illumination for two main reasons: first, because our self-consistent Schrödinger-Poisson simulations for the conduction band and electrons wavefunction show that – by varying the gate voltage – the wavefunction is not substantially altered (see Fig. 4.3 (a)). Second, because it guarantees a higher reproducibility of the results: the charge density can be increased and decreased at will, thus it is possible to repeat the electron mobility measurements in the same cooldown. Figure 4.3 (b) shows how with PS simulations, by altering the gate voltage we can change the carrier concentration in the 2DEGs.

In this PS simulations we have set the donor density in the barrier to 2 X $10^{16}cm^{-3}$, in order to obtain a total carrier density of 3.6 × 10^{11} cm^{-2} in the QW at zero bias. The simulation has been repeated, without changing the donor density, for different biases applied to a top gate. This bends the bands and alters the total carrier density n. This figure shows the resulting band structure and carrier distribution with the top gate tuned to voltages from -0.1 to 0.1 V to obtain, which allowed to tune n from 3.1 × 10^{11} cm^{-2} (blue trace) to 4.5× 10^{11} cm^{-2} (green trace). Also, we saw that once the charge goes over 4.5 × 10^{11} cm^{-2} electrons start to populate the surface $In_{0.81}GaAs$ cap (in the model we neglect effects of surface oxidation), thus forming a parasitic 2DEG that screens the bias potential and preventing to reach higher n in the InAs QW.

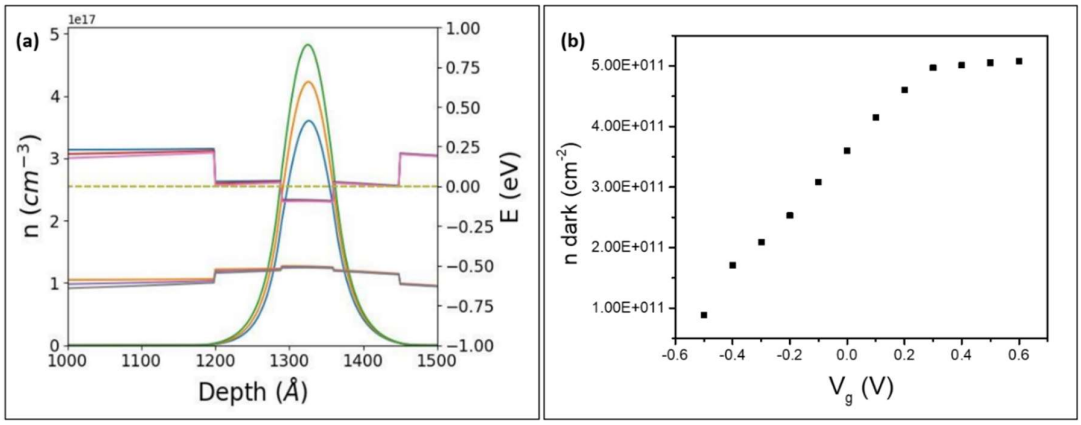

Figure 4.3: (a) Schrödinger-Poisson self-consistent calculation of the conduction band, valence band and the normalized ground state wavefunction of a with a variable surface gate voltage of 0, 0.1 and -0.1 V. (b) Gate voltage vs charge density obtained with the simulation. [110,111]

We have simultaneously determined the conductivities and recorded Shubnikov–de Haas (SdH) oscillations in [110] and [-110] directions and, and used the total electron densities for the calculation of the mobilities. We have confirmed that the total electron densities determined from SdH oscillations equal the ones determined from Hall measurements as mentioned in reference. [141] This allows to check the stability of the sample and the consistency of the results. Figure. 4.4 (b) shows the transverse and longitudinal resistances at 4.2K as a function of the perpendicular magnetic field up to 10T for a 2DEG placed at 300 nm buffer layer sample with electron mobility of 7.2x10^5 V/s. The longitudinal resistance shows the break of spin degeneracy at about 3.5 T, and its vanishing at magnetic fields that correspond to even integer quantum filling factors υ>4 demonstrates the formation of a 2DEG, without any additional

parallel conducting channels in the structure. The carrier density calculated with the SdH oscillations agreed with the classical Hall measurements in both samples, in both orientations.

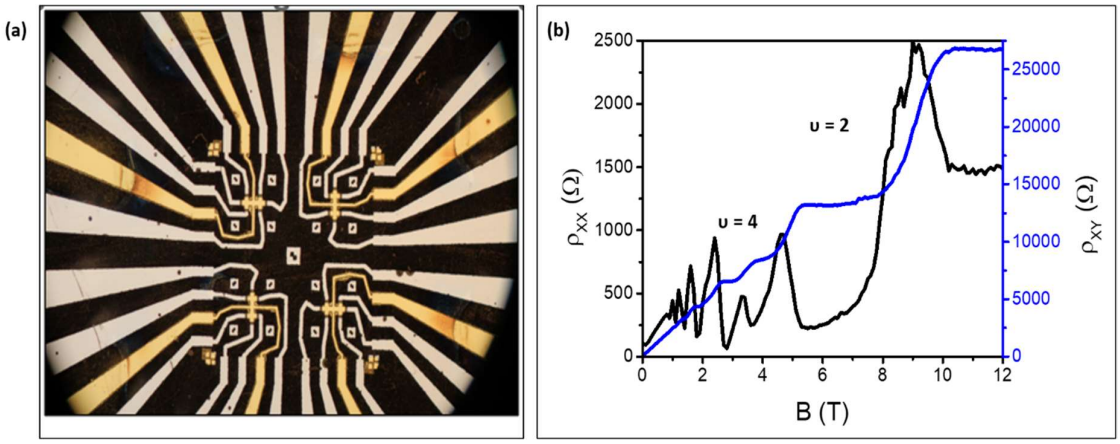

Figure 4.4: (a) Optical microscope image of the hall bars oriented in [110] and [-110] directions. (b) Longitudinal and transverse resistances of a 300 nm buffer layer sample in (110) direction measured at T=4.2 K with a gate volage of 0.25V as a function of the perpendicular magnetic field B up to 12 T.

4.4 Mobility versus carrier density measurements

Figure 4.5 shows the measured carrier density dependence on top gate voltage. The carrier density varies almost same in both orientations and we see that the range in which n is linear is -0.3 V to 1 V for 300 nm buffer sample and -0.6 to 0.6 in 50 nm buffer sample. If the gate voltage is swept outside this range, the density deviates from linearity. In particular, if the

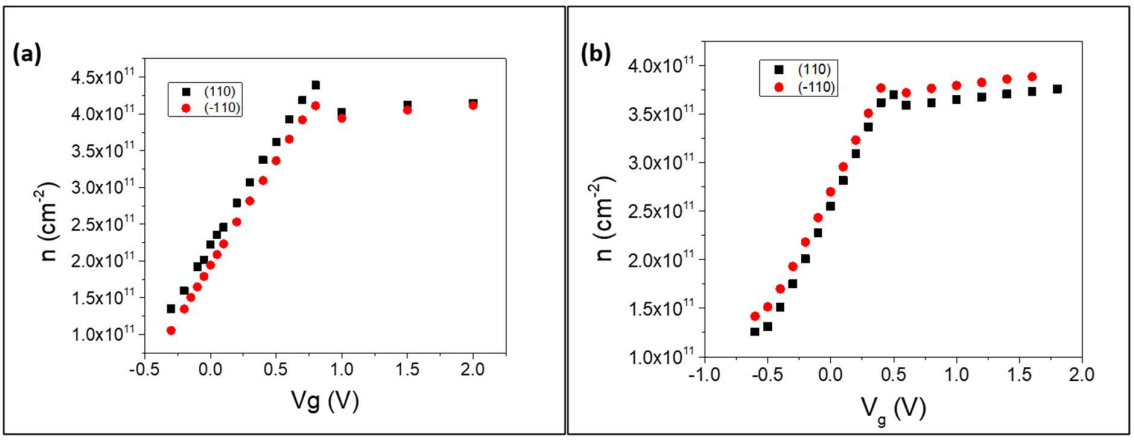

Figure 4.5: Measured carrier density dependence on top gate voltage on (a) 300 nm (b) 50nm buffer layer sample for hall bars oriented in (-110) and (110) directions.

voltage is swept to values greater than the given range, and then brought back to zero, the measured carrier density for zero applied gate voltage is increased and the mobility reduced. We attribute this behavior to charges trapped on the surface of InGaAs. These changes are not easily controllable, so care has been taken not to exceed this positive limit value, cross-checking the consistency of carrier density and electron mobility at zero applied voltage after each voltage sweep. The PS simulations shown above (Figure.4.3(b)) confirm that when the bias corresponds to n a little above 4.5 x 10^{11} cm^{-2} surface charging screens the potential seen by the 2DEG Electron mobilities were recorded with respect to charge density for all the three structures in the gate voltage range which results linear for each sample.

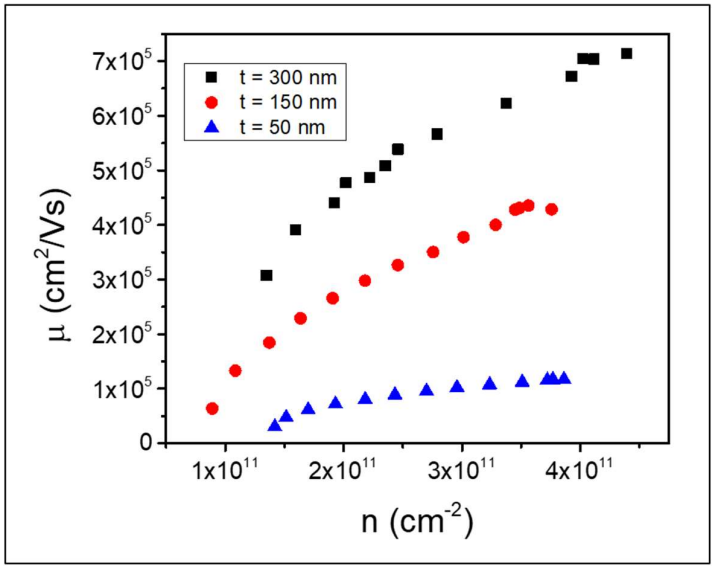

Figure 4.6: Low temperature hall mobility at 4.2K for the samples with different $Al_{0.84}Ga_{0.16}As$ buffer layer thickness with hall bars fabricated in [-110] direction.

Figure. 4.6 shows the mobility vs carrier density curves for the samples with different buffer layers on Hall bars in the [-110] direction. It can be seen that as we increase the buffer layer thickness the mobility increases considerably, in-line with the Van der Pauw measurements. In the next paragraph we are going to model these structures and try to figure out the underlying reasons for this increase in mobility.

4.4.1 Mobility Anisotropy

Figure 4.7 shows the measured dependencies of the mobilities on charge densities at 4.2 K in [110] and [-110] directions for samples with highest and the lowest mobility (t = 300 and 50 nm, respectively). Increasing the gate voltage results in an increase of mobilities in both

directions for both the samples, and for both the samples a higher mobility was observed when the Hall bars were oriented in the [-110] direction.

A similar anisotropy has been observed in molecular beam epitaxy grown $Ga_{0.25}In_{0.75}As/InP$ samples [139] and $In_{0.75}Ga_{0.25}As$ 2DEGs on GaAs substrate. [94] On our samples for t = 300 nm such anisotropy is about ~15% while for t = 50 nm it increases to about ~40% anisotropy, for the same charge density ($n = 3.5 \times 10^{11} cm^{-2}$). This suggests that IR should not play a major role as a scattering mechanism in our 2DEGs with higher buffer layer with lower anisotropy [93,106].

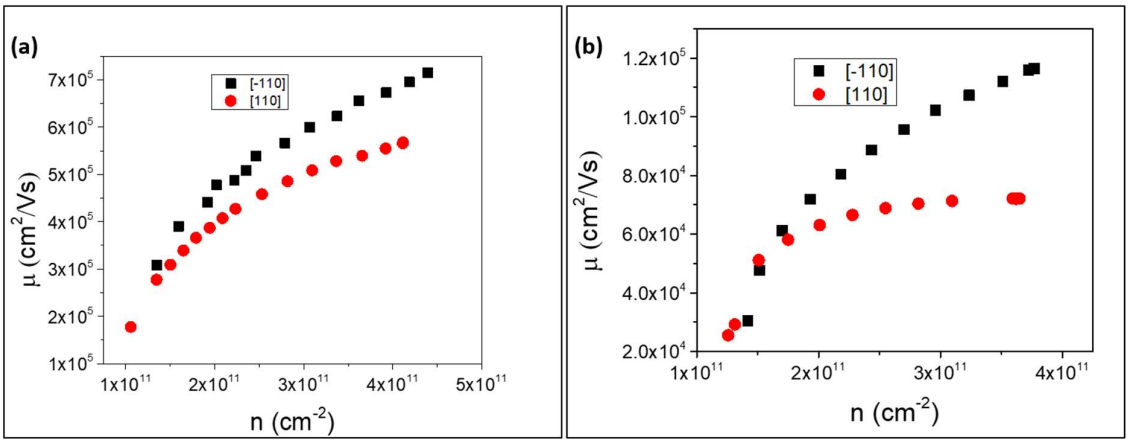

Figure 4.7: Mobility vs carrier density curves for Hall bars fabricated in both [-110] and [110] direction. (a) 300 nm thick buffer layer, (b) 50 nm thick buffer layer.

4.4.2 Power Law

Above we have discussed that there are three scattering mechanisms that may have a notable impact on modern 2DEG structures: II-, AD- and IR-scattering. While the detailed dependence of μ vs n for each of them has been accurately modeled as described above, a rough estimate of the main limiting mechanisms can be done by an allometric dependency on electron density in the form of:

$$\mu \sim n^{\alpha} \tag{4.11}$$

The exact values of the exponent α for each scattering mechanism still waits to be found, despite numerous theoretical and experimental studies.

- Background Impurities (BI): $0.6 < \alpha < 1$; the value is strongly depending on electron density, with $\alpha = 0.7$ for densities around $2 \cdot 10^{11}$ cm^{-2} ([142] [143]), but approaching $\alpha = 1$ for higher densities.
- Remote Impurities (RI): $\alpha \approx 1.5$.
- IR: $\alpha < 0$ was predicted by Nakamura [144] and experimentally confirmed by Reuter [145] and Pan [146] for high densities.

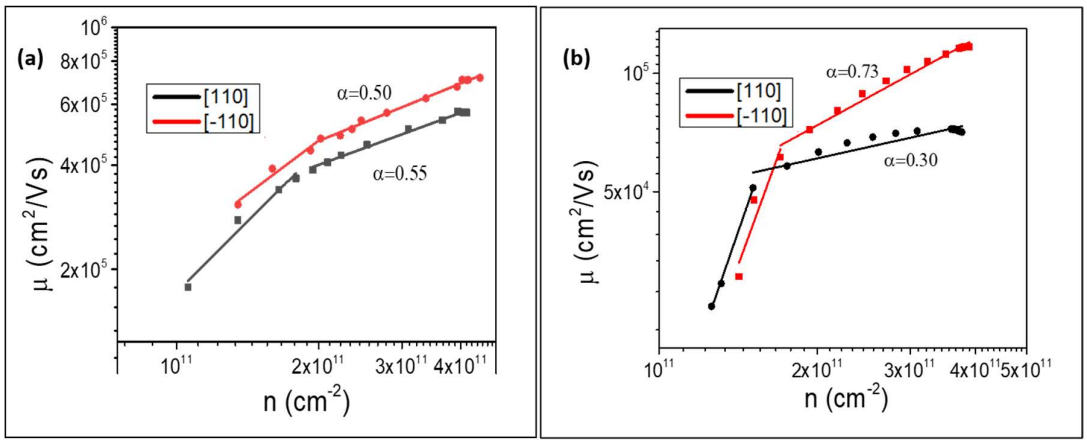

Figure 4.8: Log-log plot of mobility vs carrier density (a) t = 300 nm, (b) t = 50 nm, with allometric dependency fitting.

To determine what limits mobility in our structures we are using a log-log plot of μ vs n as shown in Figure. 4.8. The values for α we obtained from our high-mobility sample in both directions are approaching ½ suggesting that the II scattering is due to the unintentional background impurities, which is consistent with the fact that no remote modulation-doping is introduced in these samples. The extracted fit, solid lines, for α=1/2 fits well over the density range of interest and is roughly equivalent for all samples measured in this study. The sample with t = 50 nm shows a less clear behavior, with α changing from about 0.3 to 0.7 in the two orientations, hinting a more complex combination of scattering mechanisms.

4.5 Modelling of μ vs n data:

The total mobility vs carrier density is modeled using Stern Howard formulation in the region where the carrier density depends linearly on the gate voltage in figure 4.5. In the first part of this section all the three scattering mechanisms parameters are discussed individually (Figure. 4.9 and 4.10). This analysis will give us better insight into the individual scattering mechanisms

and how they are affecting the total mobility of the structures, depending on the parameters used.

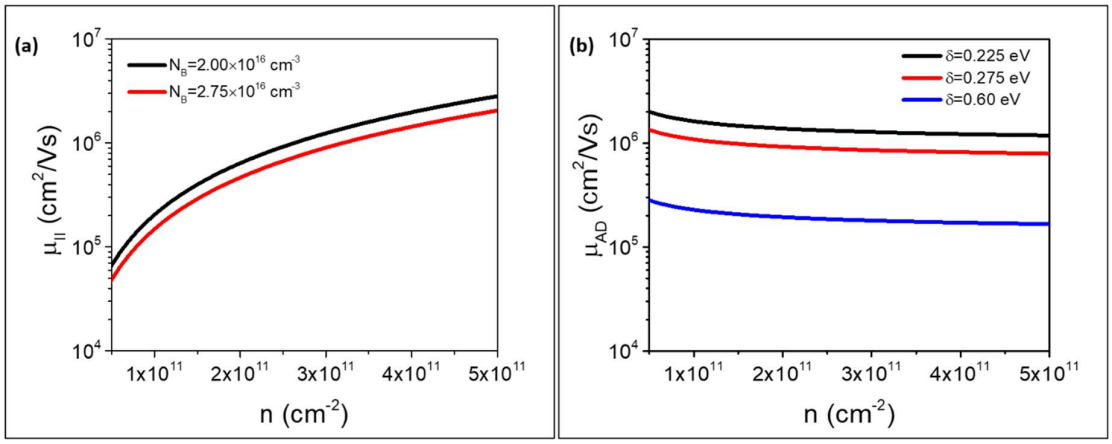

Figure 4.9: Mobility versus carrier density curves as given by Equation.4.2 and 4.3 for a 7 nm thick InAs QW with a 9 nm thick $In_{0.75}Ga_{0.25}As$ layer on both sides. (a) Ionized impurity scattering for two values of impurity density, N_B. b) Alloy disorder scattering for three values of the alloy potential fluctuation δV.

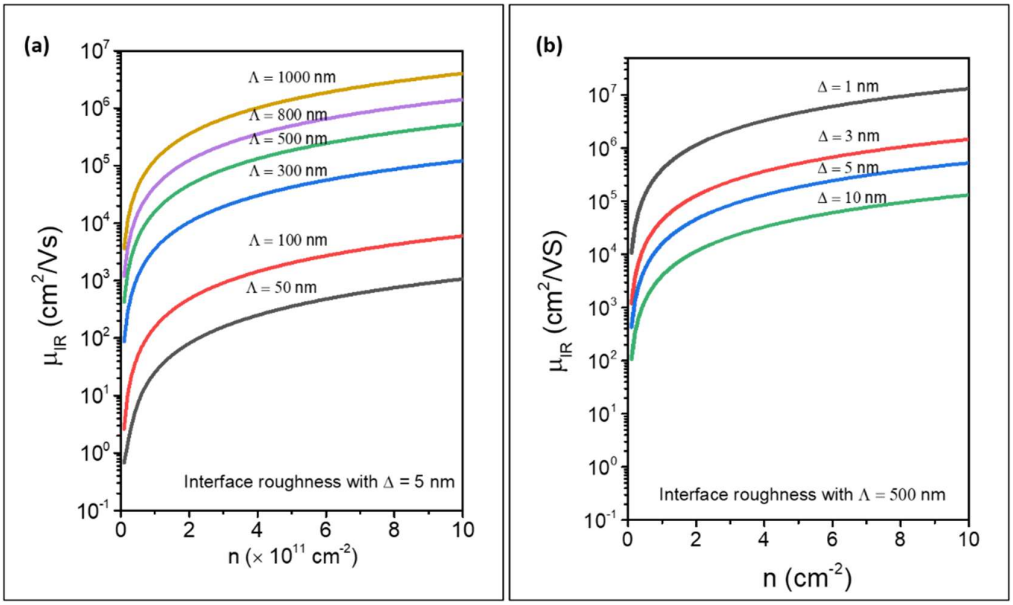

Figure 4.10: Mobility versus carrier density curves as given by Equation. 4.4, for a 7 nm thick $In_{0.75}Ga_{0.25}As$ QW by fixing IR scattering: the parameter, (a) curves with fixed Δ = 5 nm and b) curves with fixed Λ= 500 nm.

Afterwards, the three scattering mechanisms are combined through Matthiessen's rule (Equation. (4.7)) and fitted to reproduce the experimental mobility data in both [110] and [-

110] directions for the samples with t = 300 nm and t =50 nm (Figure. 4.11). Ionized impurity scattering can be divided into remote impurity scattering from ionized Si donors (which is absent in our samples), and background impurity scattering from impurities in the quantum well or in the undoped spacer layer. We have supposed that N_B is isotropic and only depends on the growth conditions and structure, and does not change in two directions. In fig. 4.9 (a) we show the plot for background impurity concentrations of $2x10^{16}$ cm^{-3} and $2.75x10^{16}$ cm^{-3}. Note that these values of the ionized impurity density parameter N_B are in line with the previous work done on similar 2DEGs, where the ranged around a few ~ 10^{16} cm^{-3} [137]. Besides, the mobility values they yield are in line with the mobility data for t = 300nm and 50 nm, respectively, thus are reasonable guesses to fit our experimental data.

The slight decrease of N_B with increased t could be due to the improved structural quality of our layers as the residual strain is relieved. In fact, the presence of electrically active deep levels inside the band gap was observed on similar samples [107], which were ascribed to the formation of arsenic defects (e.g., substitutional or clusters), and could be more pronounced in samples with lower crystal ordering.

The alloy disorder scattering is important in our samples since 69 % of the electron wave function of the InAs binary QW spreads into ternary InGaAs barriers [47]. The parameter that characterizes it is the alloy potential fluctuation δV. The only theoretical predictions for its value are 0.53 eV, based on the difference in electronegativities of the alloying species, and 0.83 eV, based on the difference in electron affinity [147]. However, none of these values are based on first-principles calculations of atomic potentials in the alloy, and are to be regarded as rough qualitative estimates. Previously experimentally determined values for δV for similar structures in different samples are 0.6 eV for "bulk" $In_{0.53}Ga_{0.47}As$, 0.5 eV for $In_{0.53}Ga_{0.47}As$/ InP QWs, and 0.3 eV for strained $In_{0.75}Ga_{0.25}As$ QWs with InP barriers [139]. As for the ionized impurity scattering, we have calculated the mobility μ_{AD} limited by the alloy disorder scattering using the potential of Equation (4.3). Figure 4.9 (b) is a plot of μ_{AD} versus charge density, calculated with three values of δV ranging between 0.225 eV (top black curve) and 0.6 eV (bottom blue curve). This range of δV causes a change in one order in mobility across the whole charge density range taken into account.

Contrary to the case of ionized impurity scattering, we had to use very different values of the AD potential to reasonably fit the data in the 2 samples: ~ 0.6 eV for the more strained sample, reducing to 0.225-0.275 eV to the less strained ones. This increase in the alloy potential could

be related to the lattice mismatch in the QWs, a high level of strain can induce clustering inside the QW, creating regions with In fluctuations, which can act as additional scattering centers. [148] These results confirm that alloy potential acts as a limiting factor for the low temperature mobility and can be improved with the decrease in strain in the QW.

The interface roughness scattering is characterized by two parameters: Δ, the amplitude of the roughness in the growth direction, and Λ, its characteristic length in the interface plane and is anisotropic in nature. Mobility versus charge density curves were calculated by numerical integration of Equation (4.1). In sample with a marked mobility anisotropy (~40%), it is reasonable that IR plays a major role since the measured roughness is highly anistropic. On the other hand, in the more symmetric sample, the asymmetric roughness sholud not play a role, so we did not take into account when we modeled the μ vs. n [93].

The IR contribution is thus only used in the sample with t = 50 nm and by applying the formalism developed in references [134,135], the measured roughness is not able to account for the observed mobility in the unstrained samples, since it would yield values orders of magnitude higher than the observed ones, as explained below. As was pointed out in section. 3.4, the sample surface topography should exhibit virtually the same cross-hatch pattern of roughness as the interfaces. AFM measurements of the surface topography show that the root mean square (RMS) amplitude of the roughness is in the 4.4 nm range while the average period of the undulations is ~ 400 nm in the [110] direction and ~ 800 nm in the [-110] direction. This helped us in deciding the fitting parameters. Figure 4.10 (a), we have fixed the RMS roughness Δ at 5 nm and varied the coherence length (Λ) from 50 nm to 1000 nm and in figure 4.10 (b) we have fixed the coherence length (Λ) at 500 nm and varied Δ from 1 to 10 nm. Using the measured roughness parameters in the two directions, the mobility due to IR scattering is in fact at least four orders of magnitude larger than the observed one. Also, as IR is anisotropic the parameters differ in both directions, while fitting we had to use Δ = 5 nm, Λ = 800 nm for [-110] direction and Δ = 4.5 nm, Λ = 600 nm for [110] direction as shown in Figure. 4.11 (c, d). These fitting parameters are significantly more severe than the RMS roughness values we measured on these samples. This suggests though it can reasonably reproduce the measured dependence of the electron mobility on the 2DEG density, but it might not be exhaustive. In fact, the roughness introduced in the semi classical approach of Ref. [134], could be accompanied by spatial modulations of other physical quantities that could limit mobility by themselves. For example, a band gap energy modulation correlated

with the surface roughness has been previously measured in a strained InGaAs sample [149]. Such an effect could be caused by a preferential indium incorporation, during the MBE growth, in the regions where the strain is more relaxed (ridges of roughness profiles); this indium accumulation should both build up the roughness of the growth front and a lead to a small modulation of the indium concentration. A local variation of indium concentration affects the conduction band energy both directly and through the effect of strain [94]. In fact, our GPA analysis data show that the strain is indeed modulated inside the InAs QW, and with fluctuations that increases considerably for non-optimized buffer layers. Such modulations, together with the correlated compositional fluctuations [95] could give rise to nonuniformity in the potential the electrons feel of several tenths of eV and should be taken into account as scattering-limiting mechanisms, adding up to morphological roughness to model the anisotropic component of mobility. scattering-limiting mechanisms, adding up to morphological roughness to model the anisotropic component of mobility.

Also, it was observed that the highly strained samples in combination with local fluctuations in the interface roughness leads to a piezoelectric (PE) field and this PE scattering mechanism resulting from the strain limits the electron mobility at low temperature in the strained quantum wells [150]. These findings imply that the strain can increase the anisotropy of electron mobility in InAs QWs, which can be ascribed to the anisotropy of random PE scattering associated with the strain. This might be one of the sources of the electron mobility anisotropy that has been found often in InAs QWs [151]. We will further investigate all these contributions.

The knowledge of the scattering mechanisms that limit low-temperature mobility in our samples suggests a way to improve the transport properties of the 2DEG. In fact, the effects of AD and IR can be reduced by reducing the strain in the QW through a proper design of the buffer layer. The strain-induced scattering mechanisms influencing the mobility as strain increases could also be qualitatively associated to the roughness induced by piezoelectric scattering at the interface between well and barrier.

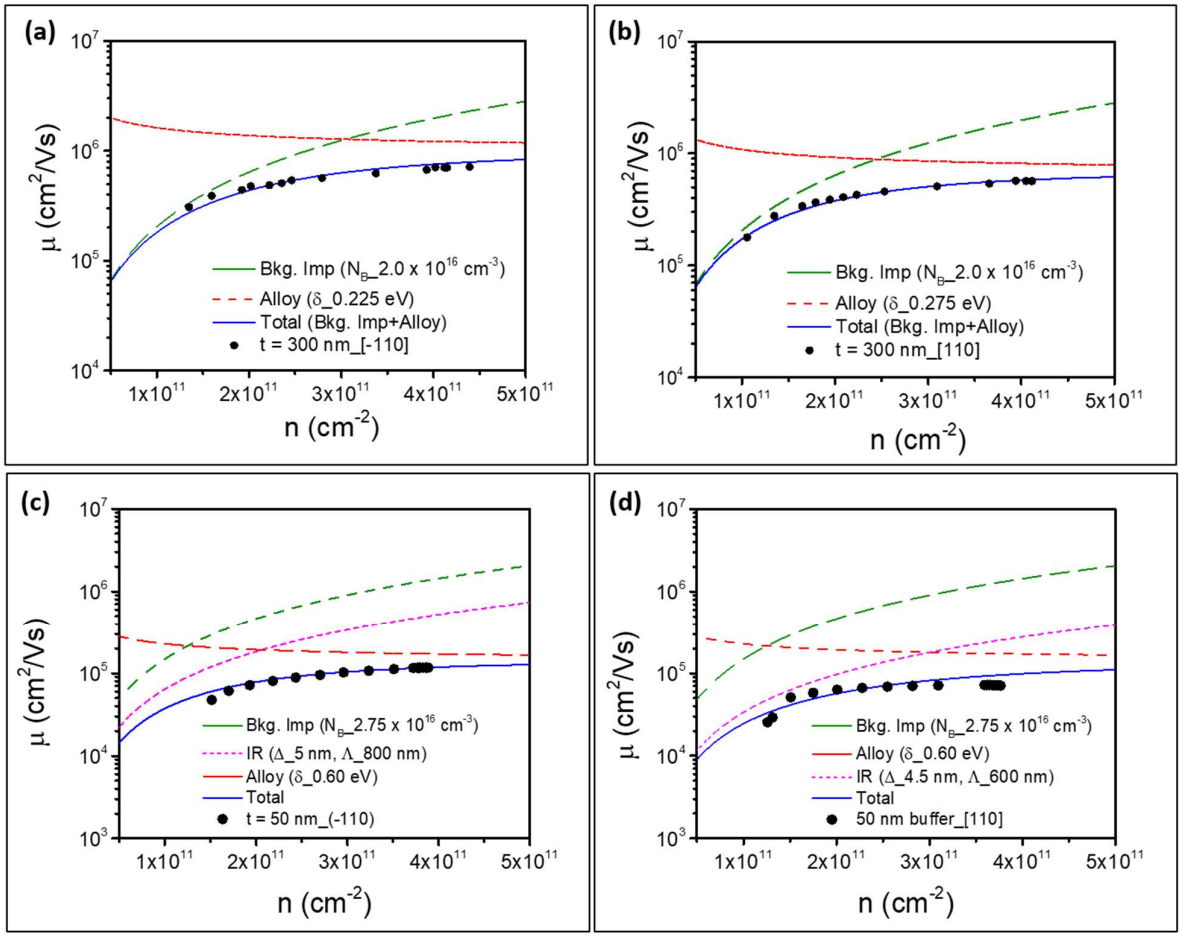

Figure 4.11: Modelling of μ vs n data using the Stern- Howard's model. (a, b) t = 300 nm (c, d) t = 50 nm.

4.6. Closing remarks

Important information has been acquired by this modelling:

- Strain-related effects play a major role in limiting the low temperature mobility. A number of scattering mechanisms are correlated to strain fluctuations. Therefore, our main aim would be to reduce strain the QW region.
- Ionized Impurity takes place mainly because of background impurities and/or chemical point defects, and the slight decrease of N_B we possibly observe with increased t could be due to the improved structural quality of our layers as the residual strain is relieved.

- Alloy disorder scattering is limiting the mobility at high charge densities in both samples, although with much stronger effects for t = 50nm. Further optimization of the buffer layer could therefore have beneficial effects for AD scattering too.
- Interface Roughness is anisotropic and it is only evident in the most strained samples with higher anisotropy.
- Along with these three scattering mechanisms there are some other parameters of scattering involved like band-gap modulation and composition fluctuation and it will be interesting to analyze their contribution in future work.

Chapter 5

Realization of hybrid structures

The superconducting Aluminum thin films are an important element in Andreev systems as discussed in detail in chapter 1. In this work, we focus on the engineering of high-quality superconducting aluminum (Al) films grown in-situ on the semiconductor heterostructures which were discussed in the chapter 3. In the previous chapter we have seen that we could reach a 2DEG mobility in deep InAs quantum wells grown on GaAs substrates around 10^6 cm^2/Vs. Now, in the first part of this work we will we try to reduce the barrier thickness between the quantum well and the superconductor to make the interfaces transparent (To control proximity coupling between the InAs 2DEG and Aluminum). Unfortunately, this makes the InAs 2DEG is sensitive to surface scattering in areas not covered by aluminum. Some experiments have suggested that nanofabrication on these structures can increase surface scattering [152–155], while theory suggests high mobility is needed to support topological phases under realistic device conditions [156]. It is therefore desirable to explore approaches to reach high enough mobility in near surface 2DEGs to have ballistic transport, while maintaining strong spin-orbit coupling and ease of inducement of superconductivity [157]. This surface level pinning of InAs-QW allows for fabrication of transparent contact to superconductors giving high quality devices [158,159]. After the optimization of near surface QW structures Al layer deposition is done in-situ. These hybrid structures are then studied for the structural and transport properties. lastly, the induced superconductivity in the InAs 2DEG will be studied using Josephson junctions. We believe this work could further enhance the progress going on in the direction of the *Andreev* qubits.

5.1 Optimization of InAs QW structures

As described in Chapter 3, Solid source Molecular Beam Epitaxy (MBE) was used to grow InAs/$In_{0.81}Ga_{0.19}As$/$In_{0.81}Al_{0.19}As$ deep Quantum Wells (QW) on a semi-insulating GaAs (001) substrate. The metamorphic QW region was grown over a strain-relieving step-graded $In_xAl_{1-x}As$ buffer terminated with a 300 nm thick $In_{0.84}Al_{0.16}As$ layer to ensure optimal strain relaxation which maximized electron mobility in deep 2DEGs [160]. In this section we have optimized the distance 'd' of the QW from surface for proximity effect and then we have further tuned the charge density in these structures by Si **δ**-doping at a 7 nm spacer in the lower $In_{0.81}Al_{0.19}As$ barrier.

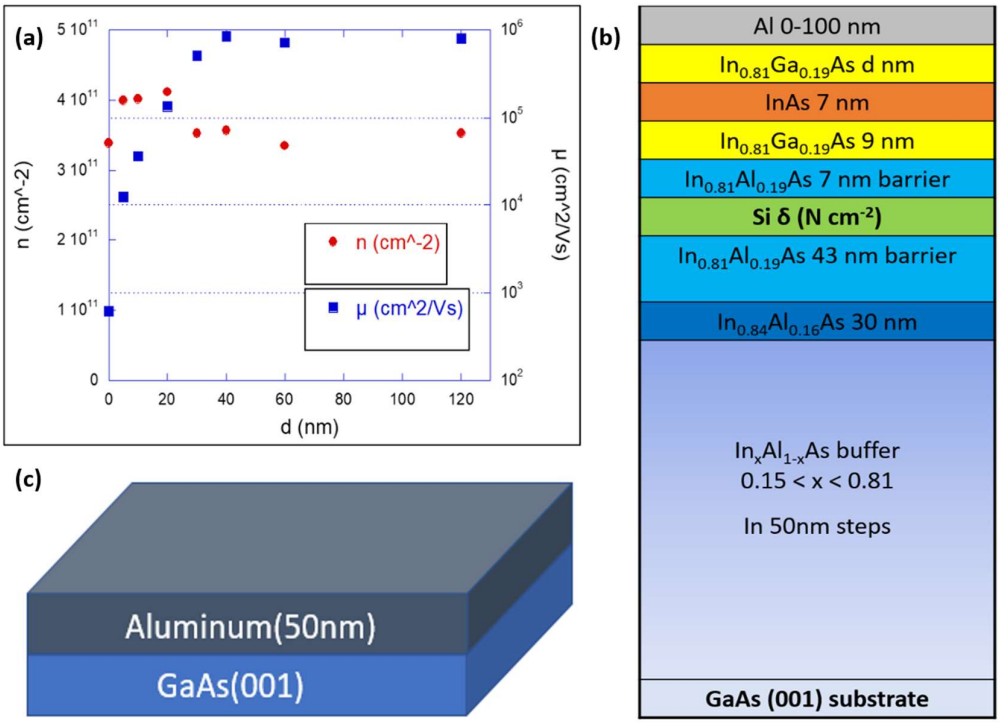

Figure 5.1: (a) low-temperature (T=4.2 K) electron charge density and mobility in the InAs/$In_{0.81}Ga_{0.19}As$ 2DEG as a function of d (distance of QW from surface) (b) the schematic of the growth sequence of Al- InAs/GaAs hybrid system (c) 50 nm thick Al grown on GaAs substrate by MBE (as reference sample).

5.1.1 Optimization of distance of QW from Surface

We have investigated the effect of the thickness *d* of the $In_{0.81}Ga_{0.19}As$ barrier separating a 7nm InAs QW from the surface in undoped 2DEGs. Figure. 5.1 (a) shows the charge density *n* and electron mobility μ at 4K as a function of *d* in the 0-120 nm range. It can be seen that μ is

independent of *d* down to about 30 nm at values around $\mu = 8 \times 10^5$ cm^2/Vs, consistently with what we previously found on similar samples after optimization of the buffer layer [47]. Mobility then decreases sharply to 3.6×10^4 cm^2/Vs at $d = 10$ nm, 1.2×10^4 cm^2/Vs at $d = 5$ nm, and 6.1×10^2 cm^2/Vs at $d = 0$ nm (in the latter two samples part of the contacts were freezing upon cooldown, making them useless for application purposes). Conversely, *n* is largely independent on *d* in the whole range, at values ≈ 3-4 X 10^{11} cm^{-2}. The electron transport properties of the samples of the above structures are evidently influenced by surface scattering due to reducing the InGaAs interface. Therefore, the mobility degradation with respect to the reduction of top barrier thickness could be attributed to the remote Coulomb scattering due to charges fixed at the semiconductor/oxide interface [161].

These findings can also be interpreted with one-dimensional Poisson-Schrödinger (PS) simulations performed as a function of *d* in the same range [162]. In the simulations we set a n-type background doping of $n_B = 4 \times 10^{16}$ cm^{-3} in the $In_{0.81}Ga_{0.19}As$ barriers, while the Fermi level at the surface E_F was pinned 15 meV below the conduction band minimum for all the samples. Conduction and valence band edges, as well as the 3D electron density profiles, are shown in Figure 5.2 (a-c) for three representative values of *d*. The chosen values of n_B and E_F ensured that *n* in the InAs QW remains constant at values ≈ 3.5 - 4 × 10^{11} cm^{-2} independent of *d*, as can be seen in figure 5.2 (d) (red squares). Note that n_B is slightly larger and E_F slightly smaller than what we found in equivalent systems with x = 0.75, where the electron density in the QW decreased at depth lower than 150 nm due to Fermi level pinning at the surface [46]. This is consistent with the fact that InGaAs alloys tend to become more n-type as the In content increases [163]. Profiles of figure 5.2 (a-c) shows that about 69% of the electron wavefunction is confined into the InAs QW. Besides, as the thickness of the top $In_{0.81}Ga0_{.19}As$ barrier decreases, a non-negligible fraction of the electron densities extends up to the top surface (See figure 5.2 (c)). The 3D electron densities at the surface are plotted as a function of '*d'* in figure 5. 2 (d) (blue squares). It can be seen that at $d = 30$nm it goes from zero to about 3 X 10^{12} cm^{-3} and then increases roughly exponentially with decreasing *d*, becoming more than 10^{17} cm^{-3} for InAs QWs placed directly on the surface. This increase correlates directly with the mobility decrease observed for *'d'* < 40nm (Figure 5.2 (d)), and it also confirms the role of surface roughness scattering as the mechanism limiting electron mobility for very shallow InAs 2DEGs [143]. Therefore, we have selected a QW depth of 10 nm as the best compromise between preserving a high enough mobility and the requirements of interface transparency to a

superconductive layer in the surface and the schematic of the hybrid system is shown in figure 5.1(b).

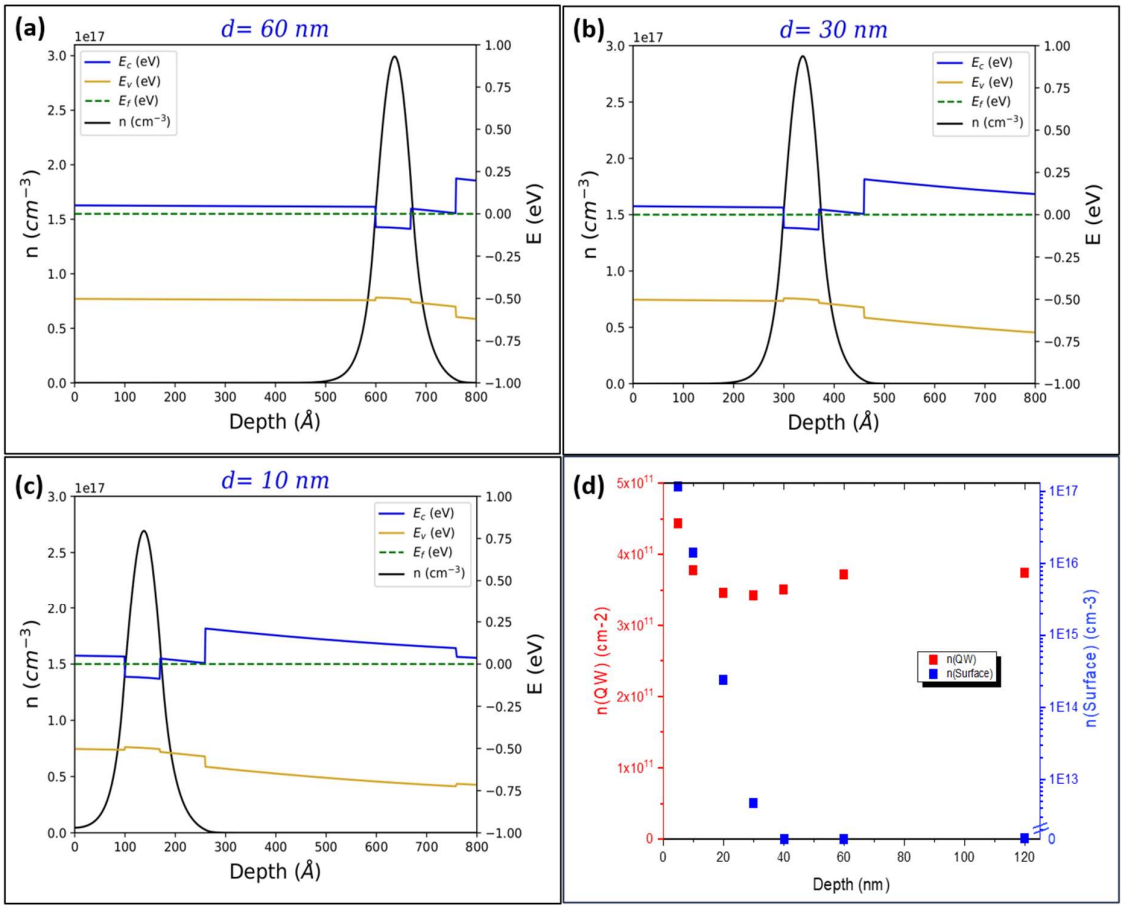

Figure. 5.2: (a, b, and c) Shows the 1D Poisson-Schrödinger simulations of the thickness of top layer of $In_{0.81}Ga_{0.19}As$ (60 nm, 30 nm, and 10 nm). Valence and conduction band profiles are indicated in orange and blue, while 3D electron density is indicated in black (d) Shows the electron charge density in the quantum well as well 3D density at the surface estimated with PS simulations of Fig. 1 (b-d) (background doping in $In_{0.81}Al_{0.19}As$ barriers = 4×10^{16} cm^{-3} surface E_F pinning = 15 meV).

5.1.2 Optimization of Si δ Doping

Remote Si doping is necessary to increase the carrier density in a controlled way, in case higher densities than those forming naturally in this material system are needed. The tuning of electron density in shallow (10 nm) InAs 2DEGs was achieved through a Si δ doping layer in the InAlAs barrier at 7nm from the InGaAs/InAs QW. By changing the Si donor concentration *N,* we were able to tune *n* from 4 X 10^{11} cm^{-2} up to more than 10^{12} cm^{-2}. Corresponding mobility μ increases up to 5.5 X 10^4 cm^2/Vs for n = 4 X 10^{11} cm^{-2} with the doping concentration of 3 X 10^{11} cm^{-2} and then it drops sharply for n higher than about 8 X 10^{11} cm^{-2}. Possible reasons behind this

sharp decrease could be the scattering by 2nd sub-band or the parallel conduction in silicon delta doping. We ruled out the population of the 2nd sub-band as the PS simulation show a single sub-band upto much higher charges. Further analysis was done through Shubnikov-de Haas oscillations (Figure. 5.3 (b)) on a sample with n = 4.95 X 10^{11} cm^{-2} to investigate these hypotheses. In this case, the SdH behaves as expected, showing well-developed quantum Hall plateaus, single occupied sub-band, Zeeman split-features @ ν=3, 5 (goes to zero, high mobility). Only for the sample with the highest doping and the corresponding degraded mobility oscillations do not go to zero, while the charge is half of what we measure with Hall effect suggesting the formation of a parallel channel in the Si δ doping.

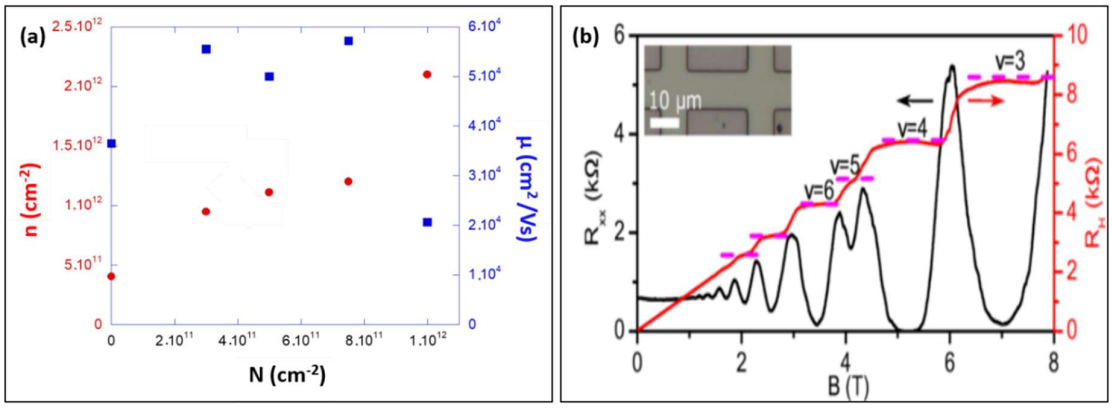

Figure 5.3: (a) Mobility vs carrier density plot with respect to Si **δ**-doping (b) magneto-transport on a non-gated Hall bar, Longitudinal (Rxx, black) and Hall (RH, red) resistance as a function of an out of plane magnetic field B at T=1.5 K.

Also, for a single *N*, we made an attempt to reduce the $In_{0.81}Ga_{0.19}As$ top barrier to 5nm resulted in a decrease of electron mobility from 5.5 X 10^4 cm^2/Vs at n = 9.5 X 10^{11} cm^{-2} to about 2.3 X 10^4 cm^2/Vs at n = 13.5 X 10^{11} cm^{-2}, which could also provide an option in case 2DEGs shallower than 10 nm should be explored for future work.

5.2 Growth of Aluminum thin films

Deposition of Al layers on arsenide compounds is possible inside the MBE growth chamber since Al, together with gallium and indium, is one of the group III elements employed in the MBE of III-V semiconductor compounds. Two level systems (TLSs) are flaws that exist in the substrate, metal, and at their interface, and they are one of the primary drivers of losses in these qubits. As a result, repeatable preparation of atomically clean and contamination-free surfaces

for Al deposition is critical. Therefore in-situ growth of Al layers is a great advantage for such qubits.

After optimizing the shallow InAs QW structures, Al thin films were deposited *in-situ* directly on the InAs 2DEGs inside the MBE system without exposing the sample surface to air. This ensures that the Al is deposited on an oxide-free, as-grown semiconductor surface, while guaranteeing at the same time the best metal material quality. Aluminum was deposited after letting the system pump down the residual arsenic overnight [164]. To prevent aluminum from de-wetting after semiconductor growth, samples were cooled down to about −50°C before deposition by switching off the manipulator heater and idling the effusion cells [165]. The C-type manipulator thermocouple was calibrated for temperatures in the range from -170 to +125 °C following the reference [166]. No active cooling was involved and therefore the cooling power is only related to the MBE system being set to idle state and the sample holder being rotated towards the liquid nitrogen cryopanels. The Al films growth rate was determined starting from the AlAs one using the respective atomic densities, using the relation:

$$R_{Al} = R_{AlAs} * \frac{2n_{AlAs}}{n_{Al}} = R_{AlAs} * 0.357 \quad (5.1)$$

Where, R_{Al} is the growth rate of Al films, R_{AlAs} is the growth rate of AlAs (Calibrated using RHEED)

The deposition rate is around of 0.5 Å/s at a base pressure of a few × 10^{-11} mbar in the growth chamber. We note that the sample surface must remain cold during the deposition. Therefore, the used growth rate (controlled by the cell temperature) needs to be optimized for each specific MBE system geometry, as it determines heat delivered to the surface of the sample during growth. After the Al deposition, the wafer was moved to the load lock chamber (pressure below 5 X 10^{-10} mbar). To prevent thermal condensation or the frost on the Al film, the sample was warmed to ambient temperature in the ultrahigh vacuum, then samples were transferred as fast as possible to the load lock. Different samples were grown with aluminum layer thicknesses ranging from 10 to 50 nm. Al thickness were calibrated within 2% either by a step profilometer after etching the film or with X- Ray reflectivity (XRR). Figure 5.4 shows the XRR curve where the thickness was measured with the help of X-Pert epitaxy software, by measuring the distance between these fringes [167]. The Al layer thickness is calculated as 50±1 nm. The persistence of oscillations is a signature of the flatness of the top surface and of

the bottom Al interface [168] Structural and electrical properties of 50 nm-thick Al/$In_{0.81}Ga_{0.19}As$ InAs/ samples were compared to those of equivalent Al films grown directly on GaAs (001) epitaxial surfaces.

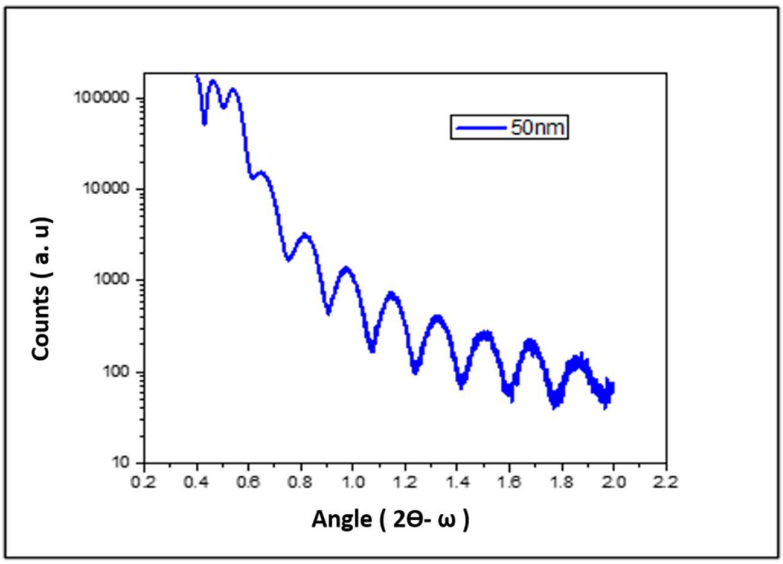

Figure 5.4: Shows the X- Ray reflectivity (XRR) of 50 nm thick Al on the InAs/GaAs heterostructures.

This growth protocol represents the ideal scenario in achieving a flat, abrupt, and impurity-free interface. In this chapter we show that our material system, Al-InAs/GaAs systems satisfies all the requirements necessary to reach the topological superconducting regime.

To assess the importance of growing the aluminum in situ, we grown are three samples on the InAs/GaAs heterostructures using different ex situ procedures:

- S-1) After the growth of InAs/GaAs, As_4 capping is done insitu in the MBE to protect the semiconductor surface from oxidation, followed by air exposure and then re-inserted in the MBE chamber. Then the As_4 is decapped at around 300°C. Afterwards 50 nm of Al is grown in the MBE at -50 °C, with the pressure of 10^{-12} mbar, with the protocol described above.
- S-2) After the growth of InAs/GaAs,As_4 capping is again done insitu, followed by air exposure. Then the sample is inserted in a sputtering chamber followed by As_4 decapping at about 310°C and then 50 nm Al are grown at room temperature with a background pressure around 10^{-7} mbar.

- S-3) After the growth of InAs/GaAs, oxidized in air exposure and then inserted in sputtering chamber. 50 nm of Al is grown at room temperature with pressure around 10^{-7} mbar as in S-2.

5.3 Characterization of Aluminum thin films:

The surface of the Al thin films was characterized by AFM and the structural properties of our Al films were analyzed by X-Ray Diffraction (XRD) and cross-sectional Transmission Electron Microscopy (TEM) followed by the electrical characterization.

5.3.1 AFM

The morphological properties of the surfaces were investigated by AFM. In these images of Al grown on an InAs QW (shown in fig 5.5 (a)), we can see the well-developed extremely uniform cross-hatch pattern [120] in a surface image due to the underlying semiconductor layer as discussed in chapter 3. It is evident that the Aluminum film is conformal to the underlying semiconductor layers. The sample with Al grown directly on GaAs layer shows a particular rectangular rods like pattern that comes from the GaAs template underneath. Here, we can clearly see the coalescence of strongly elongated Al islands. The RMS surface roughness based on these AFM images is 3.0 nm and the sample with Al grown on GaAs layer is around 2.8 nm. Low-temperature growth reduced the aluminum adatom migration and island formation during film deposition and they are consistent with the state of art Al grown on GaAs samples [169,170].

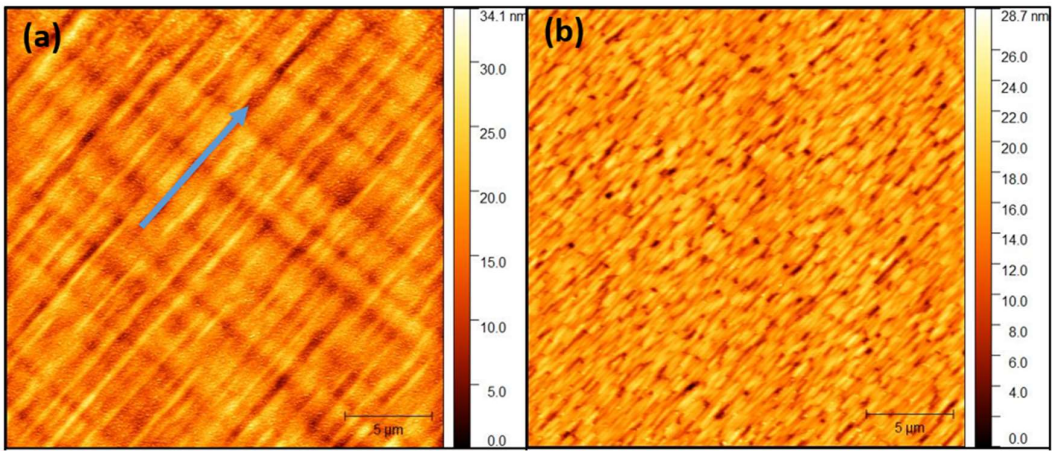

Figure 5.5: AFM scans of 25 X 25 µm of samples (a) 50 nm thick Al on InAs/GaAs heterostructures (The blue arrow indicates the [-110] direction) and (b) 50 nm thick Al on GaAs substrate.

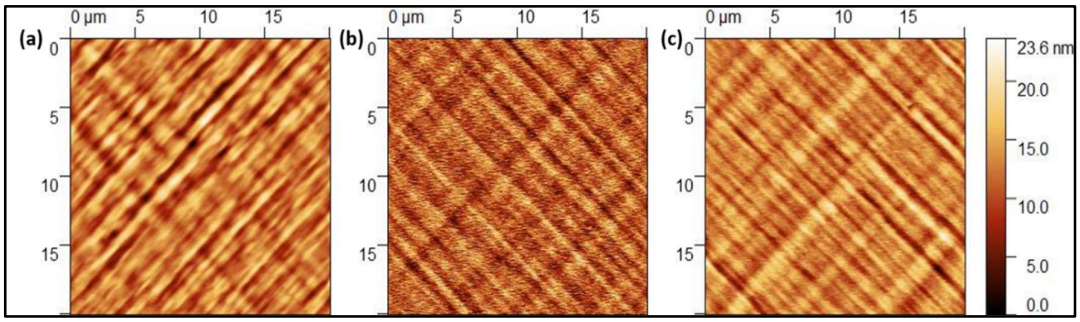

Figure 5.6: Shows the AFM scans of 25X 25 µm of samples (a) S-1, (b) S-2 and (c) S-3. The RMS roughness for these samples are 3.0 nm, 3.6 nm, and 3.3 nm respectively.

In all our samples the RMS roughness varies from one sample to another but were mostly around 3 to 4 nm, the MBE-grown ones always have a smoother surface morphology than those grown using different methods such as E-gun evaporation method. (RMS roughness ~ 7-8 nm) [171]. The other samples grown in this work, S1, S2 and S3 were compared with our 50 nm Al on InAs/GaAs samples. All these samples also shown in figure 5.6 well developed cross hatch pattern and the RMS roughness is also close to the In-situ Al growth at -50°C. Aluminum film is conformal to the underlying semiconductor, independent of deposition technique and surface oxidation.

5.3.2 XRD

XRD analysis of the 50 nm Al film grown in situ on the InAs QW is compared to an equivalent film grown directly on epitaxial GaAs. Figure 5.7 shows symmetric (004) Bragg 2-theta scans for both samples obtained with synchrotron radiation at the MCX beamline. In both cases, the main peak at 2Θ = 66.45°comes from the GaAs substrate [172]. In the case of the Al grown on GaAs, only a single strong Al (111) at 38.14° film is observed. Interference fringes confirm the film quality, along with the thickness of 50 nm. On the other hand, sample grown on InAs, apart for the complex structure on the left of the GaAs (004) peak due to the InAlAs buffer and to the QW region marked as BL, shows two Al-related diffraction peaks: one at 38.14° corresponding to Al (111) and one at 65.2° (Al (022)).

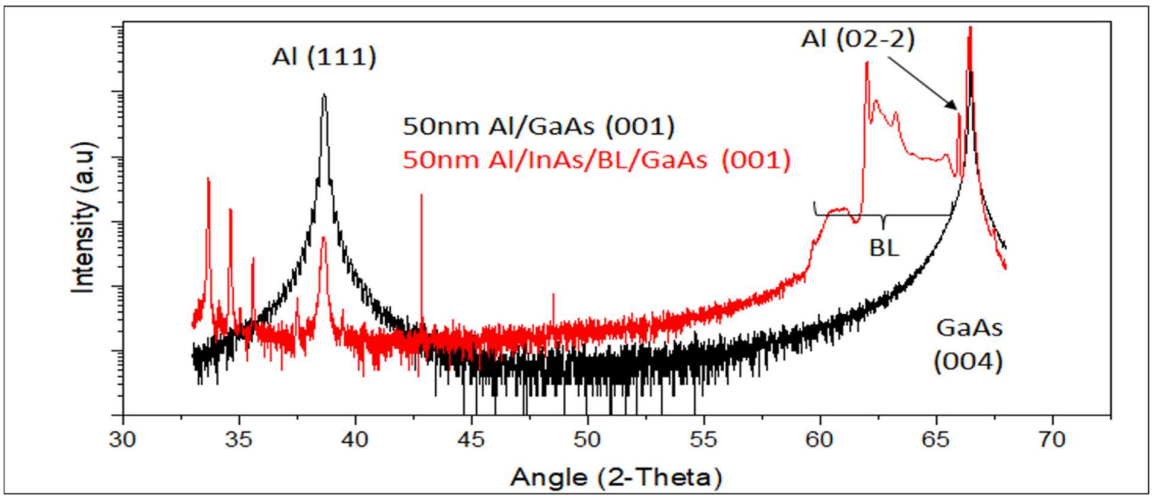

Figure 5.7: θ -2θ XRD scans of the samples - 50 nm thick Al on GaAs (Black) and 50 nm thick Al layer on InAs/GaAs heterostructures (Red).

The intensity of Al (111) is about 100 times less than in the Al/GaAs (001) case, and is likewise 2 orders of magnitudes weaker than the (02-2) peak, despite its reference intensity being 3 times larger. This suggests that the Al film is mainly oriented in the (011) direction, with isolated (111) regions. Around the Al (111) peak we can observe some satellite peaks which may indicate the presence of defects. The lattice parameters inferred from the Al (111) peak are 7.028 Å on InAs and 7.025 Å on GaAs, considered to be the same within the measurement accuracy which are almost equivalent to that of Bulk Al (7.014 Å). Similarly, for (02-2) peak the lattice parameter for the Al/InAs sample is 1.424 Å, very close to the bulk value of 1.431 Å, which indicates that the film is relaxed both on GaAs and in both domains on InAs.

5.3.3 TEM

In order to gain insight into the structural quality and probe the nano-structural assessment of the interfaces, TEM measurements were conducted in cross-sectional geometry. The bright-field TEM images in Fig. 5.8 (a) and (b) depict the growth of the same Al layers on GaAs (001) and on the InAs / GaAs (001) QW, respectively. In both the cases, the Al layer exhibits a uniform thickness of 50 nm, but also reveals the presence of defects within its structure. These defects such as twin planes, stacking faults, and twin boundaries are depicted in Figure 5.7 (c) for Al-GaAs and (d), (e) for Al-InAs/GaAs.

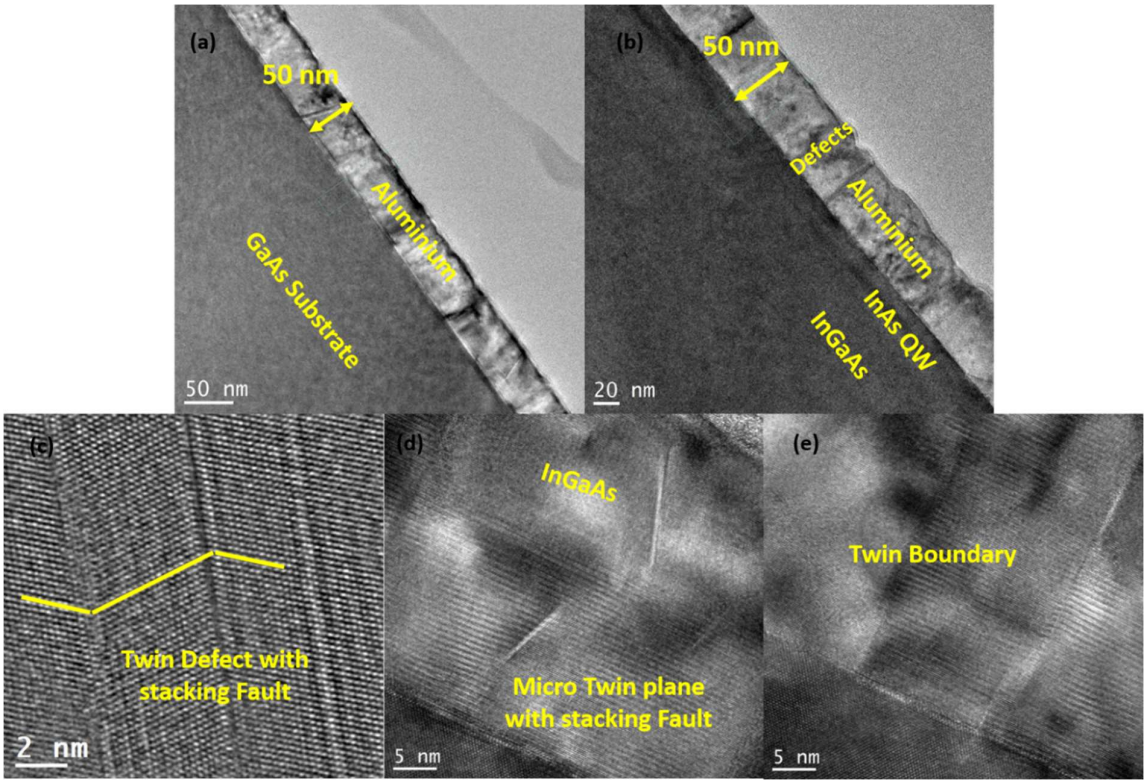

Figure 5.8: Bright Field TEM images of (a) 50 nm thick Al grown on GaAs (001) (b) 50 nm thick Al grown on InAs/InGaAs heterostructure (c) Twin planes with stacking faults in Al layer in Al on GaAs and (d,e) Micro Twin plane with stacking fauls and Twin Boundaries in Al layer on InAs/InGaAs heterostructure.

The HRTEM images of Al layer grown on the GaAs are shown in figure 5.9 (a), and InAs/InGaAs (001) QW are displayed in Figure 5.9 (b, c) and respectively, demonstrating the crystalline nature of the Al layer throughout its thickness. Furthermore, the interface between Al layer and semiconductor buffer layer is found to be abrupt at the ML level. The smoothness of the semiconductor surface in the image indicates that the presence of the boundary is not associated with either a surface step or a crystallographic defect in the semiconductor.

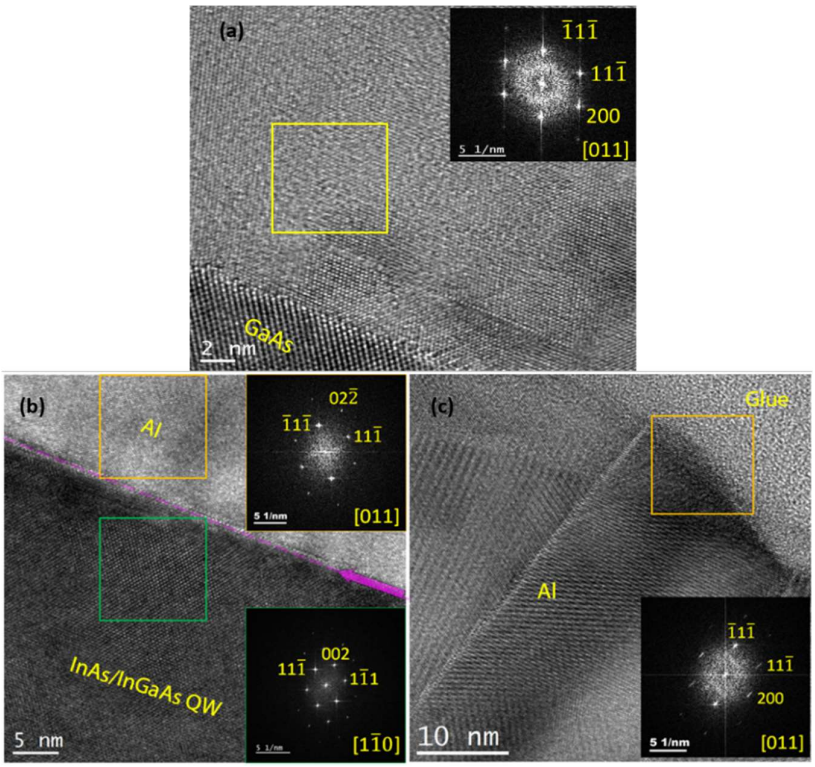

Figure 5.9: HRTEM images of Al layer grown on a) GaAs (001) (b, c), InAs/InGaAs heterostructure, highlighting the high crystalline quality of the heterostructures. Insets within the figures show corresponding FFTs obtained from the regions marked with squares. The zone axis of Al layer is [011]. These FFTs reveal that Al layer on InAs/InGaAs heterostructure exhibits the out of plane directions along both [011] and [111].

To determine the orientation and strain of Al layer, Fast-Fourier transform (FFT) patterns were obtained from the HRTEM image. The insets in figure 5.9 (a-c) display the corresponding FFTs obtained from the regions marked in the respective squares. These FFTs reveal the single crystalline nature of the heterostructure and the zone axis of Al layer is along the [011] direction. The FFT in figure 5.9 (a) illustrate that the out-of-plane orientation of the Al layer on GaAs is uniformly along the [111] direction. In contrast, the Al layer grown on the InAs/InGaAs QW exhibits an out of plane direction primarily oriented along the [011] direction (Figure 5.9 (b)). Upon closer inspection of the Al layer, particularly in isolated regions between twin boundaries, it is observed that the out-of- plane direction of Al layer grown on InAs/InGaAs QW is also oriented along the [111] (Figure 5.9(b)), albeit to lesser extent. Therefore, Al layer grown on InAs/InGaAs QW predominantly exhibits regions with an out-of-plane direction along the [011], with fewer regions aligned along the [111] direction. The

lattice parameters of Al [111] are 7.02 Å and Al [011] is 1.45 Å as calculated with FFT. These observations are consistent with the XRD analysis.

Consistently for both techniques, the Al layer is found to be relaxed to its bulk values in both [111] and [011] directions. Besides, our TEM analysis is consistent with the findings of reference [173], which revealed that the orientation of Al layer switches from [111] to [011] when the in-plane lattice parameter of the underlying semiconductor exceeds 5.98Å. Since in our case the in-plane lattice parameter is exactly the critical value, as inferred from the FFT patterns, a mixture of the two orientations is observed. It is therefore reasonable to think that the lattice constant of the sample with the InAs QW is at or near the boundary between where [111] and [011] normal orientations in Al layers are favored. In general, Al growth depends on various parameters such as strain energy and interfacial energy which depend on lattice parameter. Other process parameters, such as growth rate and growth temperature, could also cause the switch between [111] and [110] oriented aluminum to shift in lattice parameter by altering kinetic processes, but they themselves do not depend on lattice parameter and are not considered further [174]. The presence of defects (such as twin boundaries, dislocations and stacking faults) within the Al layer observed by TEM (see figure 5.8(b)) confirm that the occurrence of satellite peaks around Al [111] peak in XRD analysis should be defect-related. Therefore, it is established that the layer of Al grown consists of crystal grains of two types with the orientations Al [111] and Al [011] parallel to the corresponding GaAs [001] plane with the formation of misfit dislocations. The formation of such dislocations was directly demonstrated by FFT of the high-resolution TEM images [173].

The strain analysis of QW below the defect region and defect free areas was performed using Geometric Phase Analysis (GPA) method to see that if these defects are a cause of an increase in strain in QW region. Results are shown in figure 5.10. Below the defect-free Al region (a) we see that there is 2% perpendicular strain variation between InAs QW (red) and $In_{0.81}Ga_{0.19}As$ (green), consistently with lattice image analysis. In the areas below a defect in Al (b) there is only a minute increase in perpendicular strain by 0.5% between InAs QW and $In_{0.81}Ga_{0.19}As$. This shows that the defects in the Al film are not causing further strain in the QW region and our QW is almost unaffected. In summary, TEM and XRD analysis reveals that the lattice parameters of our Al films are in agreement with the bulk Al, which demonstrates that despite some defects our Al film is relaxed. Also, these defects in the Al layer are not affecting the QW well-region despite being close to surface.

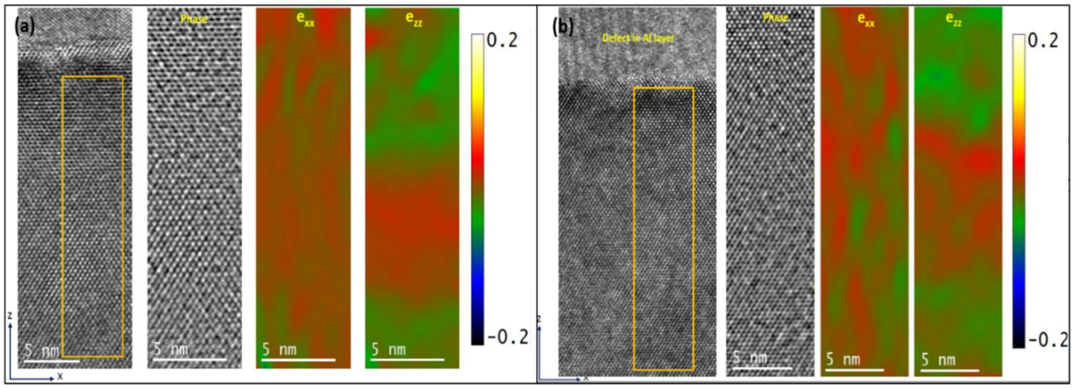

Figure 5.10: Strain analysis of QW in sample with Al layer on InAs/InGaAs heterostructure (a) QW below defect-free Al region: 2% ⊥ strain variation between InAs QW (red) and $In_{0.81}Ga_{0.19}As$ (green), consistent with lattice image analysis (b) Below defect in Al region: 2.5% ⊥ strain variation between InAs QW and $In_{0.81}Ga_{0.19}As$.

5.4 Resistivity measurements

Four-terminal resistivity measurements of Al layers were done on 1x4 mm^2 samples from 4.2K to 300 K with a testing current of $5x10^{-6}$ A. The comparison of the temperature dependence of resistivity as a function of temperature for 50 nm Al layers deposited on the InAs/GaAs and directly on the GaAs is shown in figure 5.11. Values of resistivity for a series of different Al films at 4K and 300 K are shown in table 5.1, together with the respective residue-resistance ratios (RRR), defined as R_{300K}/R_{4K}.

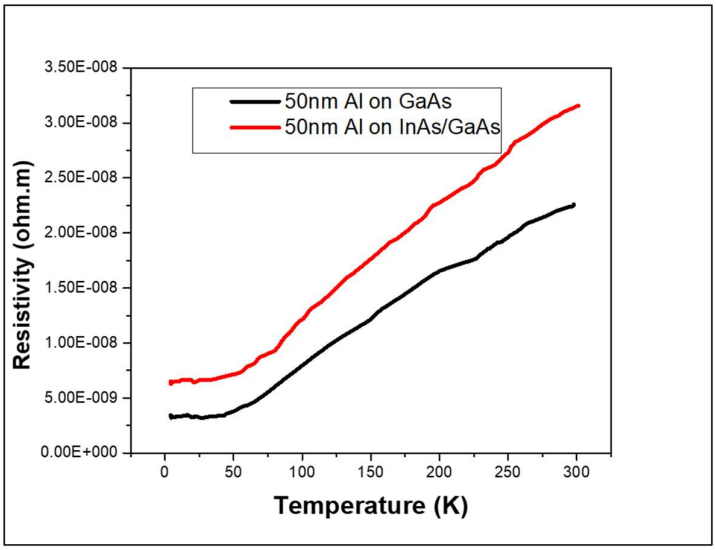

Figure 5.11: Four-point resistivity of 50nm Al layer on GaAs and on the InAs/GaAs heterostructure from 300k to 4K.

As can be seen in in table 5.1 the values of resistivities depend on film thickness. Resistivities of 5.91 x 10^{-9} Ω m (On best sample we have grown of 50 nm Al on InAs ρ_{4k} ~ 2.38 x 10^{-9} Ω m) and 6.95 x 10^{-9} Ω m were achieved at 4K for 50 nm and 10 nm, respectively (actual values should be even higher, especially for 10 nm thick Al, if one considers the 2-3nm oxide layer on the Al surface [175]). Both resistivities and RRR increase with the Al layer thickness as size effects are less evident. Both the low and high temperature values of our 10 nm and 50 nm Al films on InAs, as well as the RRR, are comparable with those of state-of-the-art epitaxial Al layers deposited by us on GaAs (2.05 X 10^{-9}), even though our layers are not single crystal domains. The RRR values are greater than 15 depicting good quality films [171]. Also, we can see here that the temperature dependencies become linear for T > 70 K (fig. 5.11) up to room temperature which is the same behavior of samples with single domains of Aluminum [171].

In table 5.1 we compare also samples (S-1, S-2 and S-3). The sample grown by sputtering has resistivity of these samples is 1-2 orders of magnitude higher than that of samples grown in-situ, and, RRR's are less than 5. These results evidence the superior crystal quality of samples grown by MBE. The electrical quality and morphology of sample S-1(see AFM in Figure 5.6) of this film is comparable to that of direct in-situ growth without air exposures, and it demonstrated the validity of As capping-decapping in case the semiconductor layers need to be transported remotely if, for example, one wants to deposit metals which are not available in the MBE on an oxide-free semiconductor surface.

Table 5.1: Shows the Resistivity values at 4K and 300K for different samples grown during this work and compared with the state of art values [171,176,177].

Al Layer Thickness	ρ_{4K} (Ω.m)	ρ_{300K} (Ω.m)	RRR
Bulk	$9X10^{-10}$	$2.65X10^{-8}$	30
10 nm on InAs/GaAs (MBE)	$6.95X10^{-9}$	$2.22X10^{-8}$	3.19
50 nm on InAs/GaAs (MBE)	$5.91X10^{-9}$	$3.24X10^{-8}$	18.2
50 nm on GaAs (MBE)	$2.56X10^{-9}$	$2.29X10^{-8}$	9
S-1	$1.28X10^{-9}$	$3.11X10^{-8}$	24.26
S-2	$3.76X10^{-8}$	$1.24X10^{-7}$	3.29

S-3	$5.44X10^{-8}$	$1.33X10^{-7}$	2.44
10 nm (MBE, Literature)	$5X10^{-9}$	$2.5X10^{-8}$	5
60 nm (MBE, Literature)	$1.45X10^{-9}$	$2.97X10^{-8}$	20.3

In general, resistivity measurements showed that in-situ growth of Al films yields best results among deposition protocols, resulting into state of art electrical quality despite of the defects present in the Al films. The crystalline orientation and quality of Al layers grown on GaAs is extremely sensitive to the growth conditions, even though the details of the mechanisms involved are still in debate.

5.5 Devices on hybrid structures:

Device fabrication and measurements on the hall bars and Josephson junctions are done at BME, Budapest in collaboration with the "Momentum" Research Group headed by Dr. Szabolcs Csonka.

5.5.1 Hall Bar measurements

Hall bars were made of wafers with the original epitaxial Al layer removed, (process explained in *Appendix 1*) with an aspect ratio of 1:2. In these devices we measured the longitudinal (R_{xx}) and Hall (R_H) resistance as a function of an out of plane magnetic field B. The highest mobility obtained on these structures are $\mu \sim 8.6 \times 10^4$ cm^2/Vs, thus even higher than what we obtained on VdP structures [178]. These results show that after optimizing the 2DEG depth from surface 'd' and the Si doping, we have got semiconducting channels with remarkably high mobility. The best mobility obtained on these hall bar structures on GaAs substrates are better than state of art InP substrates [179].

5.5.2 Josephson junction measurements

The final goal of this work was to prove that the hybrid systems show signs of superconductivity due to the 2DEG being proximitized to the epitaxial Al layer. To achieve this, we fabricated a sample with three Josephson junctions (JJ) (fabrication steps are shown in *Appendix 2).* The schematic of the sample is shown in Figure. 5. 12. We fabricated in total three different JJ's, with a width of 4μm (5 μm before etching) and length depending on the junction, 300 nm for d1, 400 nm for d2 and 500 nm for d3.

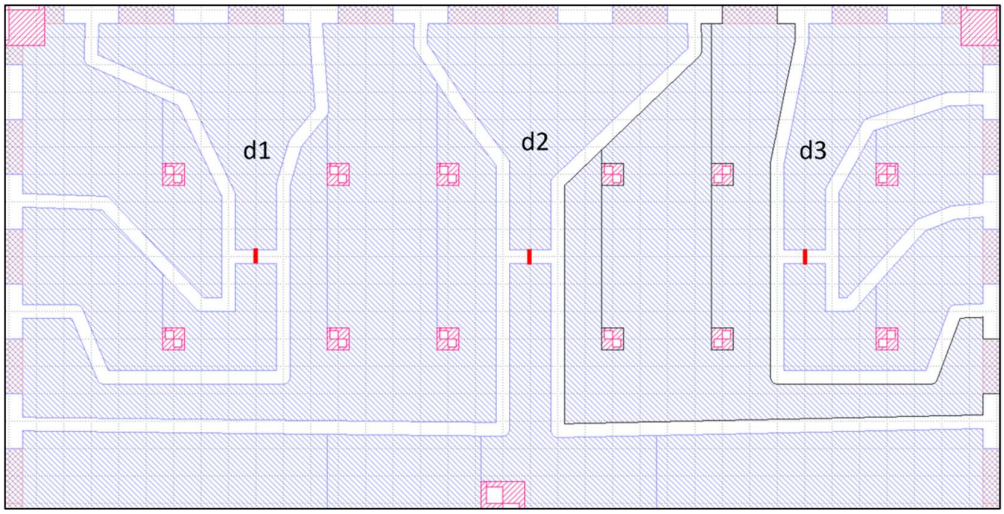

Figure 5.12: Schematic of the JJ's d1, d2 and d3 with the width of 300 nm, 400 nm and 500 nm respectively.

Then all the three junctions with 2-Point contact were measured, to compare the size of the supercurrent in the junctions at least qualitatively. The resulting resistance-current curve are shown in Figure 5.13 (a) for all three junctions. There is a clear trend showing decreasing critical current with increasing junction length, which is appropriate for our expectations, but it must be noted that the current in the three junction is rather different for the same DC voltages, due to the difference in the contact resistances. A better proof for the benefits of the shorter junction is the sharpness of the differential resistance curve on the case of d1 compared to d2 and d3.

As, we were able to see supercurrent in all three junctions, meaning that there is indeed a robust proximity superconductivity appearing inside the InAs layer (Figure 5.13 (a)). To be able to examine it a bit further, we measured d3 (As one of the contacts in d1 became faulty) in a 4 - Point setup for different magnetic fields. For these measurements we used current bias with a 1 MΩ resistance in series, and measured the voltage drop in a lock-in amplifier after magnifying it with a differential amplifier. To have a better control over the magnetic field, we used a Yokogawa instead of the build in current source. By knowing the parameters of the magnet, we can calculate the magnetic field from the current (0.485 kG/A). One of the measurements is shown in figure 5.13 (b). The 2D map shows the differential resistance as a function of the magnetic field (x axis) and bias current (y axis).

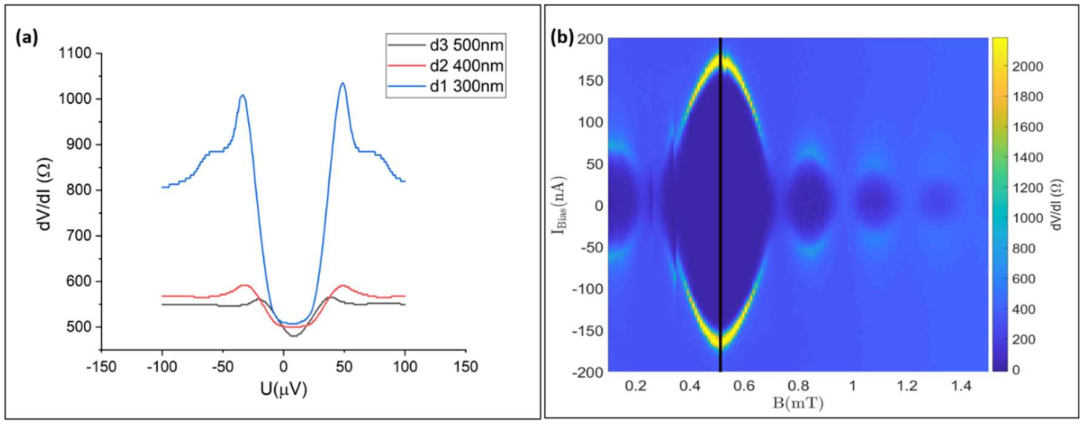

Figure 5.13: (a) Resistance-current curve for the three junctions (b) The 2D map of the differential resistance as a function of the magnetic field (x axis) and bias current (y axis) for d3 below 100 mK temperature.

We see a clearly visible Fraunhofer pattern here. The middle of the central lobe is shifted from 0T, which can be explained with some remanent magnetic field inside the magnet. The size and sign of this shift depends on the previous measurements and magnetic sweep directions. In the inset is a cut taken at the middle of the central lobe, represented by the black line, corresponding to 0T field. The critical current in this case is around 150 nA. We note that the period of the oscillations is shorter than expected, likely due to flux focusing from the Meissner effect in the wide superconducting leads. Thus, with these measurements we have demonstrated the superconducting proximity effect in a Josephson junction [178].

5.6 Conclusion

In this chapter we have shown that our material system, Al-InAs, satisfies all the structural and electrical requirements necessary to reach the topological superconducting regime. This recipe for creating a hybrid system that supports topological superconductivity requires a balance between proximity and segregation of constituent materials. Al layers deposited *in-situ* at -50°C. Structural characterizations with XRD and TEM depicts a double domain structure. Also, AFM revealed that the Aluminum films were conformal to the underlying semiconductor. These Al layers, despite having a double domain crystal structure, exhibit electrical characteristics comparable to the state of the art single-crystal films grown on GaAs.

To understand these structures further, we have fabricated Hall bars and Josephson junctions. These devices will give us better insight in the exploitation of Andreev physics on GaAs-based technology. From these devices we estimated that these semiconductor-superconductor have

high mobility and the interface is relatively transparent. We have studied the Fraunhofer pattern and the results indicate that these InAs 2DEGs are of high quality for the fabrication of Josephson junctions with transparent interfaces. With these results from our hybrid systems, we can take another step towards the progress of Andreev qubits

Conclusions

In this thesis we have followed a route leading to the fabrication of mesoscopic devices on Al/InAs based hybrid systems to make a progress in the direction of exploiting Andreev systems. A great effort has been made in the investigation of the structural and transport properties of InAs quantum wells grown by molecular beam epitaxy on GaAs (001) substrates, in order to realize 2D electron gases with improved electron mobility at low temperature. Due to the large lattice mismatch between the active InGaAs layer and the GaAs substrate, a step-graded buffer layer structure was employed to adapt the two different lattice parameters. In chapter 3 we have tested different buffer layer structures and we have found that the presence of a thick layer (t) of $In_{0.84}Al_{0.16}As$ with suitable indium content on the top of the step-graded buffer can strongly reduce the residual strain in the quantum well region. Corresponding to this strain reduction, we saw an increase of the electron mobility up to $10^6 cm^2/Vs$, which is close to state of art samples on InP substrates. This increase in the mobility is directly related to the decrease of strain in the QW region.

To further understand the limiting factors of mobility, we studied low temperature scattering mechanisms samples with different buffer layer thickness in chapter 4. In this chapter, we tried to understand the different scattering mechanisms in detail. We have shown using power law that impurity scattering in our InAs/GaAs samples are mainly due to background impurities and/ or chemical point defects. We possibly observed a slight decrease in background with increased t, which could be due to the improved structural quality of our layers as the residual strain is relieved. Alloy disorder scattering is limiting the mobility at high charge density for all the samples. Further optimization of the buffer layer could mitigate effects of AD scattering. Furthermore, we saw a higher mobility anisotropy in samples with higher strain, together with an evident effect of interface roughness. Along with these three major scattering mechanisms, other scattering parameters should be taken into account, such as bandgap modulation and composition fluctuation and it would be interesting to analyze their contribution in the future work.

After obtaining high mobility samples, we moved to the next part of our work which is to use these semiconductor heterostructures for integration into hybrid platforms. Our results on Al/InAs 2DEGs grown metamorphically on GaAs substrates show that *in-situ* Al deposition in the MBE chamber can provide state-of-the-art hybrid material platforms for topological superconductor devices in terms of crystal quality, electrical characteristics, and interface transparency. We have studied the dependence of the low-temperature transport characteristics of the InAs 2DEG as a function of the 2DEG depth and found that, despite a substantial increase of surface scattering effects, a proper choice of the top barrier thickness (around 10nm) ensures to maintain a large enough mobility (up to 8.6 $x10^4$ cm^2/Vs on delta-doped structures), while allowing at the same time the electron wave function to reach the surface. These transport properties compare favorably to those of state-of-the-art metamorphic shallow InAs 2DEGs grown on InP [157]. Thus, our shallow InAs QWs satisfy all the requirements necessary to reach the topological superconducting regime by optimizing the mobility and distance of the QW from the surface to have proximity effect.

These Al layers deposited *in-situ* were characterized by XRD and TEM and they showed a double domain crystal structure, but they nevertheless exhibit electrical characteristics comparable to the state of the art single-crystal films grown on GaAs. Also, we have shown superconducting proximity effect using Josephson junctions. Therefore, we can conclude that the observed phenomenology opens the way to the exploitation of Andreev physics on GaAs-based technology.

Appendix 1

This appendix describes the recipes that we used for defining Hall bars with top gates on our deep InAs QW samples at BME, Budapest to study the scattering mechanism.

- Cleaning of the sample surface with hot acetone, then rinsed in isopropanol (IPA), then dried with dry N_2.
- Then, O_2 plasma cleaning of the surface for better adhesion, using Diener plasma system 150W 90s.
- Spin coating of a polymethyl methacrylate (PMMA) layer 600K 4.7% at 4000 rpm to get ~300nm thick resist layer for EBL baking at 170°C for 180s.
- EBL writing in a Raith system, 20 kV EHT, dosage between 240-300 $\mu C/cm^2$. This will be the mask for the mesa etching, so the design includes all the hall bars, contacts and bonding pads alongside with the alignment markers.
- Development in 1:3 of MIBK: IPA solution for 60s, and then rinsed in IPA for 30s.
- Then O_2 plasma cleaning of the surface for better adhesion, using Diener plasma system 150W 90s important, so that the Al sticks better and gives a great hard mask for etching.
- 100 nm of Al deposited using E-gun evaporation at 1Å/s speed.
- Lift-off procedure in hot acetone for a few minutes, sonication if necessary.
- Mesa etching at 30°C using a standard III-V etchant namely H_2O: $C_6H_8O_7$: H_3PO_4: H_2O_2 with a weight ratio of 220: 55: 3: 3. Etching time is 150s, with a depth around 500nm. Cleaning in 30s DI water, then 30s ethanol
- The profile of the etching is gentler in one direction. This direction is perpendicular to the optically visible lines on the surface, so we arranged the top gates, to always climb from the better slope. This eliminates the need for angled metal deposition, and a thinner layer of metal can be used as well.
- Removing the Al from the sample using MF21 photoresist developer. Etching at 30°C, with times depending on visual feedback corresponding to the disappearance of the Al.

It does not, or very slowly etches the semiconductor, no problem there. Clean the sample in a cascade of DI water bath (3x20s).

- Repeating the surface cleaning, same resist deposition, followed by EBL steps, to realize the contacts and then O_2 plasma cleaning afterwards.
- Metal deposition. We tried different metals and setups to ease the bonding and found the 50/50 Ti/Cr the best. Other bonding pads includes 30/120 Ti/Ai, 30/120/50/50 Ti/Au/Ti/Cr, but none was as good as this. Deposition speeds are 3Å/s for Au, 1Å/s for everything Ti and Cr.
- After another plasma cleaning, thermal activated ALD in a PicoSun machine to create the Al_2O_3 layer needed for gating at 225°C, with 500 cycles of deposition (thickness around 50nm).
- Spin coat resist and then EBL as before to get the top gates.
- E-gun evaporation of Ti/Au, with the thickness 10/90 nm on the top gates
- Lift-off just like previous steps.
- Gluing the samples to a chip carrier with silver paint, then wire bonding before cooling it down to 4K and measure using lock-in technique.

Appendix 2

This appendix describes the recipes that we used for defining Josephson Junctions on our hybrid structures at at BME, Budapest to study the superconducting proximity effect.

- Cleaning of the sample surface with hot acetone, then in isopropanol (IPA), then dried with dry N_2.
- Distribution of the AR 300-80 new adhesion promoter, by confining the sample with a few drops of the substance in a small, enclosed space for 2 min.
- Spin coating the wafer with MMA EBL resist at 4000 rpm, 40s, followed by a 90s 185°C baking process. Then repeat the process. Total thickness around 2x150nm
- EBL of the inverse of the structure, presented in the first image, so the Al can be removed from the unwanted places. 20kV EHT, with the dosage of 80 C/cm^2
- Development in MIBK: IPA 1:3 for 60s, rinsed in IPA for 30s
- Al etching using a slight base, MF-321 (originally photoresist developer, discontinued and replaced by MF-21) at 30°C for 40s with a gentle stirring of the fluid.
- Mesa etching using H_2O: $C_6H_8O_7$: H_3PO_4: H_2O_2 with a weight ratio of 220:55:3:3 (standard III-V etching solution). Goal depth is 400-500nm, to prevent leakages after a thermally activated ALD process (not used in this sample)
- EBL to create the lines to be etched back for the JJ. For this step we used the previous resist without removing it after the mesa etching. Followed by the same steps of writing, development and etching as before except for the mesa etching.
- Measurement setup- The sample was measured in a dilution flow refrigerator at 35mK base temperature using standard lock-in technique using an SR830 SDP Lock-In amplifier in both voltage and current bias. To fine tune the magnetic field, we connected a Yokogawa GS200 DC Voltage / Current Source.

References

[1] M. Brooks. The race to find quantum computing's sweet spot, Nature, S1, Vol. 617, (2023).

[2] R. Blatt and C. F. Roos, *Quantum Simulations with Trapped Ions*, Nat Phys **8**, 277 (2012).

[3] D. Leibfried and R. Blatt, Quantum Dynamics of Single Trapped Ions, Rev. Mod. Phys., Vol. **75**, No.1 (2003).

[4] M. Kjaergaard, M. E. Schwartz, J. Braumüller, P. Krantz, J. I.-J. Wang, S. Gustavsson, and W. D. Oliver, *Superconducting Qubits: Current State of Play*, Annual Review, Cond. Mat. Phys.,031119-050605 (2019).

[5] P. Krantz, M. Kjaergaard, F. Yan, T. P. Orlando, S. Gustavsson, and W. D. Oliver, *A Quantum Engineer's Guide to Superconducting Qubits*, *Appl. Phys. Rev.* **6**, 02131 (2019).

[6] X. L. Wang et al., *18-Qubit Entanglement with Six Photons' Three Degrees of Freedom*, Phys Rev Lett **120**, (2018).

[7] B. E. Kane, *A Silicon-Based Nuclear Spin Quantum Computer*, Nature **393**, 133 (1998).

[8] S. Harvey, *Quantum Dots / Spin Qubits*, (2022).

[9] R. P. Feynman, Simulating Physics with Computers, Oxford University Press and the American Institute of Physics, 1982.

[10] D. P. DiVincenzo, *The Physical Implementation of Quantum Computation*, Fortschr. Phys. 48, 9-11, 771-783, (2000).

[11] B. Schumacher, *Quantum coding*, Phys. Rev. A **51**, 2738, (1995).

[12] B. J. Van Wees, H. Van Houten, C. W. J. Beenakker, J. G. Williamson, L. P. Kouwenhoven, D. Van Der Marel, and C. T. Foxon, *Quantized Conductance of Point Contacts in a Two-Dimensional Electron Gas*, Phys. Rev. Lett., Vol. **60**, No. 9, (1988).

[13] L. P. Kouwenhoven, D. G. Austing, and S. Tarucha, *Few-Electron Quantum Dots*, Rep. Prog. Phys. **64**, 701–736, (2001).

[14] L. P. Kouwenhoven T, *Excitation Spectra of Circular, Few-Electron Quantum Dots*. Vol **278**, Issue 5344, Pp. 1788-1792 (1997).

[15] Zhang Xin, et.al, *Qubits Based on Semiconductor Quantum Dots*. Chinese Physics B, **27**(2): 020305, (2018).

[16] V. Srinivasa, K. C. Nowack, M. Shafiei, L. M. K. Vandersypen, and J. M. Taylor, *Simultaneous Spin-Charge Relaxation in Double Quantum Dots*, Phys Rev Lett **110**, (2013).

[17] R. Hanson, L. P. Kouwenhoven, J. R. Petta, S. Tarucha, and L. M. K. Vandersypen, *Spins in Few-Electron Quantum Dots*, Rev Mod Phys **79**, 1217 (2007).

[18] X. Zhang, H. O. Li, K. Wang, G. Cao, M. Xiao, and G. P. Guo, *Qubits Based on Semiconductor Quantum Dots*, Chinese Physics B., 27(2): 020305, (2018).

[19] A. M. Tyryshkin et al., *Electron Spin Coherence Exceeding Seconds in High-Purity Silicon*, Nat Mater **11**, 143 (2012).

[20] D. Kim, D. R. Ward, C. B. Simmons, D. E. Savage, M. G. Lagally, M. Friesen, S. N. Coppersmith, and M. A. Eriksson, *High-Fidelity Resonant Gating of a Silicon-Based Quantum Dot Hybrid Qubit*, Npj Quantum Inf **1**, (2015).

[21] G. Nicolí, M. S. Ferguson, C. Rössler, A. Wolfertz, G. Blatter, T. Ihn, K. Ensslin, C. Reichl, W. Wegscheider, and O. Zilberberg, *Cavity-Mediated Coherent Coupling between Distant Quantum Dots*, Phys. Rev. Lett. **120**, 236801, (2017).

[22] L. E. Bruhat, T. Cubaynes, J. J. Viennot, M. C. Dartiailh, M. M. Desjardins, A. Cottet, and T. Kontos, Strong Coupling between an Electron in a Quantum Dot Circuit and a Photon in a Cavity, n.d.

[23] Y. Nakamura, Yu. A. Pashkin, and J. S. Tsai, *Coherent Control of Macroscopic Quantum States in a Single-Cooper-Pair Box*, Nature **398**, 786 (1999).

[24] R. Barends et al., *Superconducting Quantum Circuits at the Surface Code Threshold for Fault Tolerance*, Nature **508**, 500 (2014).

[25] A. G. Fowler, M. Mariantoni, J. M. Martinis, and A. N. Cleland, *Surface Codes: Towards Practical Large-Scale Quantum Computation*, Phys Rev A **86**, (2012).

[26] V. Bouchiat, D. Vion, P. Joyez, D. Esteve, and M. H. Devoret, *Quantum Coherence with a Single Cooper Pair*, Physica. Scripta. Vol. T**76**, 165-170, (1998)

[27] J. E. Mooij, T. P. Orlando, L. Levitov, L. Tian, C. H. Van Der Wal, and S. Lloyd, *Josephson Persistent-Current Qubit*, Science (1979) **285**, 1036 (1999).

[28] J. M. Martinis, *Superconducting Phase Qubits*, Quantum Inf Process **8**, 81 (2009).

[29] J. Koch, T. M. Yu, J. Gambetta, A. A. Houck, D. I. Schuster, J. Majer, A. Blais, M. H. Devoret, S. M. Girvin, and R. J. Schoelkopf, *Charge-Insensitive Qubit Design Derived from the Cooper Pair Box*, Phys Rev A **76**, (2007).

[30] R. Barends et al., *Coherent Josephson Qubit Suitable for Scalable Quantum Integrated Circuits*, Phys Rev Lett **111**, (2013).

[31] Y. Chen et al., *Qubit Architecture with High Coherence and Fast Tunable Coupling*, Phys Rev Lett **113**, (2014).

[32] V. E. Manucharyan, J. Koch, L. Glazman, and M. Devoret, *Fluxonium: Single Cooper Pair Circuit Free of Charge Offsets*, Science, Vol **326**, Issue 5949, pp. 113-116, (2009).

[33] A. Kitaev, *Protected Qubit Based on a Superconducting Current Mirror*, Patent- US 7,858,966 B2, (2010).

[34] P. Brooks, A. Kitaev, and J. Preskill, *Protected Gates for Superconducting Qubits*, Phys Rev A **87**, (2013).

[35] A. Gyenis, P. S. Mundada, A. Di Paolo, T. M. Hazard, X. You, D. I. Schuster, J. Koch, A. Blais, and A. A. Houck, *Experimental Realization of an Intrinsically Error-Protected Superconducting Qubit*, (2019).

[36] Z. L. Xiang, S. Ashhab, J. Q. You, and F. Nori, *Hybrid Quantum Circuits: Superconducting Circuits Interacting with Other Quantum Systems*, Rev Mod Phys **85**, 623 (2013).

[37] Y. Kubo et al., *Hybrid Quantum Circuit with a Superconducting Qubit Coupled to a Spin Ensemble*, Phys Rev Lett **107**, (2011).

[38] D. Marcos, M. Wubs, J. M. Taylor, R. Aguado, M. D. Lukin, and A. S. Sørensen, *Coupling Nitrogen-Vacancy Centers in Diamond to Superconducting Flux Qubits*, Phys Rev Lett **105**, (2010).

[39] X. Zhu et al., *Coherent Coupling of a Superconducting Flux-Qubit to an Electron Spin Ensemble in Diamond*, (2011).

[40] M. H. Devoret and R. J. Schoelkopf, *Superconducting Circuits for Quantum Information: An Outlook*, Science **339,** (2013).

[41] R. M. Lutchyn, E. P. A. M. Bakkers, L. P. Kouwenhoven, P. Krogstrup, C. M. Marcus, and Y. Oreg, *Realizing Majorana Zero Modes in Superconductor-Semiconductor Heterostructures*, Nature Reviews Materials **3**, pages52–68 (2018).

[42] J. Shabani, A. P. McFadden, B. Shojaei, and C. J. Palmstrøm, *Gating of High-Mobility InAs Metamorphic Heterostructures*, Appl Phys Lett **105**, (2014).

[43] F. Nichele et al., *Scaling of Majorana Zero-Bias Conductance Peaks*, Phys Rev Lett **119**, (2017).

[44] A. T. Hatke, T. Wang, C. Thomas, G. C. Gardner, and M. J. Manfra, *Mobility in Excess of 10^6 Cm^2/V s in InAs Quantum Wells Grown on Lattice Mismatched InP Substrates*, Appl Phys Lett **111**, (2017).

[45] C. Thomas, A. T. Hatke, A. Tuaz, R. Kallaher, T. Wu, T. Wang, R. E. Diaz, G. C. Gardner, M. A. Capano, and M. J. Manfra, *High-Mobility InAs 2DEGs on GaSb Substrates: A Platform for Mesoscopic Quantum Transport*, Phys Rev Mater **2**, (2018).

[46] F. Capotondi, G. Biasiol, D. Ercolani, V. Grillo, E. Carlino, F. Romanato, and L. Sorba, *Strain Induced Effects on the Transport Properties of Metamorphic InAlAs/InGaAs Quantum Wells*, Thin Solid Films **484**, 400 (2005).

[47] A. Benali, P. Rajak, R. Ciancio, J. R. Plaisier, S. Heun, and G. Biasiol, *Metamorphic InAs/InGaAs QWs with Electron Mobilities Exceeding 7×10^5 Cm^2/Vs*, J Cryst Growth **593**, (2022).

[48] Y. Oreg, G. Refael, and F. Von Oppen, *Helical Liquids and Majorana Bound States in Quantum Wires*, Phys Rev Lett **105**, (2010).

[49] S. Das Sarma, M. Freedman, and C. Nayak, *Majorana Zero Modes and Topological Quantum Computation*, Npj Quantum Inf **1**, (2015).

[50] A. Y. Kitaev, *For Shot Noise in Diffusive Conductors* (Universality, Nonlocality, and Exchange Effects), Plenum Press, (2001).

[51] Ö. Gül et al., *Ballistic Majorana Nanowire Devices*, Nature Nanotechnology **13**, pages192–197 (2018).

[52] P. Krogstrup, N. L. B. Ziino, W. Chang, S. M. Albrecht, M. H. Madsen, E. Johnson, J. Nygård, C. M. Marcus, and T. S. Jespersen, Epitaxy of Semiconductor-Superconductor Nanowires, Nature Materials **14**, 400-406, (2015).

[53] N. A. Güsken, T. Rieger, P. Zellekens, B. Bennemann, E. Neumann, M. I. Lepsa, T. Schäpers, and D. Grützmacher, *MBE Growth of Al/InAs and Nb/InAs Superconducting Hybrid Nanowire Structures*, Nanoscale **9**, 16735 (2017).

[54] J. E. Sestoft et al., *Engineering Hybrid Epitaxial InAsSb/Al Nanowire Materials for Stronger Topological Protection*, Phys. Rev. Materials **2**, (2017).

[55] H. Zhang et al., Quantized Majorana Conductance, Nature **556**, pages74–79 (2018).

[56] M. T. Deng, S. Vaitiekenas, E. B. Hansen, J. Danon, M. Leijnse, K. Flensberg, J. Nygård, P. Krogstrup, and C. M. Marcus, *Majorana Bound States in a Coupled Quantum-Dot Hybrid-Nanowire System*, (2016).

[57] A. Y. Cho and H. C. Casey, *GaAs-Alx Ga1-x As Double-Heterostructure Lasers Prepared by Molecular-Beam Epitaxy*, Appl Phys Lett **25**, 288 (1974).

[58] L. L. Chang, L. Esaki, W. E. Howard, and R. Ludeke, *The Growth of a GaAs–GaAlAs Superlattice*, Journal of Vacuum Science and Technology **10**, 11 (1973).

[59] R. Dingle, W. Wiegmann, and C. H. Henry, *Quantum States of Confined Carriers in Very Thin $Al_xGa_{1-x}As$-GaAs-$Al_xGa_{1-x}As$ Heterostructures*, Phys Rev Lett **33**, 827 (1974).

[60] C. T. Foxon and B. A. Joice, *Growth and Characterization of Semiconductors,* IOP Publishing, **35** (1990).

[61] M. A. Herman and H. Sitter, *Molecular Beam Epitaxy,* Springer Verlag, Berlin, (1996).

[62] M. A. Herman, *Molecular Beam Epitaxy — Fundamentals and Current Status,* SSMATERIALS, vol. **7**, (1996).

[63] K. G. Günther, *Naturissenschaften* **45**, 415, (1958).

[64] C. T. Foxon and B. A. Joyce, *Interaction kinetics of As_4 and Ga on (100) GaAs surfaces using Modulated Molecular beam technique*, Surface Science **50,** (1975).

[65] C. T. Foxon and B. A. Joyce, *Interaction kinetics of As_2 and Ga on (100) GaAs surfaces*, Surface Science **64**, (1977).

[66] F. Turco, J. C. Guillaume, and J. Massies, *Thermodynamic analysis of the Molecular Beam Epitaxy of AlInAs alloys*, J. Cryst. Growth **88**, (1988).

[67] M. V. Laue, *Concerning the Detection of X-Ray Interferences*, Nobel Lecture, (1920).

[68] W.L. Bragg, *The Diffraction of X-Rays by Crystals*, Nobel Lecture, (1922).

[69] T. E. Jenkins., *Semiconductor Science.* Prentice Hall International (UK) Limited, 1st Edition (1995).

[70] A. Neels, A. Dommann, P. Niedermann, C. Farub, and H. Von Känel, *Advanced Stress, Strain and Geometrical Analysis in Semiconductor Devices*, in *AIP Conference Proceedings*, Vol. **1300** (2010), pp. 114–119.

[71] M. Barchuk, V. Holý, B. Miljević, B. Krause, T. Baumbach, J. Hertkorn, and F. Scholz, *X-Ray Diffuse Scattering from Threading Dislocations in Epitaxial GaN Layers*, in *Journal of Applied Physics*, Vol. **108** (2010).

[72] M. Laudon, B. F. Romanowicz, *Technical Proceedings of the 2010 NSTI Nanotechnology Conference and Expo: June 21-24,* Anaheim, California, U.S.A., (2010).

[73] J. Hornstra and W. J. Bartels, Determination of the lattice constant of epitaxial layers of III-V compounds, J. Cryst. Growth **44**, 513, (1978).

[74] L. Landau and E. Lifshitz, *Theory of Elasticity,* Pergamon Press, Oxford, (1986).

[75] I. Vurgaftman, J. R. Meyer, and L. R. Ram-Mohan, *Band Parameters for III-V Compound Semiconductors and Their Alloys*, J Appl Phys **89**, 5815 (2001).

[76] B. R. Bennett and J. A. Del Alamo, *Mismatched InGaAs/InP and InAlAs/InP Heterostructures with High Crystalline Quality*, J Appl Phys **73**, 3195 (1993).

[77] A. Lausi, S. Trieste, M. Leoni, S. Aramco, P. Scardi, A. Lausi, E. Busetto, and M. Leoni, *The MCX Project: A Powder Diffraction Beamline at ELETTRA*, (2006).

[78] M. Ganau., *Nanotechnology Applications in Quantitative Neuroscience: Proteomic Analysis of Malignant Gliomas*. Thesis (PhD), University of Trieste, (2013).

[79] A. Saikouski. K. Xu T. Kue D. Bailey T. Millar, *Atomic Force Microscopy AFM. Technical Report,* University of Toronto, Advanced Physics Laboratory, January, (2016).

[80] P. Spellward, *Cross-Sectional Kit Content and Use. Gatan*, (2003).

[81] M. J. H. Hytch, E. Snoeck, and R. Kilaas, *Quantitative Measurement of Displacement and Strain Fields from HREM Micrographs*, Ultramicroscopy **74**, (1998).

[82] C. Koch, *Determination of Core Structure Periodicity and Point Defect Density along Dislocations*, Thesis (Ph.D.), (2002).

[83] R. Dingle, H. L. Störmer, A. C. Gossard, and W. Wiegmann, *Electron Mobilities in Modulation-Doped Semiconductor Heterojunction Superlattices*, Appl Phys Lett **33**, 665 (1978).

[84] I. Vurgaftman, J. R. Meyer, and L. R. Ram-Mohan, *Band Parameters for III-V Compound Semiconductors and Their Alloys*, J Appl Phys **89**, 5815 (2001).

[85] B. E. Keen, D. Landau, H. Cooke, J. G. Park, A. B. Fowler, F. F. Fang, W. E. Howard, and P. J. Stiles, The Institute of Physics and the Physical Society, (1964).

[86] M. Sammon, M. A. Zudov, and B. I. Shklovskii, *Mobility and Quantum Mobility of Modern GaAs/AlGaAs Heterostructures*, Phys Rev Mater **2**, (2018).

[87] S. Vijayakrishnan et al., *Anomalous Electronic Transport in High-Mobility Corbino Rings*, Nat. Comm. **14**, (2023).

[88] M. L. Schattenburg, History of the "Three Beams" Conference, *The Birth of the Information Age and the Era of Lithography Wars,* (2007).

[89] H. C. Pfeiffer, *Variable spot shaping for electron beam lithography*, J Vac Sci Technol **15**, 887 (1978).

[90] J. T. Batley., "*Spin Transport in Lateral Spin Valves*". Thesis (Ph D). University of Leeds, School of Physics and Astronomy, (2015).

[91] T. Mano, A. Ohtake, and T. Kuroda, *Lattice-Mismatched Epitaxy of InAs on (111)A-Oriented Substrate: Metamorphic Layer Growth and Self-Assembly of Quantum Dots*, Phys. stat. sol. (A), 2300767, (2023).

[92] A. Trampert, E. Tournre3, and K. H. Ploog, *Influence of the Growth Mode on the Microstructure,* Phys. stat. sol. (A) **145**, 481 (1994).

[93] F. Capotondi, G. Biasiol, D. Ercolani, and L. Sorba, *Scattering Mechanisms in Undoped In0.75Ga0.25As/ In0.75Al0.25As Two-Dimensional Electron Gases*, in *Journal of Crystal Growth*, Vol. **278**, pp. 538–543, (2005).

[94] D. Ercolani, E. Cancellieri, M. Rosini, G. Biasiol, C. Jacoboni, and L. Sorba, *Transport Anisotropy in High Mobility $In_{0.75}Ga_{0.25}As$ 2DEGs*, in *AIP Conference Proceedings*, Vol. **893**, pp. 463–464, (2007).

[95] D. Ercolani, G. Biasiol, E. Cancellieri, M. Rosini, C. Jacoboni, F. Carillo, S. Heun, L. Sorba, and F. Nolting, *Transport Anisotropy in In0.75 Ga0.25 As Two-Dimensional Electron Gases Induced by Indium Concentration Modulation*, Phys Rev B **77**, (2008).

[96] K. von Klitzing, *The Quantized Hall Effect,* in Nobel Lectures in Physics 1981-1990, World Scientific Publishing Company, Singapore, (1993).

[97] M. Y. Simmons, A. R. Hamilton, S. J. Stevens, D. A. Ritchie, M. Pepper, and A. Kurobe, *Fabrication of High Mobility in Situ Back-Gated (311)A Hole Gas Heterojunctions*, Appl Phys Lett **70**, 2750 (1997).

[98] S. Sze, *Physics of Semiconductor Devices, Wiley* Interscience Publication, New York*,* (1981).

[99] J. M. and L. F. K. Tu, *Electronic Thin Film Science: For Electrical Engineers and Material Scientists,* Macmillan Publishing Company, New York, (1987).

[100] K. L. Schulte, B. T. Zutter, A. W. Wood, S. E. Babcock, and T. F. Kuech, *Design and Characterization of Thick InxGa1-XAs Metamorphic Buffer Layers Grown by Hydride Vapor Phase Epitaxy*, Semicond. Sci Technol **29**, (2014).

[101] M. U. González, Y. González, and L. González, *Study of the Relaxation Process during InGaAs/GaAs (001) Growth from in Situ Real-Time Stress Measurements*, Appl Phys Lett **81**, 4162 (2002).

[102] V. Krishnamoorthy, Y. W. Lin, and R. M. Park, *Application of]] Critical Compositional Difference" Concept to the Growth of Low Dislocation Density ($<10^4/Cm^2$) In $_XGa_{1-X}As$ ($X\leq0.5$) on GaAs*, J Appl Phys **72**, 1752 (1992).

[103] G. B. Galiev, S. S. Pushkarev, I. S. Vasil'evskii, O. M. Zhigalina, E. A. Klimov, V. G. Zhigalina, and R. M. Imamov, *Study of the Influence of Strained Superlattices Introduced into a Metamorphic Buffer on the Electrophysical Properties and the Atomic Structure of InAlAs/InGaAs MHEMT Heterostructures*, Semiconductors **47**, 532 (2013).

[104] S. Löhr, S. Mendach, T. Vonau, C. Heyn, and W. Hansen, *Highly Anisotropic Electron Transport in Shallow InGaAs Heterostructures*, Phys. Rev. B **67**, (2003).

[105] S.I. Gozu, T. Kita, Y. Sato, S. Yamada, and M. Tomizawa, *Characterization of High Indium Content Metamorphic InGaAs/InAlAs Modulation-Doped Heterostructures*, J Cryst Growth **227-228**, (2001).

[106] Y. Sato, T. Kita, S. Gozu, and S. Yamada, *Large Spontaneous Spin Splitting in Gate-Controlled Two-Dimensional Electron Gases at Normal $In_{0.75}Ga_{0.25}As/In_{0.75}Al_{0.25}As$ Heterojunctions*, J Appl Phys **89**, 8017 (2001).

[107] F. Capotondi, G. Biasiol, I. Vobornik, L. Sorba, F. Giazotto, A. Cavallini, and B. Fraboni, *Two-Dimensional Electron Gas Formation in Undoped $In_{0.75}Ga_{0.25}As/In_{0.75}Al_{0.25}As$ Quantum Wells*, Journal of Vacuum Science & Technology B. **22**, 702 (2004).

[108] D. Ercolani, G. Biasiol, E. Cancellieri, M. Rosini, C. Jacoboni, F. Carillo, S. Heun, L. Sorba, and F. Nolting, *Transport Anisotropy in $In_{0.75}Ga_{0.25}As$ Two-Dimensional Electron Gases Induced by Indium Concentration Modulation*, Phys Rev B Cond. Matter Phys **77**, (2008).

[109] J. S. Lee, B. Shojaei, M. Pendharkar, M. Feldman, K. Mukherjee, and C. J. Palmstrøm, *Contribution of Top Barrier Materials to High Mobility in Near-Surface InAs Quantum Wells Grown on GaSb (001)*, Phys Rev Mater **3**, (2019).

[110] I. H. Tan, G. L. Snider, L. D. Chang, and E. L. Hu, *A Self-Consistent Solution of Schrödinger-Poisson Equations Using a Nonuniform Mesh*, J Appl Phys **68**, 4071 (1990).

[111] G. Snider's 1-D Poisson-Schrödinger simulator website., *http://Www.Nd.Edu/snider/*.

[112] P. F. Fewster, *X-Ray Scattering from Semiconductors,* Imperial College Press, London, (2003).

[113] J. Aubin, J. M. Hartmann, A. Gassenq, J. L. Rouviere, E. Robin, V. Delaye, D. Cooper, N. Mollard, V. Reboud, and V. Calvo, *Growth and Structural Properties of Step-Graded, High Sn Content GeSn Layers on Ge*, Semicond Sci Technol **32**, (2017).

[114] T. K. P. R. and J. R. J. E. Ayers, *Heteroepitaxy of Semiconductors – Theory, Growth and Characterization, CRC Press Taylor & Franci Group New York,* (2017).

[115] R. Chierchia, T. Böttcher, H. Heinke, S. Einfeldt, S. Figge, and D. Hommel, *Microstructure of Heteroepitaxial GaN Revealed by X-Ray Diffraction*, J Appl Phys **93**, 8918 (2003).

[116] S. Dolabella, A. Borzì, A. Dommann, and A. Neels, *Lattice Strain and Defects Analysis in Nanostructured Semiconductor Materials and Devices by High-Resolution X-Ray Diffraction: Theoretical and Practical Aspects*, Small Methods **6**, 2100932, (2022).

[117] Ю. Б. Болховитянов and О. П. Пчеляков, *Эпитаксия GaAs На Кремниевых Подложках: Современное Состояние Исследований и Разработок*, Uspekhi Fizicheskih Nauk **178**, 459 (2008).

[118] R. Nandi, S. K. Appani, and S. S. Major, *High Resolution X-Ray Diffraction Studies of Epitaxial ZnO Nanorods Grown by Reactive Sputtering*, J Appl Phys **121**, (2017).

[119] D. M. Paskiewicz, D. E. Savage, M. V. Holt, P. G. Evans, and M. G. Lagally, *Nanomembrane-Based Materials for Group IV Semiconductor Quantum Electronics*, Sci Rep **4**, (2015).

[120] K. H. Chang, R. Gilbala, D. J. Srolovitz, P. K. Bhattacharya, and J. F. Mansfield, *Crosshatched Surface Morphology in Strained III-V Semiconductor Films*, J Appl Phys **67**, 4093 (1990).

[121] A. G. Cullis, A. J. Pidduck, and M. T. Emeny, *Growth Morphology Evolution and Dislocation Introduction in the InGaAsGaAs Heteroepitaxial System*, J Cryst Growth **158**, 15 (1996).

[122] M. Myronov, A. Dobbie, V. A. Shah, X. C. Liu, V. H. Nguyen, and D. R. Leadley, *High Quality Strained Ge Epilayers on a Si0.2 Ge0.8 /Ge/Si (100) Global Strain-Tuning Platform*, Electrochemical and Solid-State Letters **13**, (2010).

[123] O. Yastrubchak, T. Wosiński, J. Z. Domagała, E. Łusakowska, T. Figielski, B. Pécz, and A. L. Tóth, *Misfit Strain Anisotropy in Partially Relaxed Lattice-Mismatched InGaAs/GaAs Heterostructures*, *Phy. Cond. Matter*, **16** (2004).

[124] I. Roh, S. H. Goh, Y. Meng, J. S. Kim, S. Han, Z. Xu, H. E. Lee, Y. Kim, and S. H. Bae, *Applications of Remote Epitaxy and van Der Waals Epitaxy*, Nano Convergence, (2023).

[125] P. R. Berger, P. K. Bhattacharya, and J. Singh, *Comparative Study of the Growth Processes of GaAs, AlGaAs, InGaAs, and InAlAs Lattice Matched and Nonlattice Matched Semiconductors Using High-Energy Electron Diffraction*, J. Appl. Phys **61**, 8 (1987).

[126] A. Fischer-Colbrie, R. D. Jacowitz, and D. G. Ast, Non-Lattice Matched Growth of $In_xGa_{1-x}As$ ($0.53 < x < 0.80$) on InP, J Cryst Growth **127**, 560 (1993).

[127] R. H. Dixon and P. J. Goodhew, *On the Origin of Misfit Dislocations in InGaAs/GaAs Strained Layers*, J Appl Phys **68**, 3163 (1990).

[128] P. Paramasivam, N. Gowthaman, and V. M. Srivastava, *Self-Consistent Analysis for Optimization of AlGaAs/GaAs Based Heterostructure*, J. Electr. Eng. Technol. **7** (2023).

[129] G. C. Gardner, S. Fallahi, J. D. Watson, and M. J. Manfra, *Modified MBE Hardware and Techniques and Role of Gallium Purity for Attainment of Two-Dimensional Electron Gas Mobility $>35\times10^6$ $Cm^2/V\,s$ in AlGaAs/GaAs Quantum Wells Grown by MBE*, J Cryst Growth **441**, 71 (2016).

[130] Y. J. Chung, A. Gupta, K. W. Baldwin, K. W. West, M. Shayegan, and L. N. Pfeiffer, *Understanding Limits to Mobility in Ultrahigh-Mobility GaAs Two-Dimensional Electron Systems: 100 Million Cm^2/Vs and Beyond*, Phys Rev B **106**, (2022).

[131] Y. Du, B. Xu, G. Wang, Y. Miao, B. Li, Z. Kong, Y. Dong, W. Wang, and H. H. Radamson, *Review of Highly Mismatched III-V Heteroepitaxy Growth on (001) Silicon*, Nanomaterials **12**, 741 (2022).

[132] A. Moridi, H. Ruan, L. C. Zhang, and M. Liu, *Residual Stresses in Thin Film Systems: Effects of Lattice Mismatch, Thermal Mismatch and Interface Dislocations*, Int J Solids Struct **50**, 3562 (2013).

[133] T. Ando, A. B. Fowler, and F. Stern, Electronic Properties of Two-Dimensional Systems, Rev. Mod. Phys., **54**, 2, (1982).

[134] A. Gold, *Scattering Time and Single-Particle Relaxation Time in a Disordered Two-Dimensional Electron Gas*, Phys. Rev. B **38,** 15**,** (1988).

[135] A. Gold, *Electronic Transport Properties of a Two-Dimensional Electron Gas in a Silicon Quantum-Well Structure at Low Temperature*, Phys. Rev. B **35,** 2**,** (1987).

[136] A. Gold, *Metal insulator transition due to surface roughness scattering in a Quantum-Well*, Solid State Communications **60**, No. 6, (1986).

[137] W. Walukiewicz, H. E. Ruda, J. I. Agowski, and H. C. Gatos, *Electron mobility in modulation-doped heterostructures*, Phys. Rev. B **30,** 8**,** (1984).

[138] N. W. Ashcroft and N. D. Mermin, *Solid State Physics,* Holt-Saunders International Editions*,* (1976).

[139] P. Ramvall, N. Carlsson, P. Omling, L. Samuelson, W. Seifert, M. Stolze, and Q. Wang, *Ga0.25In0.75As/InP Quantum Wells with Extremely High and Anisotropic Two-Dimensional Electron Gas Mobilities*, Appl Phys Lett **68**, 1111 (1996).

[140] P. Ramvall, N. Carlsson, P. Omling, L. Samuelson, W. Seifert, Q. Wang, K. Ishibashi, and Y. Aoyagi, *Quantum Transport in High Mobility Modulation Doped Ga0.25In0.75As/InP Quantum Wells*, J Appl Phys **84**, 2112 (1998).

[141] J. P. Harrang, R. J. Higgins, R. K. Goodall, P. R. Jay, M. Laviron, and P. Delescluse, *Quantum and Classical Mobility Determination of the Dominant Scattering Mechanism in the Two-Dimensional Electron Gas of an A1GaAs/GaAs Heterojunction*, Phys. Rev. B **32,** 12**,** (1985).

[142] L. Pfeiffer, K. W. West, H. L. Stormer, and K. W. Baldwin, *Electron Mobilities Exceeding 107 Cm2/V s in Modulation-Doped GaAs*, Appl Phys Lett **55**, 1888 (1989).

[143] V. Umansky, R. de-Picciotto, and M. Heiblum, *Extremely High-Mobility Two-Dimensional Electron Gas: Evaluation of Scattering Mechanisms*, Appl Phys Lett **71**, 683 (1997).

[144] S. Nakamura et al., *InGaN- based Multi Quantum Well structure Laser Diode*, Jpn.J. Appl. Phys. **35,** 74**,** (1996).

[145] D. Reuter, M. Versen, M. D. Schneider, and A. D. Wieck, *Increased Mobility Anisotropy in Selectively Doped AlxGa1-XAs/GaAs Heterostructures with High Electron Densities*, J Appl Phys **88**, 321 (2000).

[146] W. Pan, N. Masuhara, N. S. Sullivan, K. W. Baldwin, K. W. West, L. N. Pfeiffer, and D. C. Tsui, *Impact of Disorder on the 5/2 Fractional Quantum Hall State*, Phys Rev Lett **106**, (2011).

[147] M. A. Littlejohn, J. R. Hauser, T. H. Glisson, D. K. Ferry, and J. W. Harrison, *Alloy Scattering and High Field Transport in Ternary and Quaternary III–V Semiconductors*, Solid State Electron **21**, 107 (1978).

[148] S. K. Lyo and I. J. Fritz, *Alloy-Scattering and Strain-Fluctuation-Scattering Contributions to the Low-Temperature Electron Mobility in Ternary Quantum Wells and Heterostructures*, Phys. Rev. B **46,** 12**,** (1992).

[149] N. Yamamoto, T. Mita, S. Heun, A. Franciosi, and J. M. Bonard, *Cathodoluminescence from $In_xGa_{1-x}As$ layers grown on GaAs Using a Transmission Electron Microsc*ope, Mat. Res. Soc. Symp. Proc. Vol. 588, (2000)

[150] Q. Wei, H. Wang, X. Zhao, and J. Zhao, *Electron Mobility Anisotropy in (Al, Ga) Sb/InAs Two-Dimensional Electron Gases Epitaxied on GaAs (001) Substrates*, Journal of Semiconductors **43**, (2022).

[151] M. Akabori, T. Quang Trinh, M. Kudo, H. Hardtdegen, T. Schäpers, and T. kazu Suzuki, *Strain-Enhanced Electron Mobility Anisotropy in InxGa1−xAs/InP Two-Dimensional Electron Gases*, Physica E **42**, 1130 (2010).

[152] A. T. Hatke, T. Wang, C. Thomas, G. C. Gardner, and M. J. Manfra, *Mobility in Excess of 10^6 Cm^2/V s in InAs Quantum Wells Grown on Lattice Mismatched InP Substrates*, Appl Phys Lett **111**, (2017).

[153] I. 0 Kulik, *Macroscopic quantization and the proximity effect in S-N-S junctions*, Soviet Physics Jept **30**, 5 (1970).

[154] H. Pan and S. Das Sarma, *Physical Mechanisms for Zero-Bias Conductance Peaks in Majorana Nanowires*, Phys Rev Res **2**, (2020).

[155] A. Banerjee et al., *Signatures of a Topological Phase Transition in a Planar Josephson Junction*, Phys. Rev. B **107**, 245304, (2022).

[156] H. Tian and C. Ren, *Distinguishing Majorana and Quasi-Majorana Bound States in a Hybrid Superconductor-Semiconductor Nanowire with Inhomogeneous Potential Barriers*, Results Phys **26**, (2021).

[157] T. Zhang, T. Lindemann, G. C. Gardner, S. Gronin, T. Wu, and M. J. Manfra, *Mobility Exceeding 100,000 cm^2/Vs in Modulation-Doped Shallow InAs Quantum Wells Coupled to Epitaxial Aluminum*, Phys. Rev. Materials **7**, 056201 (2023).

[158] J. Shabani et al., *Two-Dimensional Epitaxial Superconductor-Semiconductor Heterostructures: A Platform for Topological Superconducting Networks*, Phys Rev B **93**, (2016).

[159] T. D. Clark, R. J. Prance, and A. D. C. Grassie, *Feasibility of Hybrid Josephson Field Effect Transistors*, J Appl Phys **51**, 2736 (1980).

[160] A. Benali, P. Rajak, R. Ciancio, J. R. Plaisier, S. Heun, and G. Biasiol, *Metamorphic InAs/InGaAs QWs with Electron Mobilities Exceeding 7×10^5 Cm^2/Vs*, J Cryst Growth **593**, (2022).

[161] P. Nagaiah, V. Tokranov, M. Yakimov, S. Koveshnikov, S. Oktyabrsky, D. Veksler, W. Tsai, and G. Bersuker, *Mobility and Remote Scattering in Buried InGaAs Quantum Well Channels with High-k Gate Oxide*, Journal of Vacuum Science & Technology B, **28**, C3H5 (2010).

[162] I. H. Tan, G. L. Snider, L. D. Chang, and E. L. Hu, *A Self-Consistent Solution of Schrödinger-Poisson Equations Using a Nonuniform Mesh*, J Appl Phys **68**, 4071 (1990).

[163] S. T. Lee et al., *High Performance InGaAs Channel MOSFETs on Highly Resistive InAlAs Buffer Layers*, Solid State Electron **176**, (2021).

[164] G. C. Gardner, S. Fallahi, J. D. Watson, and M. J. Manfra, *Modified MBE Hardware and Techniques and Role of Gallium Purity for Attainment of Two-Dimensional Electron Gas Mobility >35×10^6 cm^2/Vs in AlGaAs/GaAs Quantum Wells Grown by MBE*, J Cryst Growth **441**, 71 (2016).

[165] J. Shabani et al., *Two-Dimensional Epitaxial Superconductor-Semiconductor Heterostructures: A Platform for Topological Superconducting Networks*, Phys Rev B **93**, (2016).

[166] D. P. Pappas and C. S. Arnold, *Application of W–Re Thermocouples for in Situ Ultrahigh Vacuum Use over a Wide Temperature Range* , Review of Scientific Instruments **76**, 016104 (2005).

[167] *Technical Article, X-Ray Thin-Film Measurement Techniques- X-Ray Reflectivity Measurement, The Rigaku Journal, 26(2), (2010).*

[168] J. Tiilikainen, J. M. Tilli, V. Bosund, M. Mattila, T. Hakkarainen, J. Sormunen, and H. Lipsanen, *Accuracy in X-Ray Reflectivity Analysis*, J Phys D Appl Phys **40**, 7497 (2007).

[169] H. W. Liu, F. C. Lin, S. W. Lin, J. Y. Wu, B. T. Chou, K. J. Lai, S. Di Lin, and J. S. Huang, *Single-Crystalline Aluminum Nanostructures on a Semiconducting GaAs Substrate for Ultraviolet to Near-Infrared Plasmonics*, ACS Nano **9**, 3875 (2015).

[170] Y. H. Tsai, Y. H. Wu, Y. Y. Ting, C. C. Wu, J. S. Wu, and S. Di Lin, *Nano- to Atomic-Scale Epitaxial Aluminum Films on Si Substrate Grown by Molecular Beam Epitaxy*, AIP Adv **9**, (2019).

[171] S. W. Lin, J. Y. Wu, S. Di Lin, M. C. Lo, M. H. Lin, and C. Te Liang, *Characterization of Single-Crystalline Aluminum Thin Film on (100) GaAs Substrate*, Jpn J Appl Phys **52**, (2013).

[172] J. Tournet, Growth and Characterization of Epitaxial Al Layers on GaAs and Si Substrates for Superconducting CPW Resonators in Scalable Quantum Computing Systems, Thesis (PhD), University of Waterloo, (2015).

[173] M. V. Lovygin, N. I. Borgardt, I. P. Kazakov, and M. Seibt, *Electron Microscopy of an Aluminum Layer Grown on the Vicinal Surface of a Gallium Arsenide Substrate*, Semiconductors **49**, 337 (2015).

[174] T. Wang, C. Thomas, R. E. Diaz, S. Gronin, D. Passarello, G. C. Gardner, M. A. Capano, and M. J. Manfra, *The Dependence of Aluminum Lattice Orientation on Semiconductor Lattice Parameter in Planar InAs/Al Hybrid Heterostructures*, J Cryst Growth **535**, (2020).

[175] B. T. Chou, Y. H. Chou, Y. M. Wu, Y. C. Chung, W. J. Hsueh, S. W. Lin, T. C. Lu, T. R. Lin, and S. Di Lin, *Single-Crystalline Aluminum Film for Ultraviolet Plasmonic Nanolasers*, Sci Rep **6**, (2016).

[176] J. W. J. R A Serway, *Principles of Physics.* Fort Worth, TX: Saunders College Pub.*, (1998*).

[177] Y. T. Fan, M. C. Lo, C. C. Wu, P. Y. Chen, J. S. Wu, C. Te Liang, and S. Di Lin, *Atomic-Scale Epitaxial Aluminum Film on GaAs Substrate*, AIP Adv **7**, (2017).

[178] M. Süto, T. Prok, P. Makk, M. Kirti, G. Biasiol, E. Tóvári, and S. Csonka, *Near-Surface InAs 2DEG on a GaAs Substrate: Characterization and Superconducting Proximity Effect*, Phys. Rev. B **106**, 235404, (2022).

[179] K. S. Wickramasinghe, W. Mayer, J. Yuan, T. Nguyen, L. Jiao, V. Manucharyan, and J. Shabani, *Transport Properties of near Surface InAs Two-Dimensional Heterostructures*, Appl Phys Lett **113**, (2018).